The inaudible symphony: on the detection and source identification of atmospheric infrasound

The inaudible symphony: on the detection and source identification of atmospheric infrasound

PROEFSCHRIFT

ter verkrijging van de graad van doctor

aan de Technische Universiteit Delft,

op gezag van de Rector Magnificus prof. dr. ir. J.T. Fokkema,

voorzitter van het College voor Promoties,

in het openbaar te verdedigen

op dinsdag 4 november 2008 om 12:30 uur

door

Läslo Gerardus EVERS

doctorandus in de geofysica

geboren te Purmerend

Dit proefschrift is goedgekeurd door de promotoren:
Prof. dr. D.G. Simons
Prof. dr. ir. A. Gisolf

Samenstelling promotiecommissie:

Rector Magnificus,	voorzitter
Prof. dr. D.G. Simons,	Technische Universiteit Delft, promotor
Prof. dr. ir. A. Gisolf,	Technische Universiteit Delft, promotor
Prof. dr. S. Dosso,	University of Victoria
Prof. dr. ir. M.J.L. van Tooren,	Technische Universiteit Delft
Prof. dr. ir. C.P.A. Wapenaar,	Technische Universiteit Delft
Dr. H.W. Haak,	Koninklijk Nederlands Meteorologisch Instituut
Dr. R.W. Whitaker,	Los Alamos National Laboratory

In memory of my father

Contents

1

Introduction

1.1 General introduction to infrasound

■ 1.1.1 What is infrasound?

In general, sound waves are longitudinal waves of which the particle or oscillator motion is in the same direction as the wave propagation. A sound wave traveling through a gas disturbs the equilibrium state of the gas by compressions and rarefactions. Sound waves are elastic waves, thus, when particles are displaced, a force proportional to the displacement acts on the particles to restore them to their original position, see e.g. *Pain* [1983].

A large range of frequencies of these deformations can be facilitated by the gas. Sound waves in the atmosphere become audible to humans if the frequency is in the range of 20 to 20.000 Hz. Ultrasonic sound is inaudible to humans and has frequencies higher than 20.000 Hz. For example, bats use this high frequency sound as sonar for orientation purposes. At the other end of the spectrum, sound also becomes inaudible, when the frequency is lower than 20 Hz. Sound waves are then called infrasound, equivalent to low frequency light which is called infrared and invisible. The lower limit of infrasound is bounded by the thickness of the atmospheric layer through which it travels. When the wavelengths of infrasound become too long, gravity starts acting on the mass displacement. Acoustic-gravity and gravity waves are the results if gravity becomes part of the restoring force [*Gossard and Hooke*, 1975]. From 0.01 Hz and downwards, this gravity effect becomes important and around 0.002 Hz gravity waves have taken over from acoustic waves. In addition to frequency, sound waves have other characteristics like, propagation velocity and amplitude.

Infrasound travels with the speed of sound, 343 m/s at 20 °C in air near the earth's surface. This velocity will increase at higher temperatures and in a down wind situation and vice verse. Furthermore, this velocity depends on the type of gas, i.e. the fundamental property of the material, which also holds for solids and fluids. Low-frequency waves in the atmosphere with a velocity lower than the sound speed also occur, but the restoring force is gravity. Gravity waves typically travel with wind speed like velocities in the order of 1 to 10 m/s.

The pressure fluctuations of sound waves are, in general, small with respect to the ambient pressure. For example, an average sound volume setting of a television set in a living room, will result in pressure fluctuations of 0.02 Pa (60 dB relative to 20 μPa) against a standard background pressure of 1013 hPa. Infrasound roughly deals with receiving amplitudes of hundredths to tens of pascals. If the amplitude becomes too large, the linearity of the longitudinal acoustic wave is lost and shock waves occur. Shock waves are non-linear waves that propagate at velocities higher than the sound speed. As the energy of the shock wave dissipates, a linear acoustic wave will remain if sufficient energy is available.

Due to its low frequency content, infrasound can travel over enormous distance as it experiences little attenuation.

In this thesis, infrasonic waves in the atmosphere are considered in the frequency range of 0.002 to 20 Hz, which travel with the speed of sound and have amplitudes in the order of 10^{-2} Pa to 10^2 Pa at the receiver, after having traveled for hundreds to thousands of kilometers.

■ 1.1.2 What are sources of infrasound?

In general, infrasound is generated when a large volume of air is displaced. Sources of infrasound are, consequently, large and powerful. Examples of such sources are:

- Airplanes:
    - Sub-sonic: regular air traffic generates infrasound. On a quiet night when the measurement conditions are ideal, air planes can be tracked when flying over or nearby an infrasound array at altitudes up to 10 km to distances over 30 km [*Evers*, 2005].
    - Super-sonic: a shock wave is created when a plane travels close to the speed of sound. At short distances, this so-called sonic boom can be heard as two loud bangs being the front and back of the plane flying through the sound barrier. At larger distances, the high frequency audible part is attenuated and infrasound travels further over hundreds of kilometers. Infrasound from the Concorde has been used in an early stage to probe the upper atmosphere [*Balachandran et al.*, 1977; *Liszka*, 1978].

- Aurora: the movement of large volumes of air in the upper atmosphere by aurora, leads to a notable infrasonic signal at the earth's surface. These signals

were first discovered in Alaska by *Wilson* [1967] and come in various types depending on the type of aurora, e.g. as shock waves or pulsating infrasound.

- Avalanches: when large volumes of snow and ice are displaced, infrasound is generated. Measurement systems in the Swiss Alps have been set up to monitor avalanches [*Van Lancker*, 2001].

- Chemical explosions: large explosions like, for example, accidental chemical explosions generate infrasound. Infrasound from military test and natural sources was already used by *Gutenberg* [1939] to visualize the stratosphere through a refractive sequence of zones of silence and strong infrasonic signals observed at the earth's surface.

- Earthquakes: infrasound from earthquakes can be recorded in two ways. Firstly, upward traveling infrasound causes ionospheric disturbances [*Blanc*, 1985] that can be measured by GPS systems [*Calais and Minster*, 1995]. Secondly, infrasound can travel directly from the source region to the observer [*Benioff and Gutenberg*, 1939]. In both cases, displacements of the earth's surface over large regions cause this infrasound.

- Gas flares: infrasound has been observed by *Liszka* [1974] from gas exhausts near oil fields on the North Sea. More recently, infrasound has been associated to the burning of gas near oil and gas fields in Kazakhstan [*Smirnov*, 2006].

- Lightning: cloud-to-cloud and cloud-to-ground discharges cause infrasound because a shock wave is generated by the thermal expansion of the lightning channel [*Few*, 1969]. Huge mass displacements take place within the clouds when charges are reorganized which also lead to infrasound [*Dessler*, 1973]. Cloud-to-ground discharges in the Netherlands have been detected over ranges of 50 km and can be explained by a line-source model [*Assink et al.*, 2008]. A more exotic type of infrasound is generated by transient luminous events such as sprites [*Liszka*, 2004; *Farges et al.*, 2005]. These are discharges from the top of the clouds upwards to the ionosphere.

- Meteors: infrasound is generated when a meteoroid enters the atmosphere at hyper-sonic speeds. Infrasound can also be caused by fragmentation of the meteoroid. Most meteoroids end their journey with a thermal explosion at 30 to 50 km altitude, generating additional infrasound [*ReVelle*, 1976]. Infrasound from the Siberian Tunguska meteor was recorded in 1908, June 30 on the first microbarometers [*Shaw and Dines*, 1904] in the UK and analyzed by *Whipple* [1930].

- Nuclear tests: atmospheric nuclear tests generate infrasound that can travel around the globe several times if the yield is large enough. This was the case with the megaton TNT tests on Novaya Zemlya in the 1960s. Also smaller test can be detected over large ranges [*Posey and Pierce*, 1971].
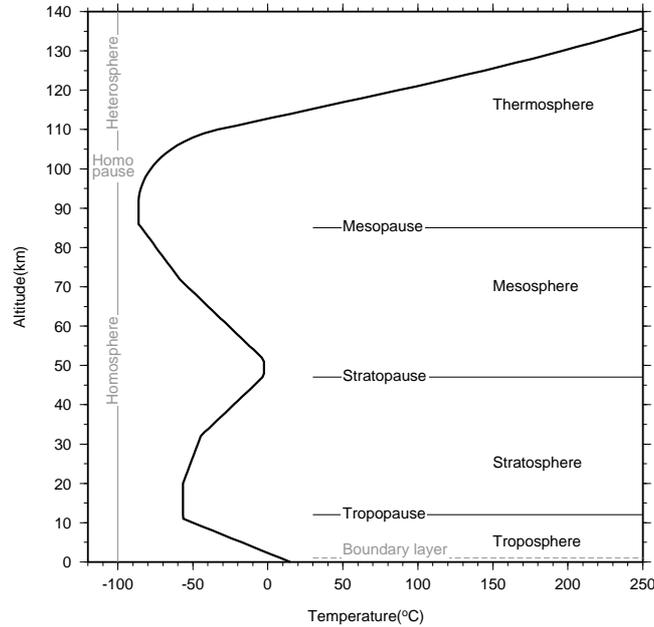
Figure 1.1: *The temperature in the atmosphere as function of altitude based on the average kinetic energy of the atoms, from the U.S. Standard Atmosphere [NOAA et al., 1976].*

- Oceanic waves: the non-linear interaction of oceanic waves traveling in almost opposite directions generates microbaroms in the atmosphere and microseism in the solid earth. These waves coincide with large low pressure systems over the oceans, where strong winds act on the ocean surface. Microbaroms were first discovered by *Benioff and Gutenberg* [1939] and later mathematically described by *Longuet-Higgins* [1950].

- Severe weather: large storms and storm cells contain turbulent structures on all scales including shear winds. These huge displacements generate infrasound signals that have been detected over ranges of more than 1000 km [*Bowman and Bedard*, 1971].

- Volcanoes: the first instrumentally recorded infrasound event was the explosion of the Krakatoa near Java in Indonesia on 1883, August 27. The infrasound was recorded on traditional barographs and traveled around the world seven times [*Symons*, 1888].

■ 1.1.3 How does the atmosphere influence infrasound propagation?

Infrasound wave propagation is, in first order, dependent on the composition and wind and temperature structure of the atmosphere. The effective sound speed incorporates these effects and described by e.g. *Gossard and Hooke* [1975] and *Pierce* [1989]:

$$c_{eff} = \sqrt{\gamma_g R_c T_a} + \hat{n}_{xy} \cdot \vec{u} \qquad (1.1.1)$$

where the multiplication of the ratio of specific heats with the gas constant for air is $\gamma_g R_c$=402.8 m^{2}s^{-2}K^{-1}. The absolute temperature is given by T_a and $\hat{n}_{xy} \cdot \vec{u}$ projects the wind $\vec{u}$ in the direction from source to observer $\hat{n}_{xy}$.

The temperature decreases with altitude in the lower atmosphere, under regular atmospheric circumstances. As a result of this, sound bends upward as function of horizontal distance. Refraction of infrasound back to the surface may occur from regions where c_{eff} becomes large than its surface value. This can be caused by an increase in wind or temperature or a combined effect. Refraction follows from Snell's law and will bend infrasound back to the earth's surface.

The atmosphere is composed of 78% molecular nitrogen and 21% molecular oxygen. The remaining 1% consists of water vapor, carbon dioxide, ozone and other minor constituents. The global mean pressure and density decrease approximately exponentially with altitude. Pressure decreases from 10^5 Pa, at the surface, to 10% of that value at an altitude of 15 km. Consequently, 90% of the atmosphere's mass is present in the first 15 km altitude. The density decreases at the same rate from a surface value of 1.2 kg/m^3. The mean free path of molecules varies proportionally to the inverse of density. Therefore, it increases exponentially with altitude from 10^{-7} m at the surface to 1 m at 100 km [*Salby*, 1996].

The absorption of sound in the atmosphere is a function of frequency and decreases with decreasing frequency. The absorption in a molecular gas is caused by two different mechanisms, which are the classical and relaxation effects. The classical effects are formed by transport processes in a gas. These are molecular diffusion, internal friction and heat conduction. The latter two have the largest contribution. The relaxation effects follow from the compressional energy which is stored in the internal degrees of freedom of the molecules. It requires time to (de)excitate internal energy states which occur during collisions. The relaxation effects can be split in a vibrational and rotational component. Both the classical and relaxation effects are a function of frequency to the power of two [*Bass et al.*, 1972].

The atmosphere is divided into several layers. Naming of these layers can be based on, for example, how well mixed a certain portion of the atmosphere is. Turbulent eddies lead to a well mixed atmosphere below 100 km. Above 100 km, turbulent air motions are strongly damped and diffusion becomes the preferred mechanism for vertical transport. Above an altitude of 500 km, the critical level, molecular collisions are so rare that molecules leave the denser atmosphere into space if their velocity is high enough to escape the earth's gravitational field. Based on the above, the first 100 km is called the homosphere. Split by the homopause, the area ranging
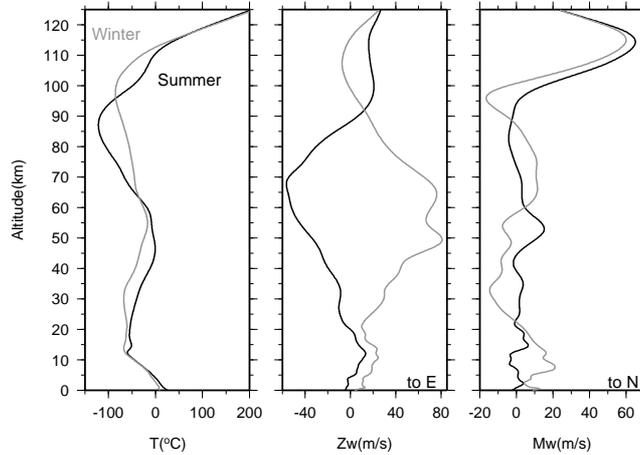
Figure 1.2: *NRL-G2S profiles for 2006, July 01 (in black) and December 01 (in gray) at 12 UTC in De Bilt, the Netherlands, at 52° N, 5° E [Drob et al., 2003].*

from 100 to 500 km is called the heterosphere. The region from 500 km upward is named the exosphere [*Salby*, 1996].

Naming can also be based on the sign of temperature gradients in different parts of the atmosphere. This is more convenient for the study of infrasound since the propagation of infrasound is partly controlled by temperature. The temperature distribution within a standard atmosphere is given in Figure 1.1. The profile shows a sequence of negative and positive temperature gradients which are separated by small regions of constant temperature. From bottom to top, the atmosphere is divided into layers called the troposphere, stratosphere, mesosphere and thermosphere, these are separated by the tropopause, stratopause and mesopause, respectively.

In the standard atmosphere, the temperature decreases with altitude in the troposphere. In a real atmosphere, a temperature inversion may occur when the temperature increases with altitude in the first 100 m up to a couple of km. After a constant temperature in the tropopause, the temperature increases in the stratosphere due to the presence of ozone. The so-called ozone layer consists of this radiatively active trace gas and absorbs UV radiation. After a decrease in temperature in the mesosphere, the temperature rises again in the thermosphere due to highly energetic solar radiation which is absorbed by very small residuals of molecular oxygen and nitrogen gases. The temperature around 300 km altitude can vary from 700 to 1600 °C depending on the solar activity.

Figure 1.2 shows the temperature and wind profiles for summer and winter in De Bilt, the Netherlands, at 52°N, 5°E. The wind is split in a West-East component that is called the zonal wind and in a South-North component, the meridional wind. The zonal wind is directed positive when blowing from the West towards the East, a
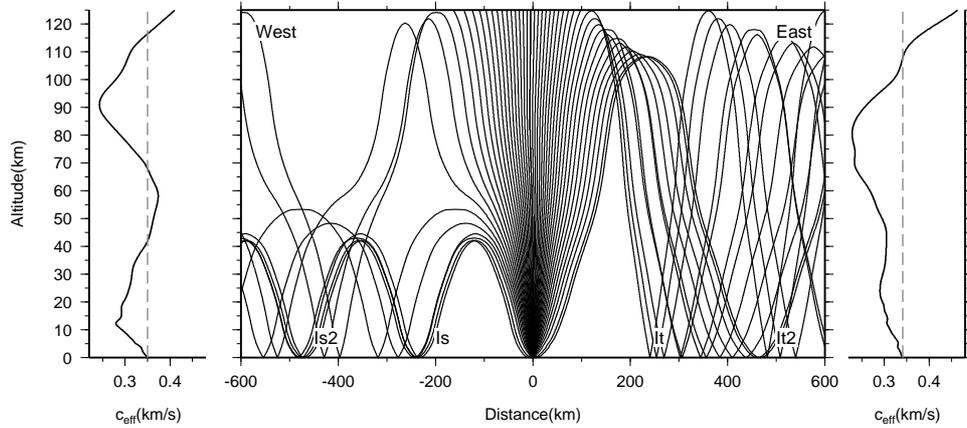
Figure 1.3: *Raytracing for a source at a distance and altitude of 0 km. Rays are shot each four degrees from the vertical to the horizontal in a westward and eastward direction through the summer situation as given in Figure 1.2. Effective speeds are given in the left and right frame, the dashed vertical line represents the effective speed at the surface.*

westerly wind. The meridional wind has a positive sign if it originates in the South. Two regions in the atmosphere are of importance for infrasound propagation, as far as wind is concerned. Firstly, the jet stream just below the tropopause, which is caused by temperature difference between the pole and equator in combination with the Coriolis force. The temperature gradient is much higher in winter than in summer. Therefore, the maximum zonal wind speed is largest in winter. The other is, the zonal mean circulation in the stratosphere. The main features, consistent with the temperature gradient from winter to summer pole, are an easterly jet in the summer hemisphere and a westerly one in winter. The maximum wind speeds of this polar vortex occur around an altitude of 60 km and are again largest in winter [*Holton*, 1979].

Figure 1.3 shows an example of raytracing [*Garcés et al.*, 1998; *Petit*, 2000] through the summer situation presented in Figure 1.2. Rays are shot from the source at a distance and altitude of 0 km, each four degrees from the vertical to the horizontal. Both westward and eastward atmospheric trajectories are given which are controlled by the effective velocity structure, see Equation 1.1.1. The effective velocity profile for westward propagation is given in the left frame of Figure 1.3, the eastward effective velocity is given in the right-hand frame. Infrasound refracts back to the surface from regions where c_{eff} increases to a value larger than the value at the surface. This surface value of c_{eff} is given by the dashed vertical line in the left and right-hand frames of Figure 1.3. The polar vortex is directed from East to West. Therefore, stratospheric refractions are predicted for energy traveling to the West. The corresponding arrivals are labeled as Is, $Is2$ indicates that two refractions have

occurred. Some thermospheric paths (It) are also present to the West. The counteracting polar vortex results in solely thermospheric arrivals towards the East.

Where Figure 1.3 only represents an West-East cross section, Figure 1.4 shows the bounce points of the rays on the earth's surface in all directions. The source is located in the center of the figure. Stratospheric arrivals (in orange) are refracted from altitudes of 45 to 55 km, while thermospheric arrivals (in red) result from refractions of altitudes between 100 and 125 km. This image is only valid for 2006, July 01 at 12 UTC for a c_{eff} at 52°N, 5°E and will change as function of time and geographical position. Therefore, Figure 1.4 also illustrates the challenge in understanding the atmospheric propagation of infrasound.

In summary, wind and temperature conditions that strongly influence infrasound propagation in the lower atmosphere are the occurrence of a temperature inversion in the troposphere and the existence of a jet stream near the tropopause. For the middle atmosphere, important conditions are the strong temperature increase within the stratospheric ozone layer and the polar vortex. Upper atmospheric propagation will be controlled by the positive temperature gradient in the thermosphere.

■ 1.1.4 Why is measuring infrasound of interest?

As mentioned before, a wide variety of sources generate infrasound, ranging from natural phenomena to man-made events, and can travel over enormous distances. Therefore, infrasonic signals contain information about these sources. Not only sources leave a fingerprint in the signals, but also the medium, i.e. the atmosphere, contributes to the recorded signature. Measuring infrasound serves the following purposes:

- To monitor the atmosphere for nuclear tests. Infrasound is a technique in the International Monitoring System (IMS) for the verification of the Comprehensive Nuclear-Test-Ban Treaty (CTBT) [*PrepCom*, 1997].

- To distinguish between vibrations caused by sources in the atmosphere and sources in the solid earth. Small earthquakes cause the same phenomena as a sonic boom, such as the rattling of windows. Identifying the source is of societal interest.

- To provide information on the state of the atmosphere. Infrasound can serve as passive atmospheric probe to derive information on wind and temperature through the whole atmosphere, up to thermospheric altitudes.

- To derive source characteristics in forensic investigations. In case of explosions, infrasound can give information on the location, origin time, yield, the number of explosions and possible precursory events.

- To monitor the possible threat of volcanic eruptions and ash. Infrasound could
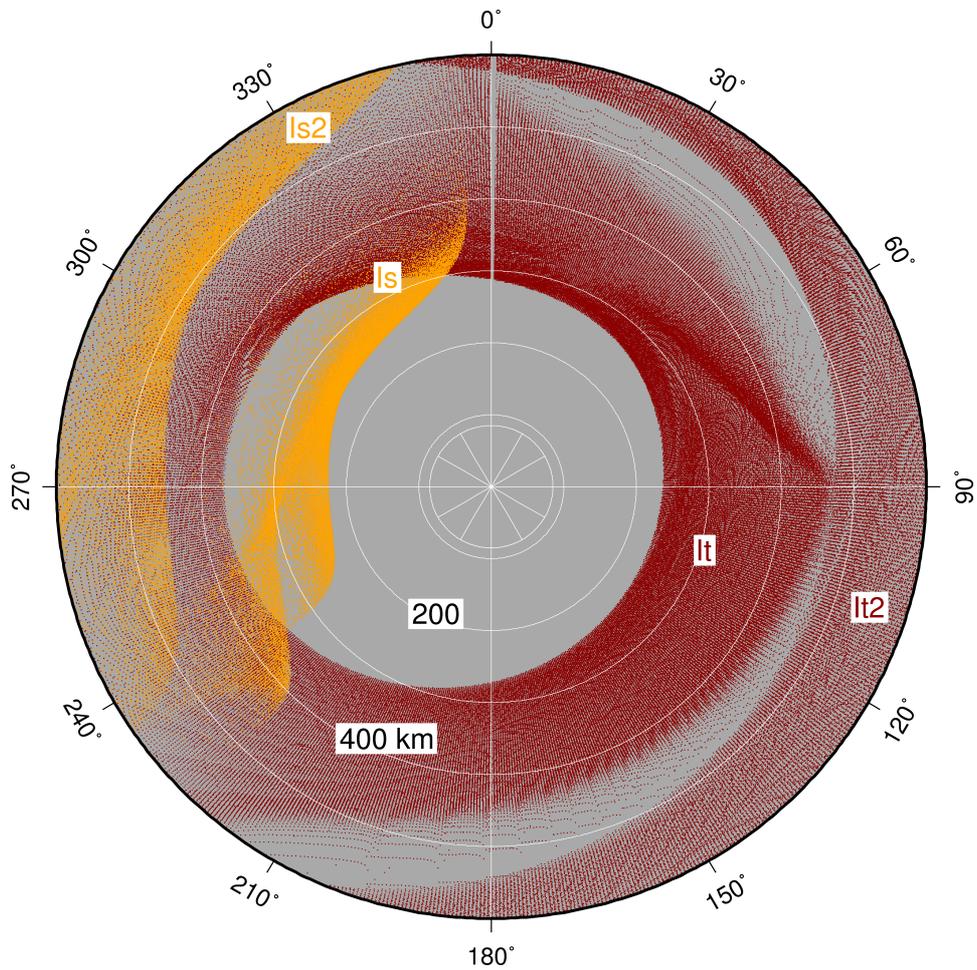
Figure 1.4: *Raytracing through the summer atmosphere from Figure 1.2 in all directions. The source is located in the center. The bounce points of the rays on the earth's surface are shown as function of distance, up to 600 km, and propagation direction. The North is located at zero degrees and the East at 90 degrees. The arrivals are labeled using the same convention as Figure 1.3, where a West (270 degrees) to East (90 degrees) cross section was shown. The stratospheric arrivals are given in orange, red is used for rays impinging on the earth's surface after being refracted and having turned in the thermosphere.*

be an additional technique to identify volcanic eruptions in an early warning system against volcanic ash, for aviation.

- To provide details on pressure fluctuations traveling with sub-sonic velocities. The developed techniques can be used to identify and quantify gravity waves which occur in the stable boundary layer. The resulting destabilization leads to uncertainties in climate models.

- To give insight in weather dependent sound propagation over large ranges. City hum and low frequency sound can be mapped, including its weather dependence, by continuously monitoring the atmosphere near, for example, airports, high- and railways.

- For military intelligence. Military activities like: super-sonic flying, usage of munitions and troop movement can be detected over large ranges. This information can be acquired locally or behind enemy lines, remotely.

1.2   Statement of problems

The study of infrasound gained much interest after World War II when it was used to monitor nuclear explosions. This period came to an end with the signature of the Limited (or Partial) Test Ban Treaty in 1963 that confined nuclear tests to underground. A lot of the research and developments from this period have been published in volume 26 from 1971 of the Geophysical Journal of the Royal Astronomical Society. This more or less marked the end of the global interest in infrasound.
A small amount of scientists stayed interested in infrasound. Among those were groups in Australia, France, the Netherlands, Sweden and the US. With the signature of the CTBT in 1996, infrasound gained renewed interest as it was chosen as one of the verification techniques. A milestone was the certification of the first IMS infrasound array in the Bavarian Forest, Southern Germany, in 2001.
Infrasound has been measured by the KNMI since 1985. The first developments concentrated on a loudspeaker mounted in wooden box. Later, arrays of electret microphones and loudspeakers were used. Signal detection was performed by a short-term average over long-term average (STA/LTA) algorithm in combination with a voting detector, while parameter estimation of events was realized through frequency-wavenumber analysis. In 1999, a project sponsored by the Royal Netherlands Air Force (KLu) was started with the title "Sonic Boom Detection Technique". This project aimed at installing a 16 element microbarometer array at an Air Force Base near the village of Deelen, the Deelen Infrasound Array (DIA). The goal was to develop a technique to record properly sonic booms and to assist the KLu in handling damage claims from sonic booms and to provide public information. A robust microbarometer was designed and more sophisticated array processing techniques were tested under this project.

The basic challenges of measuring infrasound, detecting coherent signals, character-
izing events and identifying the sources, were recognized during the construction of
DIA and its first years of operation. One challenge was the construction of a micro-
barometer and the design of appropriate arrays. As arrays became operational, it
appeared that a lot of coherent infrasound was present in the atmosphere. At very
low detection thresholds thousands of events per day could be detected. Here, the
challenge was to extract events of interest and identify the sources. Source identi-
fication can partly be realized through localization, but the dynamic nature of the
atmosphere makes this a demanding task. The recorded waveforms can differ highly
from array to array and several sources can be present at the same time from various
directions and at different distances.

Identifying sources of infrasound involves a measurement system, processing tech-
nique, knowledge on the influence of the atmosphere and the source time functions,
which generally states the problems addressed in this thesis.

1.3   Research objectives

Based on the statement of problems, the following objectives have been defined:

- To develop a technique to measure infrasound. This includes the construc-
  tion of an instrument and proper configuration of arrays to reduce noise and
  characterize the signals.

- To use signal detectors and array processing techniques. Relevant signals
  should be extracted from the continuous recordings, and parameters, like back
  azimuth, should be retrieved.

- To apply the measurement, detection and processing techniques. To prove the
  functionality of the complete system by identifying sources of infrasound. Here,
  knowledge on the state of the atmosphere is essential because it determines
  the propagation characteristics.

1.4   Outline of the thesis

This thesis describes the complete sequence from measurement to processing, to the
interpretation of infrasound data. This involves the development of a sensor, acqui-
sition system and arrays to measure infrasound. With continuous data becoming
available, signal detection and parameter estimation is performed by applying array
processing techniques. The performance of the system is evaluated by identifying
sources of infrasound while including atmospheric propagation effects.

Chapter 2 describes how infrasound signals are acquired by making use of a micro-
barometer. This microbarometer was developed at KNMI and is capable of measur-

ing the very small air-pressure fluctuations associated with infrasound. The response of the microbarometer is described both theoretically and experimentally. Arrays of microbarometers are deployed to reduce noise, mainly due to wind, and to character-ize the signals. Chapter 2 describes the considerations for configuring an appropriate array and illustrates its performance. Infrasound is measured continuously with a variety of arrays. Chapter 2 also describes the applied array processing techniques for detecting coherent signals which possibly are events of interest. Furthermore, parameter estimation is achieved through beamforming to determine the event's slowness or back azimuth and apparent sound velocity. The processing techniques are based on Fisher statistics, both in the time and frequency domain

Several sources will be identified in the next chapters to illustrate the capabilities of the measurement system and processing techniques. These studies often relate to the application of infrasound as monitoring technique. Meteors are one of the few natural impulsive sources mimicking a nuclear test in terms of yield. The treat-ment of these sources is described in Chapter 3. Small sized meteors interfere with background noise from microbaroms and need careful processing since their yield is in the range of the lower threshold for nuclear test monitoring. Their dynamic character can be used to distinguish meteors from static explosive sources. Here, knowledge of atmospheric properties like wind and temperature are important to derive an appropriate effective velocity model.

The detectability of infrasound depends on the array configuration, i.e. the num-ber of sensors, inter-station distances and aperture. This sensitivity is addressed in Chapter 4 in a practical case study based on volcanic infrasound from Mt. Etna (Italy) observed in the Netherlands in July 2001. Not only the array configuration controls the detectability, also the state of the boundary layer influences the signal coherency.

Ground truth events in the study of infrasound are rare. Most natural sources lack an accurate origin time and/or source location. More knowledge on the source can often be obtained or derived from man-made or accidental events. In Chapter 5, infrasound from incidental chemical explosions is used to asses the accuracy of sig-nal identifiers and location procedures. The combination of infrasound and seismic signals in a so-called seismo-acoustic analysis proved useful in forensic investiga-tions on origin time, location and yield. The associated precisions highly depend on knowledge of the atmosphere as a whole, since infrasound probes the atmosphere up to thermospheric altitudes.

Chapter 6 concludes with summarizing the major findings described in this thesis. Furthermore, possible topics of further research and new applications are given in an outlook.

2

Measurement and processing of infrasound data

2.1 The KNMI microbarometer

■ 2.1.1 Design and construction

The infrasonic frequency range of interest is 0.002 to 20 Hz and can be measured by either making a microphone low frequency or a barometer high frequency. Microphones tend to be sensitive to moisture and will, therefore, degrade during the required continuous operation. Furthermore, the response of most commercially available microphones will severely drop at frequencies lower than 10 Hz. As an alternative, low frequency loudspeakers, woofers, can be used to measure infrasound if mounted in a box. But these also suffer from the lack of durability in outdoor operations and sensitivity at very low frequencies. Consequently, it was chosen to adapt a barometer to higher frequencies and make it more sensitive to small air pressure fluctuations. A barometer typically measures air pressure fluctuations in the order of 100 hPa and samples the atmosphere every 1 to 10 seconds. In the infrasound application the measurement device should be capable of resolving fluctuations in the order of 10^{-2} Pa and sample at at least 40 Hz.

Figure 2.1 shows a schematic overview of the microbarometer developed by the KNMI. The atmosphere is sampled through the inlet box to which a commercial pressure sensor is attached. Validyne Eng. fabricates pressure sensors sensitive to very low fluctuations. These so-called ultra, or very low range, differential pressure transducers come in various sensitivities. Within the microbarometer, type DP-103 (ultra low, 0.022 to 0.35 kPa at ± 10 Vdc Full Scale) and DP-45 (very low, 0.14
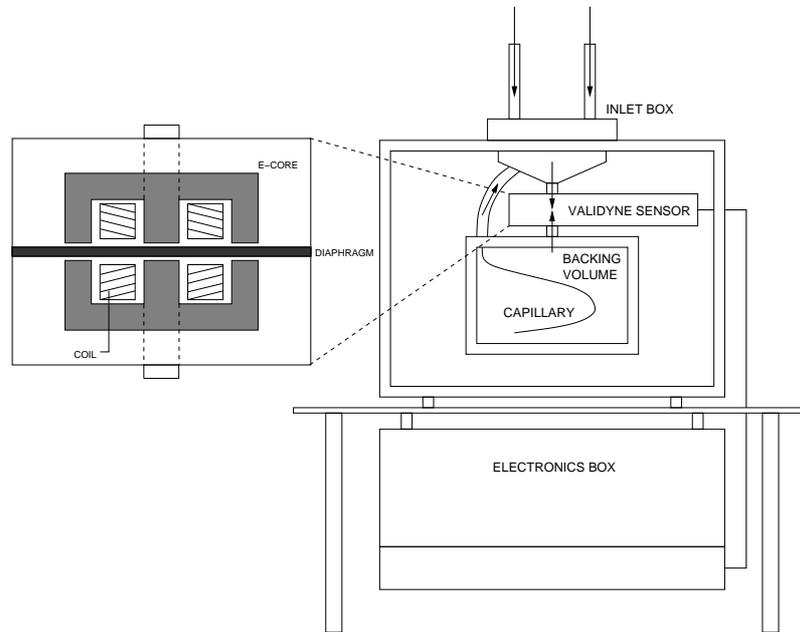
Figure 2.1: *Schematic overview of the KNMI microbarometer. The atmosphere is sampled through the inlet box where pressure fluctuations are measured by the Validyne sensor. A backing volume is attached to the sensor to construct a differential instrument. Within the backing volume, an acoustical resistance, i.e. capillary, is mounted to "leak" very low frequency pressure fluctuations back to the atmosphere. Various elements of the Validyne sensor are shown in the inlay being the e-cores, coils and diaphragm.*

to 0.35 kPa FS) are deployed. The natural frequency of the sensor is 600 Hz which is far above the upper limit of the frequency range of interest. The inset in Figure 2.1 shows the details of the pressure sensor. The pressure sensing diaphragm is mounted between coils and free to move in response to differential pressure. The coils are matched and wired in series in an inductive half-bridge. The coils are fed with an AC excitation to create a magnetic flux. Movement of the diaphragm will lead to a change in coil impedance which, in turn, will bring the half-bridge out of balance. An AC signal will appear directly proportional to the applied pressure. The phase of the signal is determined by the direction of movement of the diaphragm. The coils are enclosed within two e-like shaped cores to close the magnetic circuit.

A backing volume is attached to the pressure sensor. Thus, a differential microbarometer has been created capable of measuring over the whole frequency range of atmospheric pressure fluctuations, also those of meteorological origin. A low frequency cut-off is realized by including a leak in the backing volume. This leak consists of a thin capillary that acts as acoustic resistance, redirecting fluctuations

$P_A + P_e$

R INLETS AND
NOISE REDUCER

CAPILLARY V $P_A + P$ FORE VOLUME

b

r DIAPHRAGM

BACKING VOLUME

v $P_A + p$
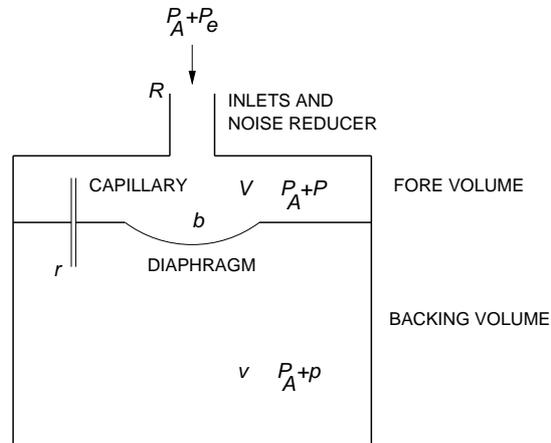
Figure 2.2: *Schematic drawing of the microbarometer adapted after Burridge [1971]. Two volumes V and v are connected by a high acoustic resistance r. The atmosphere is sampled through the noise reducers and inlets that have a low acoustic resistance R. An external pressure P_e is applied to the system. The observed pressure difference $\Delta P_{obs} = P - p$, with respect to the ambient pressure P_A, is sensed by the diaphragm that undergoes a volume change b as function of this pressure.*

with too long periods back to the atmosphere. The length and diameter of the capillary and the size of the backing volume determine the low frequency cut-off.

Additional electronics are needed to supply the sensor with power and to read and transmit the out-coming signal. This electronics board is mounted in a separate box below the sensor. In a later version of the microbarometer, the electronics are included in the same box as the sensor.

Detailed constructional drawings of the KNMI microbarometer can be found in Appendix B.

■ 2.1.2 Theoretical microbarometer response

Burridge [1971] derived the theoretical response for a microbarograph. Figure 2.2 shows the different elements of the microbarometer. The fore volume of size V is connected to the atmosphere which has an ambient pressure P_A. The atmosphere is sampled through the inlets and an additional analog noise reducer with a low acoustical resistance R. A backing volume is present of size v. A pressure difference between the two chambers is sensed by the diaphragm of the Validyne sensor. In the work of *Burridge* [1971], pressure-sensitive bellows were used to sense the pressure difference. The volume change as function of pressure within the Validyne sensor is denoted by b. The backing volume is connected to the fore volume by a high

acoustic resistance r, i.e. the capillary. An external pressure of size P_e results in an observed pressure difference of $\Delta P_{obs} = P - p$ between the fore and backing volume. The phase and amplitude of this difference are detected by the diaphragm.

The air initially occupying the fore and back volume is perturbed by the external pressure P_e. By evaluating Boyle's law, differentiated with respect to time, *Burridge* [1971] derived the theoretical microbarometer response as function of frequency ω, as:

$$D = \frac{\Delta P_{obs}}{P_e} = \frac{i\omega}{P_A\left[\beta + i\omega\alpha + \frac{i\omega RV}{P_A}(B + i\omega A)\right]} \tag{2.1.1}$$

where

$$\alpha = \frac{1}{P_A} + \frac{b}{v}, \qquad \beta = \frac{1}{rv} \tag{2.1.2}$$

$$A = \frac{1}{P_A} + b\left(\frac{1}{V} + \frac{1}{v}\right), \qquad B = \frac{1}{r}\left(\frac{1}{V} + \frac{1}{v}\right) \tag{2.1.3}$$

The described response has a lower and upper frequency limit. At low frequencies, large volumes and high acoustic resistances will control the behaviour of the instrument. The small volumes and low acoustic resistances will dominate at high frequencies. Equation 2.1.1 can be rewritten as:

$$D = \frac{1}{\frac{P_A\beta}{i\omega} + P_A\alpha + \frac{RVB}{P_A} + \frac{i\omega ARV}{P_A}} \tag{2.1.4}$$

The first and last term in the denominator of equation 2.1.4 contain frequency ω; the middle two terms are constants. At low frequencies, the first term will dominate. Thus, the response in the low frequency limit is:

$$D \sim \frac{i\omega rv}{P_A} \tag{2.1.5}$$

The second term is important at high frequencies, leading to:

$$D \sim \frac{1}{i\omega RV\left[\frac{1}{P_A} + b\left(\frac{1}{V} + \frac{1}{v}\right)\right]} \tag{2.1.6}$$

As expected, the low frequency response is controlled by the large backing volume v and the capillary as high acoustic resistance r. The small fore volume V and inlets, with a low acoustic resistance R, determine the high frequency response.

■ 2.1.3 The low frequency cut-off

Theoretical derivation

The low frequency cut-off f_l of the KNMI microbarometer is controlled by the characteristics of the capillary and the size of the backing volume. The acoustical resistance

of the capillary r is described by:

$$r = \frac{P}{dv/dt} \qquad (2.1.7)$$

with, P as pressure and dv/dt represents a volume change with time. Equation 2.1.7 is equivalent to Ohm's law for the electrical resistance R as function of voltage V and current I, being $R = V/I$. Poiseuille's law couples the resistance of a flow through the capillary to its length l and radius a, by:

$$r = \frac{8l\eta}{\pi a^4} \qquad (2.1.8)$$

where the viscosity η equals 18.27 μPa s at 18°C. Equation 2.1.8 is valid for small pressure fluctuations with respect to the background pressure, which is generally true for acoustics waves in the atmosphere. The capillary is characterized by a=0.1 mm and l=10 cm, resulting in a r of 4.65x10^{10} kg m^{-4}s^{-1}.

The low-frequency cut-off f_l of a system can be written, by using of the relaxation time τ, as:

$$f_l = \frac{1}{2\pi\tau} \qquad (2.1.9)$$

The corresponding value is known as the -3 dB point or the level at which the amplitude has decreased with e^{-1}. In electronics, $\tau = RC$ is known as the RC-time of a circuit which contains a resistance R and a capacitance C. Equivalently, equation 2.1.9 is used to determine the frequency cut-off of, for example, an analog filter.

From equation 2.1.5 and 2.1.9 it follows that:

$$f_l \sim \frac{P_A}{2\pi r v} \qquad (2.1.10)$$

This equation also shows the analogy of the acoustic resistance r and electrical resistance R and that of a volume v and capacitance C. The low frequency cut-off of the microbarometer is theoretically determined with equation 2.1.10, as $f_l \sim$3.5x10^{-3} Hz with v=100 ml and P_A=1.01325x10^5 Pa.

Experimental determination

The low frequency cut-off can also be determined experimentally as described by *Evers and Haak* [2000]. In essence, the relaxation time of the instrument is measured after a sudden over- or under-pressure, i.e. the impulse response. The relaxation of the diaphragm is described by *Haak and de Wilde* [1996] and follows the relation:

$$\frac{P_t}{P_0} = \frac{V_t}{V_0} = e^{-\alpha t} \qquad (2.1.11)$$
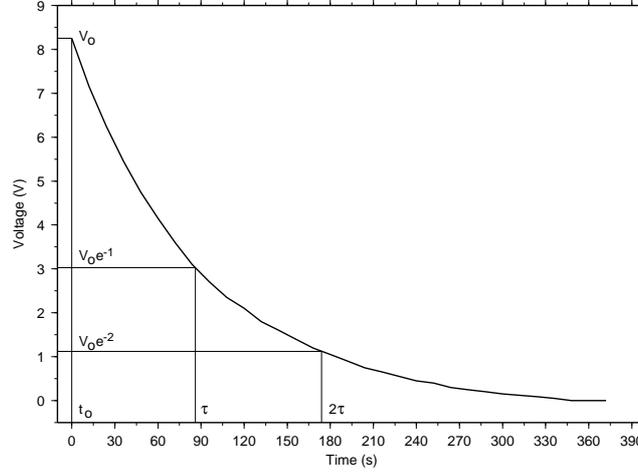
Figure 2.3: *Response of the microbarometer to a sudden under-pressure. The relaxation time, τ, can be derived at various levels, n, of $V_0 e^{-n\tau}$.*

where, P_0 represents the over-pressured starting situation which is relaxed in time t. Within the sensor, pressure variations, P_t, are directly proportional to voltage variations V_t. The capillary controls the time necessary to reach an equilibrium, between the open air and backing volume, by a constant α. The relaxation time τ is defined as the time necessary to let the amplitude decay to e^{-1}, the -3 dB point, from which it follows that:

$$e^{-\alpha t} = e^{-1} \rightarrow \alpha = 2\pi f_l = \frac{1}{\tau} \qquad (2.1.12)$$

Figure 2.3 shows the results of the relaxation experiment obtained after suddenly opening one of the inlets of the microbarometer. It follows from this experiment and that the low frequency cut-off equals: $1.85\pm0.01\text{x}10^{-3}$ Hz. This value was again obtained with a capillary of 0.1 mm radius and length of 10 cm, within a backing volume of 100 ml. The period of the instrument can be increased by increasing the acoustical resistance of the capillary by, for example, increasing its length or decreasing the diameter.

The theoretically and experimentally derived low frequency cut-off differ because of the strong dependence on the diameter a of the capillary. In equation 2.1.8, a is present to the fourth power. Therefore, small variations in the diameter of 0.1 mm will have a large influence on the low frequency cut-off.

Table 2.1: *Sizes of the microbarometer's components, acoustical resistances and volume change*

	size
length capillary	$10\text{x}10^{-2}$ m
diameter capillary	$0.1\text{x}10^{-3}$ m
r: resistance	$4.65\text{x}10^{10}$ kg m^{-4}s^{-1}
length inlet	$6\text{x}10^{-2}$ m
diameter inlet	$10\text{x}10^{-3}$ m
R: resistance	279 kg m^{-4}s^{-1}
volumetric displacement pressure cavity	$4.9\text{x}10^{-8}$ m^3
at DP-103 Full Scale	$0.35\text{x}10^3$ Pa
b: volume change	$1.4\text{x}10^{-10}$ m^{3}Pa^{-1}
v: backing volume	$100\text{x}10^{-6}$ m^3
V: fore volume	$22.1\text{x}10^{-6}$ m^3

■ 2.1.4 Response of the KNMI microbarometer

The amplitude and phase response of the microbarometer are given in Figure 2.4. The sizes of different components, as input for this calculation, are listed in Table 2.1. In this table, values are derived for the acoustical resistances r and R, and volume change b. The amplitude is calculated by taking the absolute value of D (equation 2.1.1); the phase follows from the argument of D. The black line is the theoretical response. The gray line represents the true response which was experimentally determined for the low frequency cut-off.

The theoretical response is flat up to a high value of the angular frequency ω. The high frequency cut-off of $9.2\text{x}10^6$ rad/s, or $1.5\text{x}10^6$ Hz, is far above the infrasonic upper frequency limit of 20 Hz. However, this theoretical value will not be reached in practice, because:

- A noise reducer will be attached to the system to sample the atmosphere (see Section 2.1.5), and will act as a low-pass filter at higher frequencies. Typically, this filter will attenuate frequencies higher than 50 Hz, depending on the size of the noise reducer.

- The natural frequency of the Validyne sensor is 600 Hz, which leads to resonances at and around this frequency. Furthermore, a Helmholtz resonator has been created by combining an inlet and fore volume. This resonance is around 400 Hz, using the geometric values given in Table 2.1.

From the phase response, it becomes clear that the microbarometer differentiates signals with a very low frequency content. This will lead to a 90 degrees, or $\frac{\pi}{2}$,
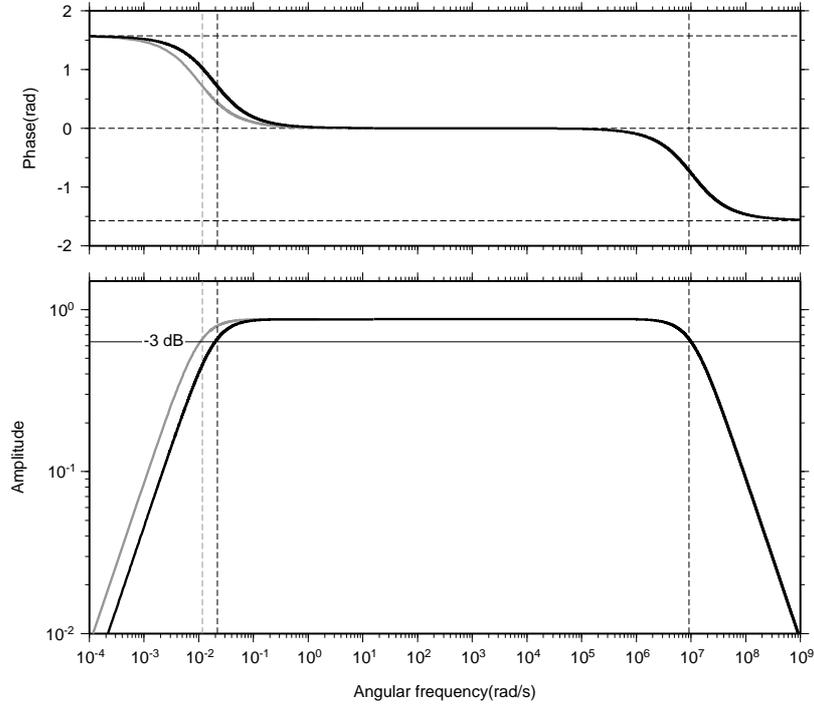
Figure 2.4: *The amplitude and phase response of the KNMI microbarometer as function of the angular frequency ω. The black line represents the theoretical response based on equation 2.1.1. The gray line is the true response experimentally determined for the low frequency cut-off. The −3dB points are given by the intersections of the dashed line.*

phase shift of the recorded signals. Therefore, signals recorded at these very low frequencies should be corrected for the instrument's response. This correction can be approximated by integrating the signal [*Christie et al.*, 1978].

The sensitivity of the microbarometer was determined by a simple calibration experiment [*Evers and Haak*, 2000]. The microbarometer was vertically displaced over a certain distance h. The induced pressure variation ΔP and vertical distance are related through:

$$\Delta P = \rho g h \qquad (2.1.13)$$

with the density of air ρ and gravitational acceleration g. The instrument was displaced over known distances multiple times, which resulted in an average value for the sensitivity of 5.65×10^{-2} Pa/mV.

More details on the microbarometer response will become available in *Mentink and Evers* [2008].
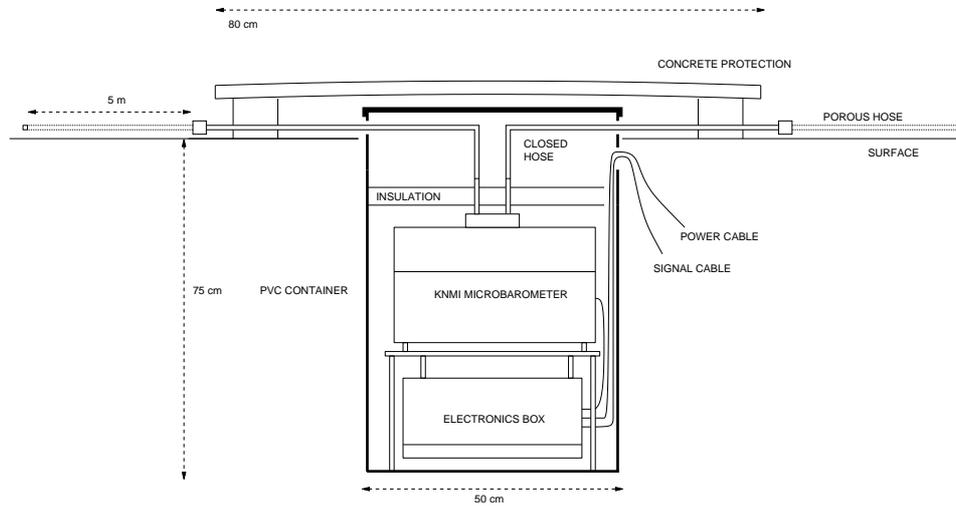
Figure 2.5: *Typical installation of the KNMI microbarometer as element of an infrasound array. The microbarometer is installed in a watertight PVC tube beneath the surface. Next to its subsurface mounting, Styrofoam plates are placed within the tube to ensure temperature stability. Porous hoses and cables are tightly connected through cable swivels. Additional protection is obtained by a concrete cover also serving as supplemental insulation device.*

■ 2.1.5 Field installation

The microbarometer is installed below the earth's surface in a watertight PVC tube (Figure 2.5). Subsurface mounting is important to ensure temperature stability. The microbarometer is a differential pressure sensor and, therefore, sensitive to temperature fluctuations. Mainly temperature fluctuations with periods smaller than 500 s will affect the pressure in the backing volume and lead to a notable signal within the frequency range of interest. Further insulation is achieved by placing Styrofoam plates in the tube and the placement of a concrete cover which also serves as protection. Temperature measurements inside the PVC tube have shown no correlation between the measured temperature and pressure fluctuations for periods less than at least 1000 s [*Mentink and Evers*, 2008]. A power and signal cable are connected to the microbarometer through cable swivels.

The measurement of infrasound is affected by noise from wind. Typically, between 1 and 10 Hz winds will affect the infrasound signals of interest. Therefore, analog filters are applied that use the large coherency length of infrasound versus the short coherency length of wind to improve the signal-to-noise ratio of the recording. By sampling the atmosphere over an area rather than at one point, incoherent wind is canceled out while the infrasonic signal remains unaffected. Figure 2.6 shows an analog filter constructed with six porous or soaker hoses of 5 m length in a star-like

Figure 2.6: *Installation of a microbarometer in DIA. The microbarometer is installed beneath the earth's surface and covered by a concrete top. The atmosphere is sampled by six porous hoses in a star-like layout, each of 5 m length.*

configuration. Impermeable hoses of 1.5 m are used close to the instrument, to avoid sampling of a possible coherent wind field. Other such filters can consist of pipes [*Daniels*, 1950] and [*Daniels*, 1959] or pipe arrays with discrete inlets [*Hedlin et al.*, 2003]. Wind barriers are also applied and can be constructed of wood [*Liszka*, 2008] or porous shade cloth [*Christie*, 2007]. The spatial design of noise reducers depends on the infrasonic freqeuncy range of interest and the expected wind speeds [*Wilson et al.*, 2007]. The spatial coherence of the wind field increases with increasing wind speeds but remains only a small fraction the coherence of the infrasonic wave [*Shields*, 2005].

Both signal and power cables originate from a central facility where 27 VDC/2 A is provided as power to the microbarometers. Here, the analog signals are also collected. The analog signals are converted to digital by a National Instrument's 16 bits analog-digital converter (ADC) board mounted in a Linux driven PC. The board is accessed through free driver software made available at www.comedi.org and incorporated in a data acquisition program. The signals are accurately time stamped, i.e. at sub-sample rate values, by a GPS clock provided by Meinberg Funkuhren GmbH & Co., that is also accessible under Linux. The data can be accessed, all year round (24/7), through TCP/IP protocols like secure shell (ssh) and the file
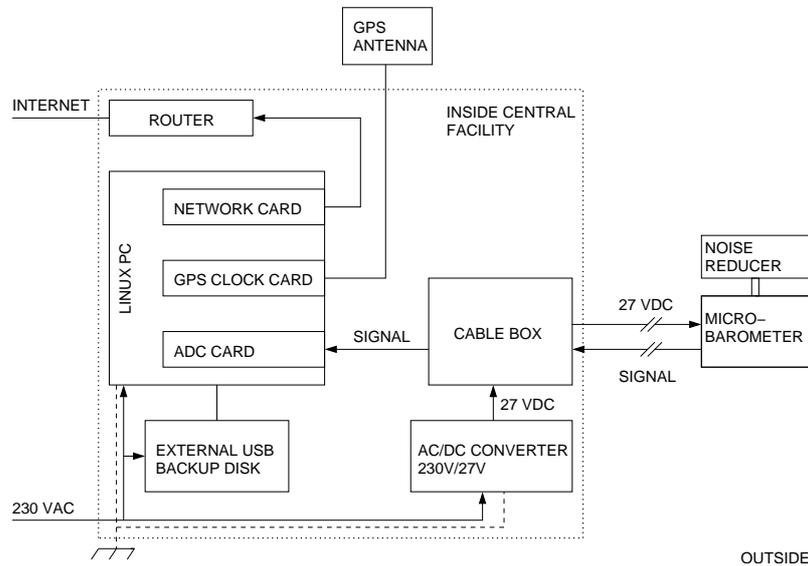
Figure 2.7: *Architecture of a typical infrasound measurement system. The various components both in- and outside the central facility are shown.*

transfer protocol (ftp) or pushed from a remote site to the user over the Internet. All components of the infrasound measurement system, both in- and outside, are summarized in Figure 2.7.

2.2   Arrays for infrasound measurements

Infrasound is measured with arrays of microbarometers. These arrays reduce noise through signal summation, ideally leading to $1/\sqrt{N}$ increase in signal-to-noise ratio, in case of uncorrelated noise, where N is the number of array elements. Furthermore, array processing techniques enable the characterization of the signal in terms of back azimuth and apparent sound speed. In the first section, the array response will be derived, which forms the basis for array design. For this purpose, beamforming and the frequency-wavenumber spectral density will be introduced. These will also be applied later in array processing.

■ 2.2.1   Beamforming array response pattern

An infrasound array consists of N microbarometers in a limited aperture. The reconstruction of the wavefield is affected by this spatial discretization since the atmosphere is not sampled infinitely.

Assume we have a monochromatic three-dimensional wavefield of unit amplitude described by:

$$g(t, \vec{r}) = e^{i(2\pi f_0 t - \vec{k}_0 \cdot \vec{r})} \tag{2.2.14}$$

with frequency f_0, traveltime t, wavenumber $\vec{k}_0 = (k_{0x}, k_{0y}, k_{0z})$ at position $\vec{r} = (x, y, z)$.

The Fourier transform of this signal is given by:

$$G(f, \vec{r}) = \int_{-\infty}^{\infty} g(t, \vec{r}) e^{-i2\pi f t} dt \tag{2.2.15}$$

being

$$G(f, \vec{r}) = \delta(f - f_0) e^{-i\vec{k}_0 \cdot \vec{r}} \tag{2.2.16}$$

A wavefield can be characterized by means of a spectral density function. This is a frequency-wavenumber (f/k) spectral density function for propagating waves, or a homogeneous random field. Such a f/k spectral density function provides information on the process as a function of frequency and the vector velocities of propagating waves [*Capon*, 1969]. The f/k density function for the assumed planar wavefield, is defined as (see e.g. [*Denholm-Price and Rees*, 1999]):

$$G(f; k_x, k_y) = \int_{-\infty}^{\infty} \int_{-\infty}^{\infty} G(f, \vec{r}) e^{i(\vec{k} \cdot \vec{r})} dx dy \tag{2.2.17}$$

with: $\vec{k} = (k_x, k_y)$ and the positions $\vec{r} = (r_x, r_y)$ located at $z = 0$, i.e. the earth's surface.

By using the result of the Fourier transform (2.2.16), the f/k spectral function becomes:

$$G(f, \vec{k}) = \delta(f - f_0) \delta(k_x - k_{0x}) \delta(k_y - k_{0y}) \tag{2.2.18}$$

The maximum value of $G(f, \vec{k})$ is found at $(f_0, \vec{k}_0)$.

Arrays of microbarometers discretely sample the wavefield above the array in two dimensions. Spatial sampling is controlled by N sensors located at positions $\vec{r}_j = (x_j, y_j)$, while the sample rate Δ determines the temporal sampling. The discrete form of the frequency-wavenumber power spectrum of the acquired data is defined [*Smart and Flinn*, 1971]:

$$P(\omega, \vec{k}) = \sum_{j=1}^{N} \sum_{m=1}^{N} w(\vec{r}_j) w(\vec{r}_m) S_{jm}(\omega) e^{i\vec{k} \cdot (\vec{r}_j - \vec{r}_m)} \tag{2.2.19}$$

where $P(\omega, \vec{k})$ represents an estimate for the f/k power spectrum, $S_{jm}(\omega)$ is the cross-spectrum between the jth and mth sensor as function of ω, which is the angular frequency and equals $2\pi f$. If it is assumed that all instruments are equally sensitive to the plane wave than $w(\vec{r}_j) = w(\vec{r}_m) = 1$.

The Fourier transform $G(f, \vec{r})$ (equation 2.2.15) can be written as $A_j(\omega)e^{i\varphi_j(\omega)}$ which contains the amplitude and phase information of the signal in the frequency domain for the jth sensor. The cross-spectrum between the jth and mth sensor can then be written as:

$$S_{jm}(\omega) = A_j(\omega)e^{-i\varphi_j(\omega)} \cdot A_m(\omega)e^{i\varphi_m(\omega)} \tag{2.2.20}$$

which follows from the correlation theorem for real signals $h_1(t)$ and $h_2(t)$, generally stated as:

$$C(h_1, h_2) \iff H_1(f)H_2^*(f) = H_1(f)H_2(-f) \tag{2.2.21}$$

where $H_2^*(f)$ is the complex conjugate of $H_2(f)$.

It follows from the substitution of equation 2.2.20 in 2.2.19 that:

$$P(\omega, \vec{k}) = \sum_{j=1}^{N} A_j(\omega)e^{-i[\varphi_j(\omega) - \vec{k}\cdot\vec{r}_j]} \sum_{m=1}^{N} A_m(\omega)e^{i[\varphi_m(\omega) - \vec{k}\cdot\vec{r}_m]} \tag{2.2.22}$$

By using:

$$P(\omega, \vec{k}) = \sum_{j=1}^{N} c_j^* \sum_{m=1}^{N} c_m = C^*C = |C|^2 = \left| \sum_{n=1}^{N} c_n \right|^2 \tag{2.2.23}$$

the double summation can than be rewritten as a single summation:

$$P(\omega, \vec{k}) = \left| \sum_{n=1}^{N} G(\omega, \vec{r}_n)e^{-i\vec{k}\cdot\vec{r}_n} \right|^2 \tag{2.2.24}$$

The result found in equation 2.2.16 is now used to find the estimate for $G(\omega, \vec{k})$, being:

$$P(\omega, \vec{k}) = [\delta(\omega - \omega_0)]^2 \left| \sum_{n=1}^{N} e^{-i(\vec{k} - \vec{k}_0)\cdot\vec{r}_n} \right|^2 \tag{2.2.25}$$

Ideally, the best estimate for $G(\omega, \vec{k})$ is found for the limit of $N \to \infty$:

$$\sum_{n=1}^{\infty} e^{-i(\vec{k} - \vec{k}_0)\cdot\vec{r}_n} \to \delta(\vec{k} - \vec{k}_0) \tag{2.2.26}$$

which means that the atmosphere is regularly sampled with an infinitely long array. With this result, we define the array response as:

$$R(\omega, \vec{p}) = \left| \frac{1}{N} \sum_{n=1}^{N} e^{-i\omega[(\vec{p} - \vec{p}_0)\cdot\vec{r}_n]} \right|^2 \tag{2.2.27}$$

with:

$$\vec{p}_0 = \frac{1}{\omega}(k_{0x}, k_{0y}) \tag{2.2.28}$$

$R(\omega, \vec{p})$ is called the beamforming array response pattern [*Capon*, 1969], or spatial window function [*Lacoss et al.*, 1969] or array transfer function [*Denholm-Price and Rees*, 1999].

Beamforming is performed in the two-dimensional slowness ($\vec{p} = \frac{\vec{k}}{\omega}$) domain to resolve the apparent sound speed c_{app} and back azimuth ϕ, through:

$$|\vec{p}| = \frac{1}{c_{app}} \tag{2.2.29}$$

$$p_x = |\vec{p}| \cos \phi \tag{2.2.30}$$

$$p_y = |\vec{p}| \sin \phi \tag{2.2.31}$$

Figure 2.8 shows an inclined wavefront in three spatial dimensions (x,y,z) traveling over a three element planar array, located at the earth's surface, i.e. the xy-plane. The back azimuth ϕ is the angle between the propagation direction of the wave in the xy-plane, given by the vector $\hat{n}_{xy}$, and the North. The back azimuth is measured clockwise and gives the direction where the wave originates with respect to the receiver. In the example of Figure 2.8, ϕ equals 300°, which means a source located to the northwest of the array.

The effective sound speed c_{eff}, see equation 1.1.1, takes into account both the effect of temperature and wind on the velocity of an infrasonic wave. Therefore, the effective sound speed is the propagation velocity of the inclined wavefront in the xyz-space, see Figure 2.8. The microbarometers measure a velocity in the xy-plane which is called the apparent sound speed c_{app}. The apparent and effective sound speed are related through the inclination θ, as $c_{app} = \frac{c_{eff}}{\cos \theta}$.

There are two extreme cases in beamforming, as follow from equations 2.2.29 through 2.2.31:

- $\vec{p} = 0$, $c_{app} = \infty$ and $\theta = 90°$: all instruments measure the waveform at the same time. This infinite c_{app} means that there are no traveltime differences over the array. The source will be located right above the array in the case of a planar wave.

- $c_{app} = c_{eff}$ and $\theta = 0°$: the wavefront travels parallel ($\hat{n}$ is in the same direction as $\hat{n}_{xy}$) to the earth's surface, or to the xy-plane in which the instruments are located. The c_{app} equals c_{eff} which is also the lowermost possible value for c_{app}. Only, for non-acoustic waves, like gravity waves, can c_{app} be become smaller than c_{eff}.
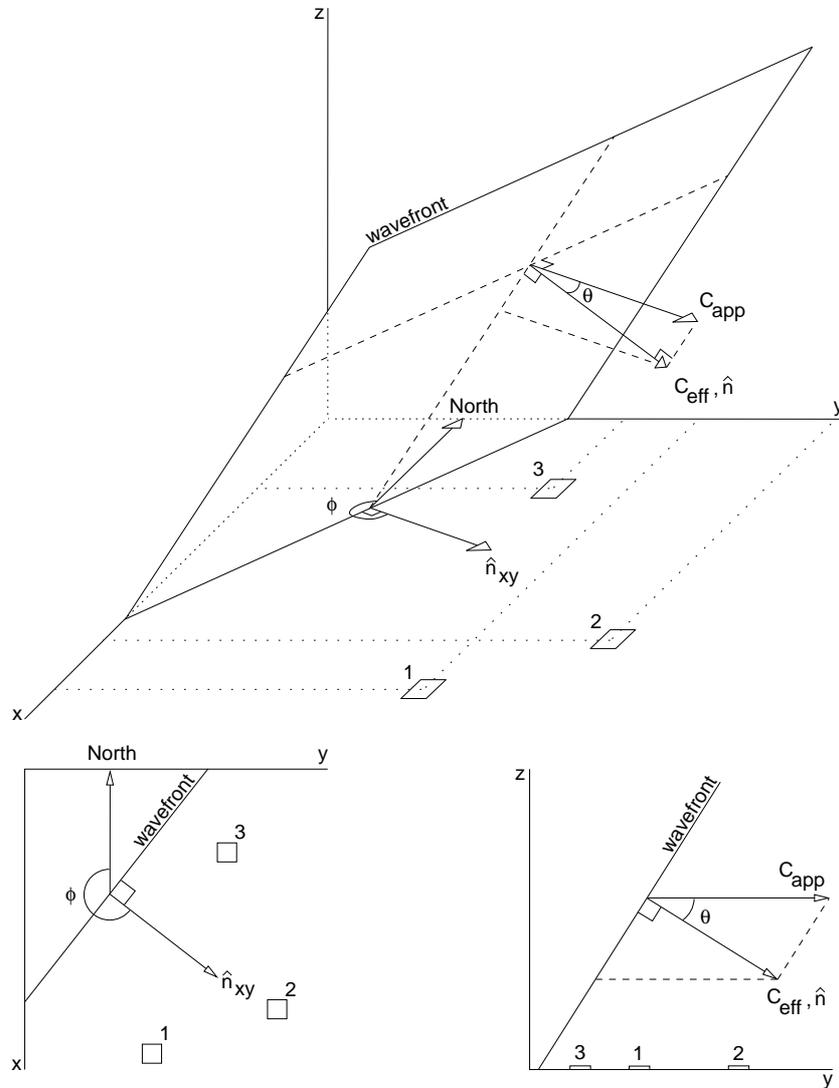
Figure 2.8: *An inclined wavefront traveling over an array of three microbarometers located on the earth's surface, i.e. xy-plane. The projection of the wavefront normal $\hat{n}$ on the xy-plane is indicated by $\hat{n}_{xy}$. The back azimuth ϕ is the clockwise angle between the propagation direction of the wave in the xy-plane, represented by the vector $\hat{n}_{xy}$, and the North. The effective sound speed c_{eff} is the velocity with which the wave propagates through the air, i.e. in the xyz-space, and is directed normal $\hat{n}$ to wavefront. The apparent sound speed c_{app} is the velocity of the wavefront as measured by the microbarometers in the xy-plane. The apparent and effective sound speed are related through the inclination θ with $c_{app} \geq c_{eff}$.*
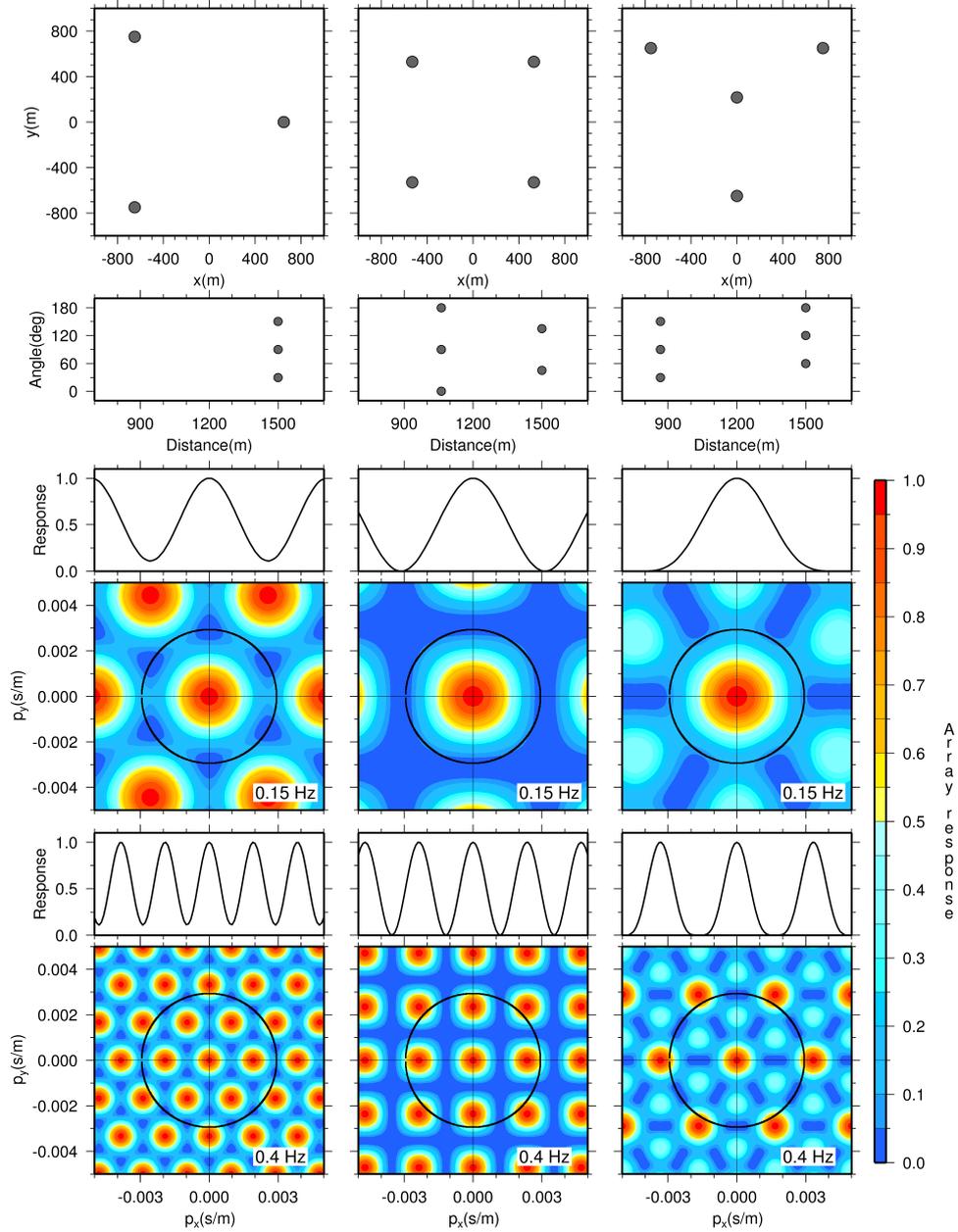
Figure 2.9: *The columns show array layouts and their response patterns for simple three and four element configurations. A vertical incident planar wave, i.e. $c_{app} = \infty$ and $\theta = 90°$, peaks in the center of the graph. The top frame displays the array layout for array apertures of 1500 m. The amount of distances and angles between the elements are given in the next frames. In the lower four frames, the array responses are plotted for 0.15 and 0.4 Hz. The cross sections are also given at $p_y = 0$. The black circles in the response patterns represent an apparent sound speed of 340 m/s (on the black circle $c_{app} = c_{eff}$ and $\theta = 0°$) defining the slowness interval of interest for infrasound.*

■ 2.2.2   Array design

The temporal resolution is controlled by the sampling rate Δ, leading to a Nyquist frequency of $f_N = 1/2\Delta$ which is the highest recoverable frequency given this digitization in time. Frequencies higher than f_N will be aliased. Typical sample frequencies in infrasound measurements are in the order of 1 to 200 Hz, depending on the frequency range of interest.

Similarly, the resolution of an array is determined by the configuration and also limited by aliasing. A source cannot uniquely be identified if this so-called spatial aliasing occurs. In such a case, multiple solutions will exist for the apparent sound speed and back azimuth. In practice, the sensors within an array are placed such that $R(\omega, \vec{p})$ in equation 2.2.27 approximates a delta function around the desired slowness $\vec{p}_0$ [*Lacoss et al.*, 1969]. This discretization in space is realized by varying three parameters to design an optimal array, the diameter or aperture of the array, the number of sensors and the inter-sensor distances [*Haubrich*, 1968]. The lowest frequency that can be resolved by the array is determined by its aperture. The number of sensors and inter-sensor distances control the amount of spatial aliasing. The simplest and most effective three element planar array is realized when the sensors are placed at the corners of an equilateral triangle. The left column of Figure 2.9 shows the layout and array response patterns for 0.15 and 0.4 Hz. Also given are the number of inter-sensor distances, one in this case, and the number of angles present between the elements. The distance between a pair of sensors is is calculated by $\sqrt{(\Delta x^2 + \Delta y^2)}$. The angle between a pair of sensors is calculated by taking the absolute value of tangent of Δy and Δx. Both distance and angle are plotted for all possible sensor pairs in the second row from the top of Figure 2.9. As the aperture of the array and frequency range of operation scale linearly, this figure is valid for the whole range of acoustic frequencies. The black circle in response patterns represents a c_{app} of 340 m/s. The cross section right above the pattern shows the response at $p_y = 0$. The main lobe of the response, at $p_x = p_y = 0$, has a circular shape. This means that the array has no preferred orientations and will be equally sensitive in all directions. Side lobes are present near the main lobe and both are of equal size which will lead to spatial aliasing. This effect is clearly visible when the frequency is increased from 0.15 to 0.4 Hz and numerous lobes of unit amplitude are present in the slowness domain of interest, making it impossible to identify the main lobe.

If the number of sensors is increased from three to four, it seems logical to put them equidistantly on a circle. The middle column of Figure 2.9 shows the capabilities of such a circular array. The side lobes have moved somewhat away from the main lobe due to the increase in the number of inter-station distances and angles. This array will perform better over a wider range of frequencies than the triangular one. Although a circular array may seem appropriate, a more effective array can be constructed from four elements being a triangle with a central element. The right column in Figure 2.9 shows the layout and responses for this array. Nearby side lobes only have 50% of the amplitude of the main lobe. Spatial aliasing is avoided almost up to 0.4 Hz when the first unit amplitude side lobes come in the slowness

range of interest. The effect of increasing the number of inter-station distances and angles is hereby illustrated. The accuracy of the parameter estimation of infrasound arrays can be quantified by evaluating the distributions of the slowness estimates, which are event-specific [*Szuberla and Olson*, 2004].

To summarize the above, the number of inter-station distances plays a decisive role in reaching an optimal array in the Fraunhofer approximation. These should allow for a wide range of distances, i.e. small and large, and various angles. The largest distance within the array determines the lowest frequency that can be resolved. Therefore, the general design criteria are:

- The main lobe has a circular shape. This means that the array is equally sensitive to all infrasonic arrivals, independent of its back azimuth.

- The main lobe is as small ("peaked") as possible. The inclination and back azimuth will be resolved with the maximum accuracy since energy is minimally smeared out.

- Side lobes are small in amplitude. Most energy is present in the main lobe, enabling maximum resolution and avoiding spatial aliasing.

- Side lobes are as far away from the main lobe as possible. The main lobe will be unambiguously identified and spatial aliasing will be avoided.

■ 2.2.3 Infrasound arrays in the Netherlands

Several arrays of microbarometers have been or are operational in the Netherlands. Figure 2.10 shows five infrasound arrays with various layouts and number of elements. The exact coordinates of the arrays and the microbarometer positions are listed in Appendix C.

The De Bilt Infrasound Array (DBN) was installed in 1991 and is situated on a measurement terrain near KNMI. In its early years, DBN consisted of low frequency loudspeakers (woofers) mounted in an air tight PVC container. This design was based on the work of *Benioff and Gutenberg* [1939]. Later, electret microphones were applied, capable of measuring infrasound down to 1 Hz. Circular rings of PVC tube were used for noise reduction where discrete inlets sampled the atmosphere [*Haak*, 1996]. These rings were 314 cm in diameter and had 20 equally spaced inlets of 0.08 cm diameter. During 2002, DBN was upgraded with microbarometers to be able to measure longer periods, i.e. 500 s, of infrasound. Furthermore, microbarometers are far more rugged for outdoor operation than loudspeakers or microphones, of which the performance degrades under the influence of moisture. DBN is capable of estimating an event's slowness down to a frequency 1 Hz, with a limited aperture of 80 m. All microbarometer arrays use porous hoses for noise reduction.

The Witteveen Infrasound Array (WIT) became operational halfway through the nineties and also consisted of electrets in PVC rings with discrete inlets. Even
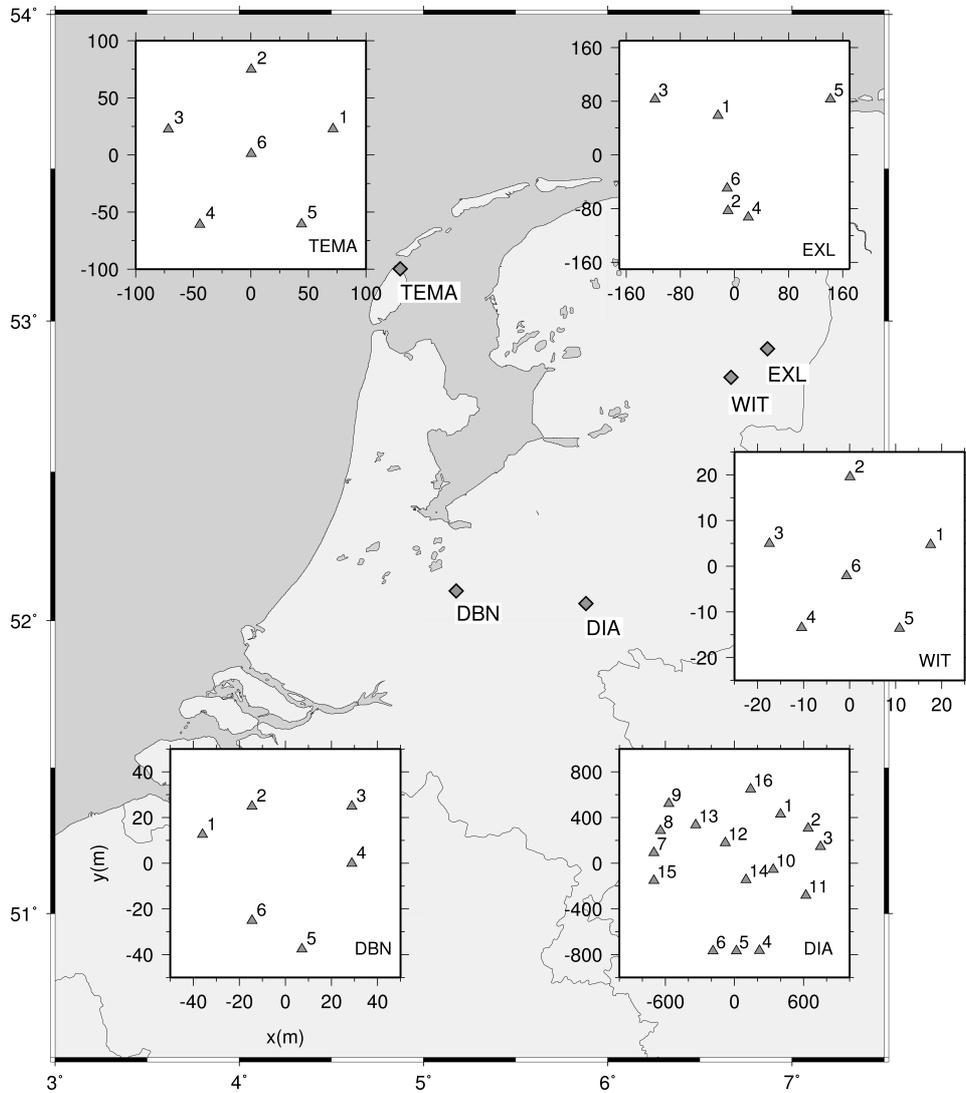
Figure 2.10: *The locations of the infrasound arrays in the Netherlands. The array layouts are given in separate inlays. The coordinates of the arrays and various microbarometer positions configuring the arrays can be found in Appendix C.*
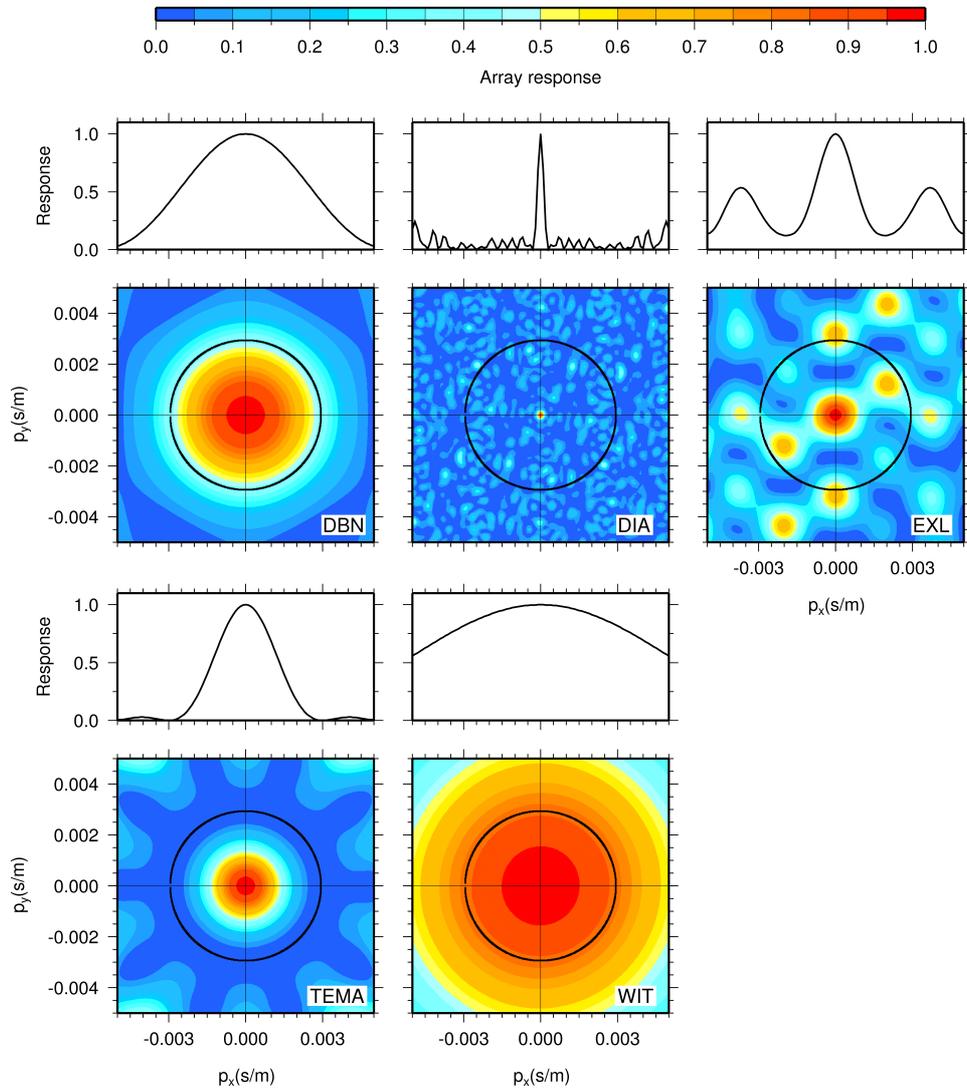
Figure 2.11: *Array responses of the infrasound arrays to a planar wave of 2 Hz. The wide variety of number of array elements and apertures causes different response patterns.*

smaller in size than DBN, this array could mainly be used for short range infrasound detection. Typically, sonic booms from military fighters above the North Sea could be localized by cross bearing the results of DBN and WIT. During 2002, WIT was also upgraded with microbarometers for the same reasons as given above.

The Deelen Infrasound Array (DIA) was funded by the Royal Netherlands Air Force and built in 1999. DIA was designed to detect sonic booms, based on the experience with DBN and WIT. Furthermore, the unique configuration of DIA enabled research to support the CTBT. The number of instruments of the first IMS arrays were four to five, while DIA consisted of 16 microbarometers. DIA is built on Air Force base Deelen and its layout is controlled by the local infrastructure. The microbarometers are installed in close vicinity of roads and landing strips. Therefore, instruments like number 4, 5 and 6 follow a straight line. Because of its size, DIA is currently the most low frequency array going down to frequencies of 0.05 Hz.

In 2004, the Texel Experimental Monitoring Array (TEMA) was constructed on one of the Dutch islands. This array specifically aimed at detecting military practices at a neighboring island that cause nuisance to the citizens of Texel. Mainly, the usage of munitions can generate infrasound of tens of pascals which can easily be detected under the right meteorological conditions. Furthermore, the islands are one of the windiest places of the Netherlands, ideally suited for testing noise reduction systems.

The Exloo Infrasound Array (EXL) was installed in collaboration with an astronomical initiative called Low Frequency Array (LOFAR). The aim of LOFAR is to create a sensor network in the northern part of the Netherlands consisting of radio-astronomical sensors, seismometers, microbarometers and equipment for high-precision farming, consisting of sensors for e.g. temperature and moisture measurements. EXL became operational in 2005 and its close vicinity to WIT made WIT for the time being obsolete. EXL was designed with a genetic algorithm, which optimized the usage of the asymmetrical terrain in obtaining the largest aperture.

The response patterns of the arrays are given in Figure 2.11 and are calculated for a monochromatic plane wave of 2 Hz. Clearly, the wide variety of number of instruments and array apertures gives different patterns. In general, the smaller the array, the broader its main lobe. The two extremes are DIA with an aperture of 1500 m and WIT with only 35 m. Where DIA starts approaching the desired delta function at 2 Hz, WIT is totally incapable of direction finding. All arrays are designed such that they have a circular main lobe, guaranteeing unbiased omni-directional operation characteristics.

2.3 General concept of infrasound data processing

Array processing is based on the detection of coherent signals and subsequent estimation of specific parameters to characterize the event. Infrasonic signals are continuously acquired at a rate of 40 samples per second and a detection algorithm

is applied to find possible events of interest. Such detectors can perform in the time domain in search of correlated signals. Two correlation detectors are commonly used in infrasound data processing, being the Fisher detector [*Melton and Bailey*, 1957] and the Progressive Multi Channel Correlation technique, PMCC [*Cansi*, 1995]. Signal detection can also be achieved in the frequency domain, where signal coherency is used to trigger a detection [*Smart and Flinn*, 1971]. A comparison between the Fisher detector and the PMCC technique has been made by *Caljé* [2005]. It was concluded that the lower threshold for Fisher detection corresponds to a signal-to-noise power ratio of 0.05, which appeared to be 0.2 for the PMCC method.

The Fisher detector analyzes variances within measurements and is based on the work described by *Fisher* [1948]. *Melton and Bailey* [1957] introduced the F-ratio which has been used in seismological studies by *Blandford* [1974] and more recently by *Heyburn and Bowers* [2007]. Based on experiences from seismology, Fisher detection has been proposed for the processing of infrasound data by *Brown et al.* [2002a] and has successfully detected sources like meteors and oceanic waves [*Evers and Haak*, 2001b].

As introduced in Chapter 2, beamforming is applied to sample the atmosphere above the array in all directions of interest. Parameters are estimated for a specific beam when a certain detection threshold is reached, i.e. an event is detected. The primary parameters are apparent sound speed and back azimuth. Other event-specific parameters are frequency contents, amplitude and signal-to-noise ratio.

The following steps give an overview of the processing sequence:

- Read the raw data. A filter can be applied before reading to concentrate on a specific frequency range, for example, a second order Butterworth band-pass filter. Any DC offset or linear trend should be removed from the data because the Fourier transform would than be dominated by low-frequency components.

- Split the data in overlapping time segments, i.e. bins, if long time series are to be evaluated. In real-time processing, data are split in 50% overlapping bins with the length being at least the traveltime of a wave over the array. Doing so, it is ensured that a coherent wave, traveling over the array, is included in the bin.

- Define a slowness $\vec{p}$, see equations 2.2.29 through 2.2.31, interval of interest. Typically, a grid of 50x50 points is defined in the slowness range of -0.005 to 0.005 s/m. The apparent velocity on such a grid varies between sub-acoustic velocities and infinity, which covers the apparent acoustic velocities.

- Perform beamforming for each pair of (p_x, p_y) and run a detector on each beam. All 2500 time or phase differences are evaluated. These 2500 operations should be multiplied by the number of frequencies in the case of a frequency domain detector. The one that explains the time or phase differences in the data best will lead to the highest detector value. The slowness, or apparent sound speed

and back azimuth, for this beam will be stored, after which the next time segment can be evaluated.

- Construct a best beam. The sum of all time aligned traces for the slowness at the maximum detector value is called the best beam. This can either be done for each bin or for the maximum detector value from a set of bins. Incoherent noise will cancel out and the signal will, consequently, be enhanced. The apparent sound speed and back azimuth are known at the maximum detector value. The events are characterized.

■ 2.3.1   Time domain Fisher analysis

The Fisher detector was first described by *Melton and Bailey* [1957] and aims to detect a coherent signal traveling over an array of sensors. This work was based on the analysis of variances [*Fisher*, 1948] of both noise and signal that are present in the recordings. *Blandford* [1974] successfully applied the F-detector to seismic array data, as was later done by *Heyburn and Bowers* [2007]. Applying a F-detector is attractive because of its well-known statistical distribution. In this section the approach of *Melton and Bailey* [1957] and *Olson* [2004] will be followed to derive the F-ratio, where in essence a statistical hypothesis is tested.

A statistical test is a set of rules whereby a decision about a hypothesis is reached. The null hypothesis that is being tested is designated H_0. An alternative hypothesis H_1 will be accepted when H_0 is rejected. The decision rules in the test are with respect to the rejection or non-rejection of H_0. If the decision rules reject H_0 when in fact H_0 is true, the rules lead to an incorrect decision, called false alarm. The probability of making this so-called type 1 error is controlled by the chosen level of significance or threshold. A type 2 error is made when the rules do not reject H_0 when in fact H_1 is true [*Winer*, 1962].

The hypothesis to be tested H_0 is that all recordings made by the microbarometers consist of uncorrelated noise. The alternative hypothesis H_1 is valid for the case that not only noise is present but also signal. Evaluated are the variance of the noise σ^2 and the variance σ_α^2, which can not be attributed to the noise since it is common to all signals. Table 2.2 summarizes the effects of the decisions made in the statistical test based on the F-ratio. If the decision is made to reject H_0 while H_0 is true, a type 1 error is made. Thus, a false alarm is given since the recordings consist of noise, i.e. $\sigma_\alpha^2 = 0$, while the corresponding hypothesis is rejected. A missed event is the situation in which a coherent infrasonic wave traveled over the array but was not detected. In this case, the decision is made not to reject H_0 while H_0 was false, i.e. $\sigma_\alpha^2 > 0$. The central F-distribution represents the situation in which only noise is present. If signal is present, the non-central F-distribution will follow which is guided by the non-centrality parameter. The general concept described above will be applied in more detail to infrasound array recordings.

Assume an array of $n = 1, ..., N$ microbarometers that measure the air-pressure fluc-

Table 2.2: *Statistical test and the errors, adapted after Winer [1962]. H represents a hypothesis, $E(F)$ the expected value of the Fisher ratio and σ_α^2 a variance.*

	H_0 true	H_0 false H_1 true
Reject H_0	Type 1 error False alarm	No error
Do not reject H_0	No error	Type 2 error Missed event
	$\sigma_\alpha^2 = 0, E(F) = 1$	$\sigma_\alpha^2 > 0, E(F) > 1$

tuations over a certain time segment (or bin) $t = 1, ..., T$. Consider these recordings to be arranged in matrix form where each row represents a recording and each column the output of all sensors at a certain time. Thus, each row consists of T samples while each column contains N recordings, forming an $N \times T$-matrix.

Beamforming is applied to the recordings of air pressure fluctuations in each row by time-shifting. The mean of each column can be written as:

$$\bar{x}_t = \frac{1}{N} \sum_{n=1}^{N} x_{nt} \tag{2.3.32}$$

where x_{nt} are the time-shifted recordings of the air-pressure fluctuations and is considered Gaussian distributed.

The data consist of the recordings and an error signal ϵ_{nt}. The recordings differ from the mean by an error signal ϵ_{nt} as: $x_{nt} = \bar{x}_t + \epsilon_{nt}$. It is assumed that the error signals are normally distributed with a zero mean and variance σ^2.

The mean of all samples equals, or grand average, is:

$$\bar{x} = \frac{1}{NT} \sum_{t=1}^{T} \sum_{n=1}^{N} x_{nt} \tag{2.3.33}$$

This mean also represents the bias in the recordings. Variations on time scales longer than the signal period are considered DC offsets. If the traces have non-zero means, $\bar{x}$ can be used to remove these. This leaves only the departures from $\bar{x}$ in the data which are the AC inputs, i.e. the signals of interest.

The deviation of each column from the grand average is: $\alpha_t = \bar{x}_t - \bar{x}$. The data model can then be written as: $x_{nt} = \bar{x} + \alpha_t + \epsilon_{nt}$. A null hypothesis is formed stating that the samples x_{nt} of each row consist of noise, thus $\alpha_t = 0$. To test this hypothesis against the alternative hypothesis that $\alpha_t \neq 0$ requires the construction of a F-ratio. To evaluate the F-ratio, the total variation in the recording is considered, which is

the sum of the residuals, being [*Spiegel and Stephens*, 2008]:

$$V_T = \sum_{t=1}^{T} \sum_{n=1}^{N} (x_{nt} - \bar{x})^2 \tag{2.3.34}$$

which can be written as (see Appendix D.1):

$$V_T = V_W + V_B \tag{2.3.35}$$

with

$$V_W = \sum_{t=1}^{T} \sum_{n=1}^{N} (x_{nt} - \bar{x}_t)^2 \tag{2.3.36}$$

and

$$V_B = N \sum_{t=1}^{T} (\bar{x}_t - \bar{x})^2 \tag{2.3.37}$$

V_W is the variation within a recording. V_B is the variation between the recordings. Variations in both noise and signal are evaluated in V_W since each sample x_{nt} is compared with the average $\bar{x}_t$. The result is a measure of noise power. In V_B, variations in each recording average $\bar{x}_t$ are compared to the grand average $\bar{x}$. Here, the variation common to all recordings is evaluated and the results is a measure of signal power.

The expected values of the variations are:

$$E(V_W) = T(N-1)\sigma^2 \tag{2.3.38}$$

and

$$E(V_B) = (T-1)\sigma^2 + N \sum_{t=1}^{T} \alpha_t^2 \tag{2.3.39}$$

and

$$E(V_T) = (TN-1)\sigma^2 + N \sum_{t=1}^{T} \alpha_t^2 \tag{2.3.40}$$

The degrees of freedom $T-1$ for the expected value of V_B follow from the summation over time T. The expected value of V_W has $N-1$ degrees of freedom which is the result of the summation over the recordings N. Since the summed recordings in V_W are averaged over time, the degrees of freedom become $T(N-1)$.

An unbiased estimate of σ^2 is, thus, given by:

$$E\left(\frac{V_W}{T(N-1)}\right) = \sigma^2 \tag{2.3.41}$$

whether or not H_0 is true.

On the other hand, only when H_0 is true, i.e. $\alpha_t = 0$, will:

$$E\left(\frac{V_B}{T-1}\right) = \sigma^2 \tag{2.3.42}$$

and

$$E\left(\frac{V_T}{TN-1}\right) = \sigma^2 \qquad (2.3.43)$$

If H_0 is not true, equation 2.3.42 will be biased positively because $\sigma_\alpha^2 > \sigma^2$.
We define the F-ratio:

$$F = \frac{V_B/(T-1)}{V_W/T(N-1)} \qquad (2.3.44)$$

The expected value of this F will be greater than one if H_1 is true, i.e. $E(F) > 1$. F has an expected value of one if H_0 is true, i.e. $E(F) = 1$ (see Table 2.2). This F-ratio can be written in the form of *Melton and Bailey* [1957], as (see Appendix D.2):

$$F = \frac{T(N-1)}{N(T-1)} \frac{\sum_{t=1}^{T}(\sum_{n=1}^{N} x_{nt})^2 - \frac{1}{T}(\sum_{t=1}^{T}\sum_{n=1}^{N} x_{nt})^2}{\sum_{t=1}^{T}\sum_{n=1}^{N} x_{nt}^2 - \frac{1}{N}\sum_{t=1}^{T}(\sum_{n=1}^{N} x_{nt})^2} \qquad (2.3.45)$$

which is a realization of a random variable because x_{nt} are random variables. *Melton and Bailey* [1957] also derived a relation between signal-to-noise (snr) power ratio on the traces and F, being:

$$F = N \cdot snr + 1 \qquad (2.3.46)$$

In general, V_B and V_W are characterized by two χ^2 distributions with $T-1$ and $T(N-1)$ degrees of freedom. Therefore, the F-ratio is characterized by a F-distribution with $\nu_1 = T-1$ and $\nu_2 = T(N-1)$ degrees of freedom. The central F-distribution $F(\nu_1, \nu_2)$ represents the case if only noise is present. If signal is present, the non-central F-distribution $F(\nu_1, \nu_2, \lambda_{nc})$ will follow which is guided by the non-centrality parameter $\lambda_{nc} = \nu_1 \cdot snr$ [*Shumway*, 1971], with snr as signal-to-noise power ratio on the beam. Figure 2.12 shows an example of the central and non-central F-distribution. The missed event and false alarm rate are determined by the chosen detection threshold.

The F-distributions become more peaked, more symmetrical and separated for a larger number of samples T (or time segment). This effect can be seen in Figure 2.13. The average value for the central F-distribution then becomes:

$$E(F) = \frac{\nu_2}{\nu_2 - 1} \simeq 1 \qquad (2.3.47)$$

and for the non-central F-distribution:

$$E(F) = \frac{\nu_2(\nu_1 + \lambda_{nc})}{\nu_1(\nu_2 - 2)} \simeq snr + 1 \qquad (2.3.48)$$

with snr on the beam. *Heyburn and Bowers* [2007] presented a practical method for determining the upper and lower bounds of λ_{nc} by taking into account the confidence intervals for the non-central F-distributions.
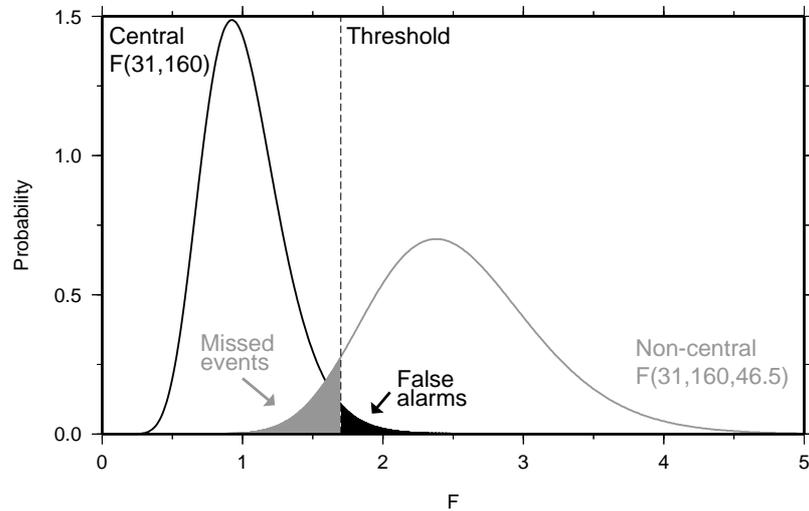
Figure 2.12: *The central $F(\nu_1, \nu_2)$ and non-central F-distribution $F(\nu_1, \nu_2, \lambda_{nc})$, for $T = 32$, $N = 6$ and $snr = 1.5$ as function of F. The missed event and false alarm rate are indicated by the shaded areas for a chosen detection threshold of $F = 1.7$.*
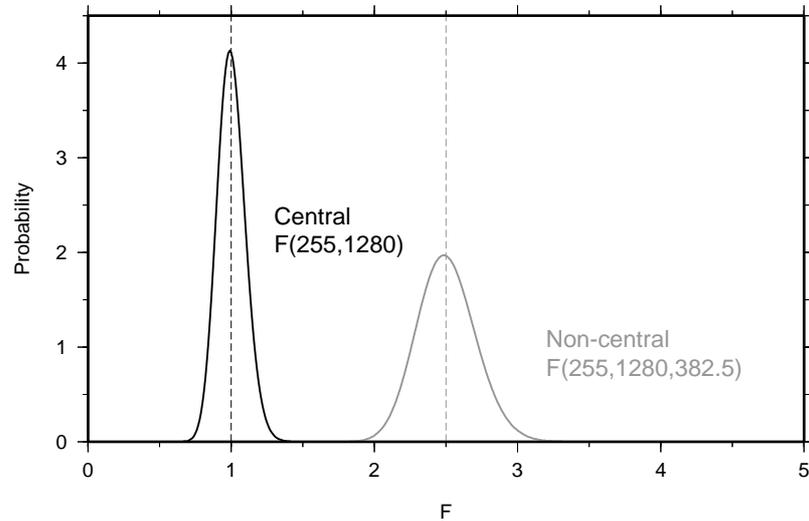
Figure 2.13: *The central $F(\nu_1, \nu_2)$ and non-central F-distribution $F(\nu_1, \nu_2, \lambda_{nc})$, for $T = 256$, $N = 6$ and $snr = 1.5$ as function of F. The average value of the central and non-central F-distribution are indicated by the dashed lines.*

■ 2.3.2   Frequency domain Fisher analysis

Smart and Flinn [1971] derived the Fisher statistic on the basis of frequency-wave-number (f/k) spectra. The f/k power spectral density function, equation 2.2.17, for a single frequency can be estimated by:

$$P(\omega, \vec{k}) = \left| \sum_{n=1}^{N} G(\omega, \vec{r}_n) e^{-i\vec{k}\cdot\vec{r}_n} \right|^2 \qquad (2.3.49)$$

where, $G(\omega, \vec{r}_n)$ is the Fourier transform of the time-shifted recordings x_{nt} (equation 2.2.15). $G(\omega, \vec{r}_n)$ contains information on the signal's amplitude and phase and $e^{-i\vec{k}\cdot\vec{r}_n}$ is related to the array response.

The integral expression for the f/k density function in equation 2.2.17 is estimated by 2.3.49 since the infrasonic wavefield is both discretely sampled in space and time. Temporal resolution is limited by Nyquist frequency, while spatial resolution is controlled by the array response. In the presence of signal, equation 2.3.49 represents the signal power and can be written as:

$$P_S(\omega, \vec{k}) = \left| \frac{1}{N} \sum_{n=1}^{N} G(\omega, \vec{r}_n) e^{-i\vec{k}\cdot\vec{r}_n} \right|^2 = \frac{1}{N^2} P(\omega, \vec{k}) \qquad (2.3.50)$$

The total amount of energy, in terms of power, contained in the recordings is given by:

$$P_T(\omega) = \frac{1}{N} \sum_{n=1}^{N} |G(\omega, \vec{r}_n)|^2 \qquad (2.3.51)$$

which includes both noise and signal.

The F-ratio is a measure of *snr* power ratio, therefore the F-ratio is defined as [*Shumway*, 1971]:

$$F(\omega, \vec{k}) = \frac{P_S(\omega, \vec{k})}{P_T(\omega) - P_S(\omega, \vec{k})} (N - 1) \qquad (2.3.52)$$

where, the noise in the denominator is represented by the total energy minus the signal power.

As in the time domain analysis, equation 2.3.52 is evaluated for each beam. The Fisher statistic also needs to be extracted for each frequency, for each beam. The number of frequencies returned by the Fourier transform depends on the length of the input time segment (bin size) or the number of samples. Computational efforts can be reduced by summing a set of frequencies and calculate the average Fisher statistic at the central frequency. Further reduction can be obtained by limiting the total frequency band of interest. For example, it is not always necessary to evaluate equation 2.3.52 up to the Nyquist frequency.
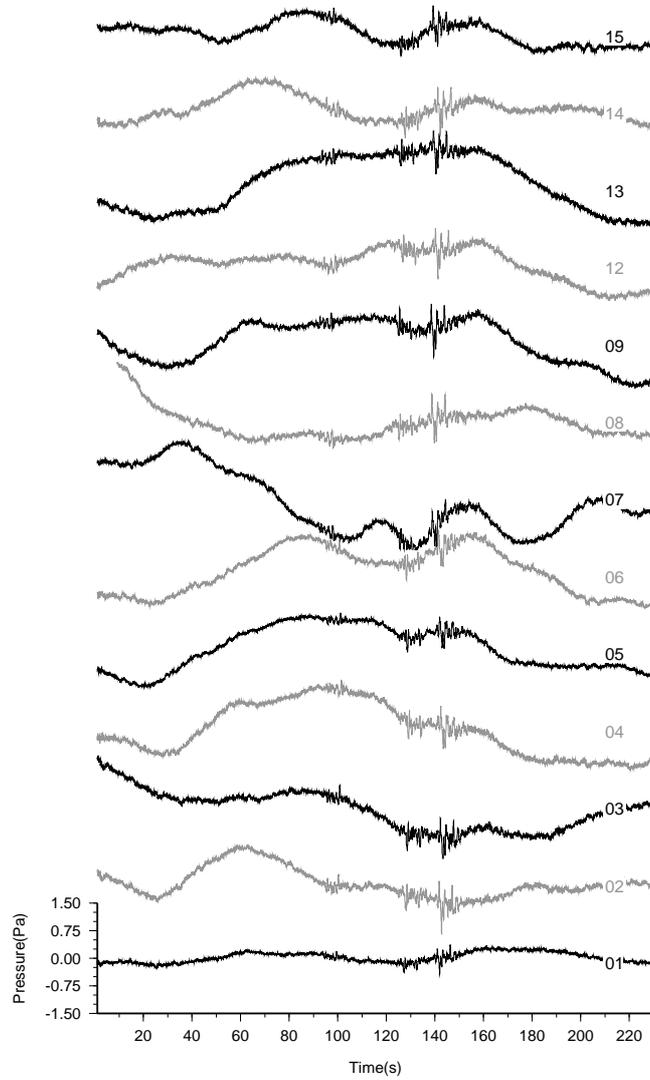
Figure 2.14: *Raw recordings at DIA. The time axis starts on 2007, September 04 at 20h03m18.475s UTC. A coherent signal with high frequencies is visible on all traces superposed on low frequency energy.*
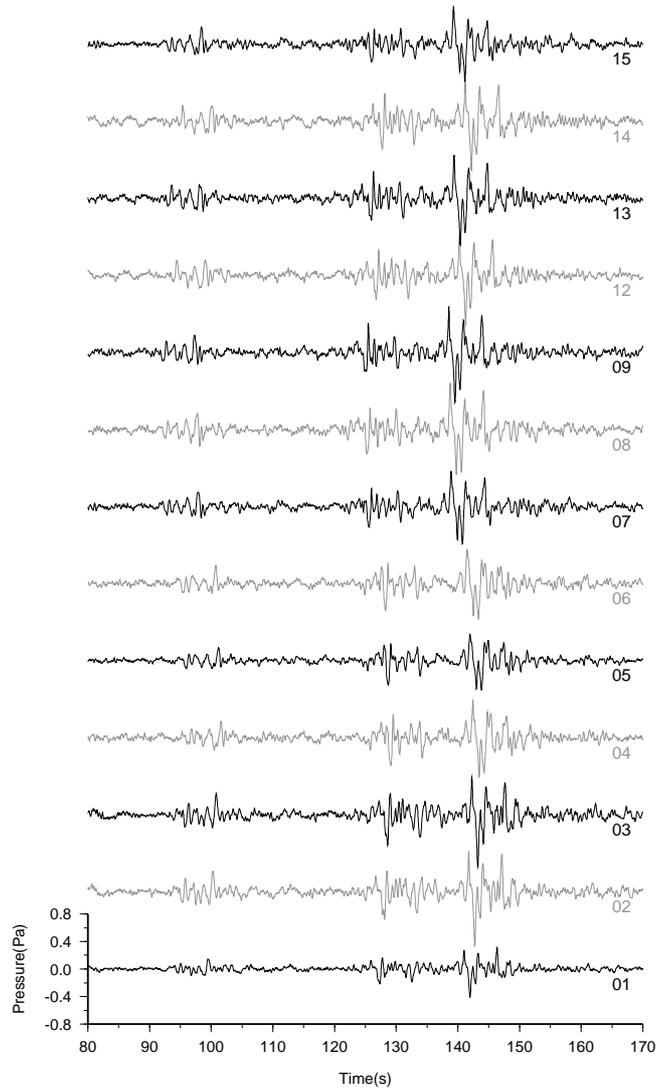
Figure 2.15: *Band-pass filtered traces with a second order Butterworth filter with corner frequencies of 0.1 and 5 Hz. The traveltime differences over DIA are visible.*
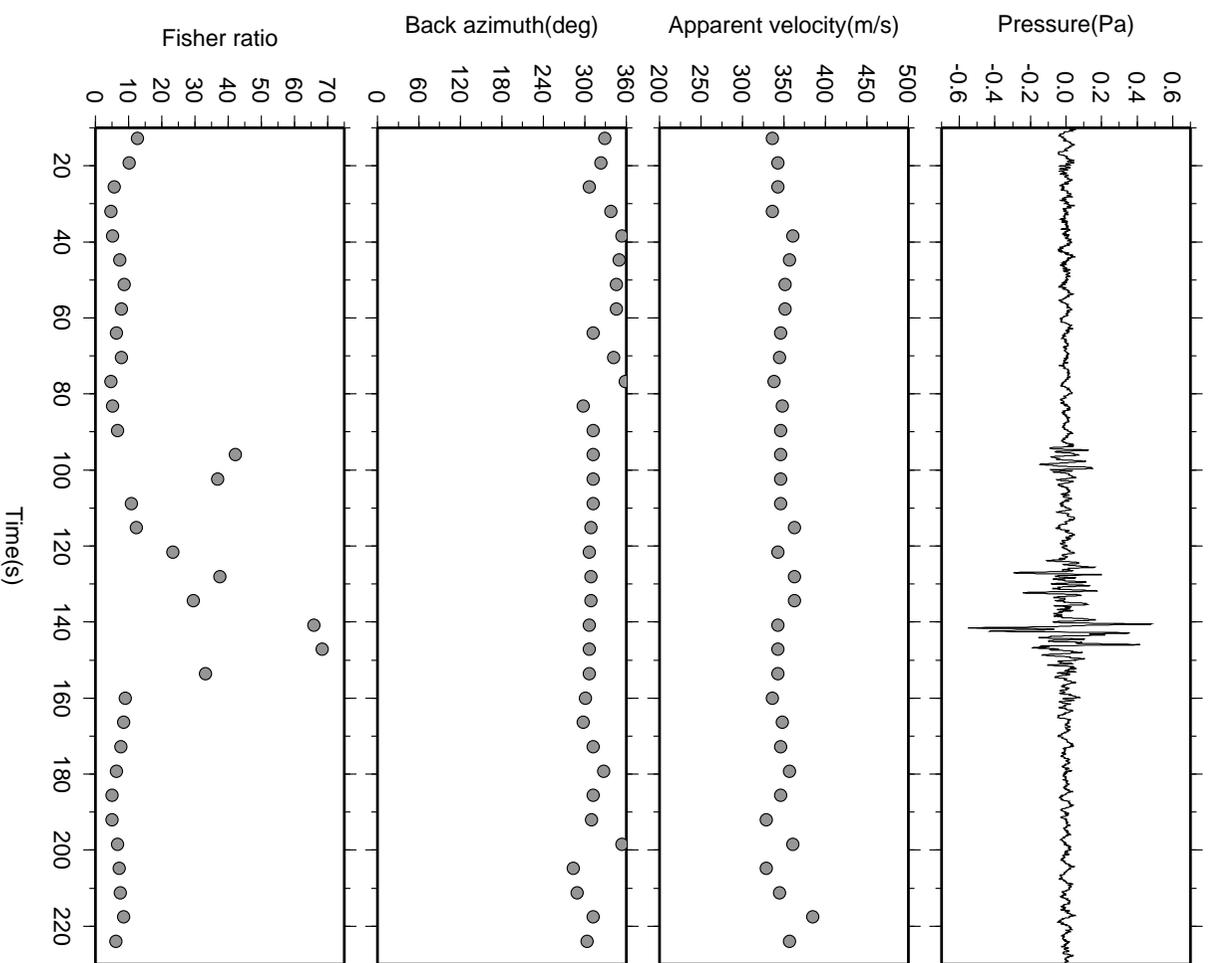
Figure 2.16: *Results of a time domain F-ratio analysis (see equation 2.3.45). From bottom to top, the frames show the F-ratio, back azimuth, apparent sound speed and the best beam, all as function of time.*
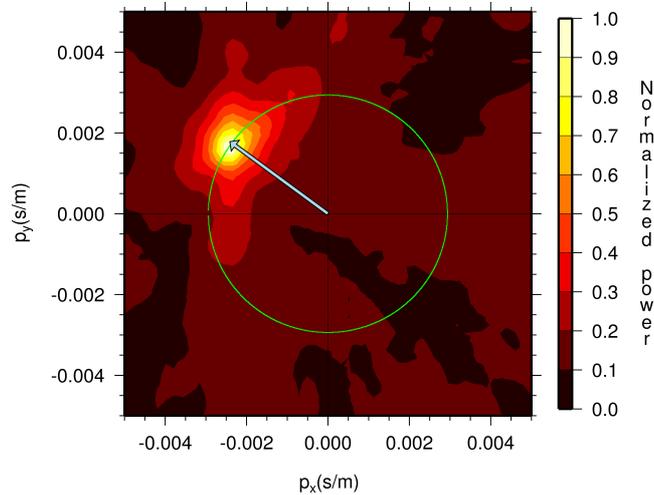
Figure 2.17: *Broad-band frequency slowness analysis for the energy around 140 s in the frequency range of 0.1 to 5 Hz (see equation 2.3.49). The light blue slowness vector points to the maximum value of the power. A time segment of 1024 samples (25.6 s) is evaluated which gives a power value each 0.039 Hz. These are averaged over the range of 0.1 to 5 Hz. The green circle represents a c_{app} of 340 m/s.*

■ 2.3.3 Processing example

In this section, a processing example of infrasonic array data is presented to illustrate beamforming, signal detection and parameter estimation. Figure 2.14 shows 230 seconds of infrasound recordings made by the microbarometers of DIA. The recordings of the 16 element array started on 2007, September 04 at 20h03m18.475s UTC. During that time, 13 of the 16 microbarometers were operational. Long periodic signals are visible throughout the recordings. These signals have periods of at least 100 seconds and amplitudes of several pascals.

A more high frequency signal is superimposed on these background fluctuations. In Figure 2.15, a second order Butterworth band-pass filter has been applied to the same recordings, with corner frequencies of 0.1 and 5 Hz. The time axis has been adjusted to show clearly the signal coherency and traveltime differences over the array. Packages of coherent energy can be identified on all recordings. The arrivals between 140 and 150 s have the largest amplitudes and show a high coherency. From Figure 2.15, it should be noted that the energy appears first on microbarometer 08 and last on number 04. Therefore, a rough estimate is obtained of a source located to the northwest of DIA (see Figure 2.10). These signals have most likely been caused by a military jet flying supersonically above the North Sea approximately 300 km from DIA.
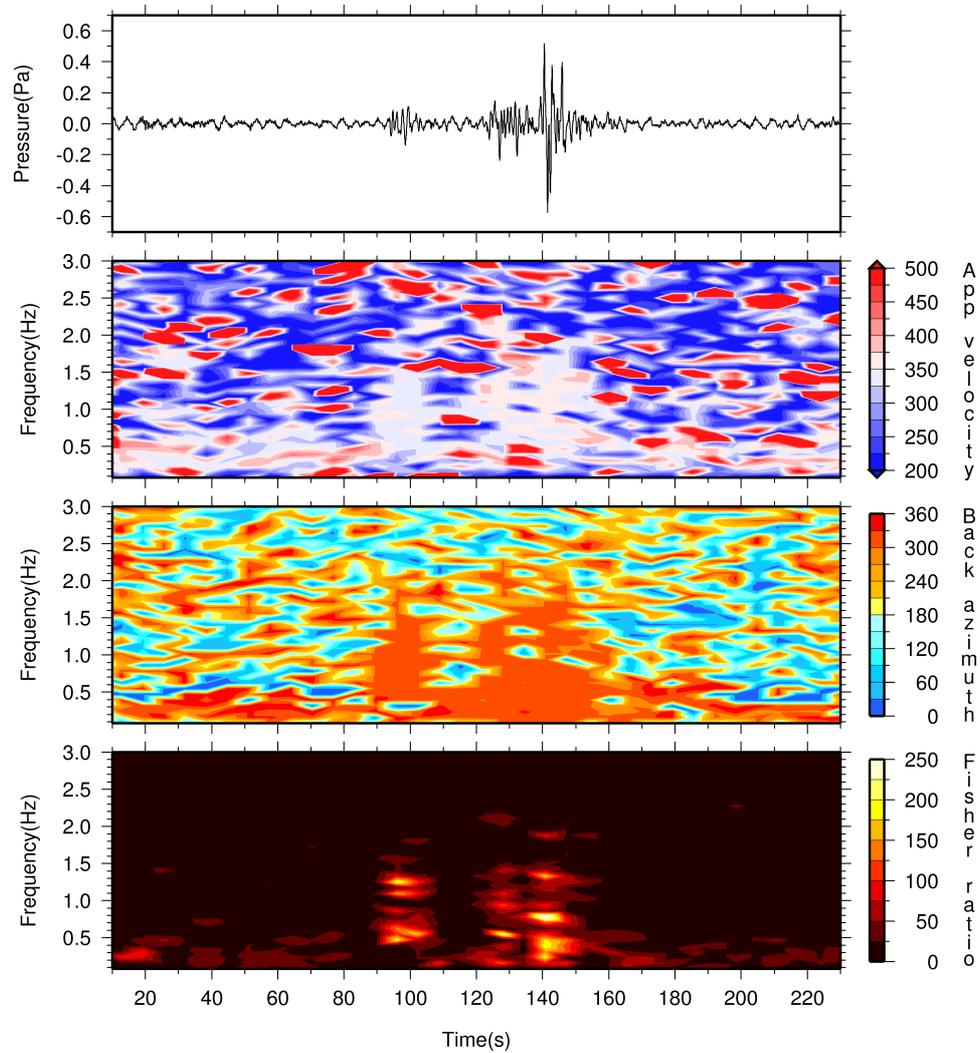
Figure 2.18: *Processing results from a frequency domain Fisher analysis (see equation 2.3.52). From bottom to top, the frames shows the color-coded F-ratio, back azimuth, apparent sound speed and the best beam, all as function of time and frequency.*
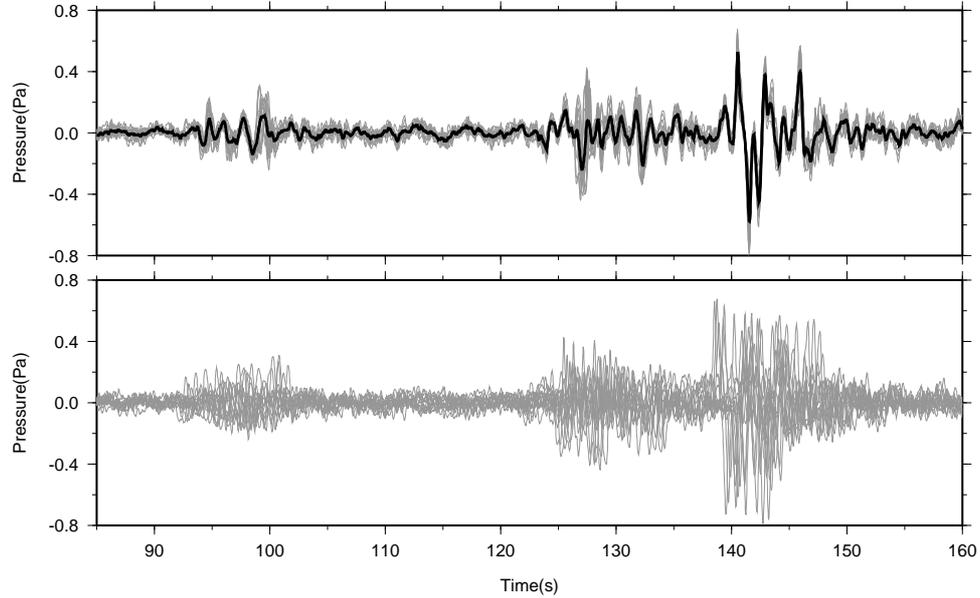
Figure 2.19: *The lower frame shows the unaligned recordings in DIA. The aligned traces and best beam (in black) are given in the top frame. All traces are time shifted according to the slowness values at maximum F-ratio as found around 140 s.*

The recordings are processed by making use of the F-ratio as described by equation 2.3.45. In Figure 2.16, the results of detection and parameter estimation are given. Signal detection is achieved by splitting the recordings in 50% overlapping bins of 512 samples, which is 12.8 seconds, with a sample rate of 40 Hz. Beamforming is performed on a slowness grid of 50×50 points. Thus, 2500 beams are evaluated for each bin; the maximum F-ratio within a bin is plotted. Several high values of the F-ratio trigger a detection. The maximum F-ratio of 70 is found around 140 s, which corresponds to a signal-to-noise power ratio of 5.3 (see lower frame) by making use of equation 2.3.46. This maximum F-ratio corresponds to one of the 2500 beams. This specific beam is the one which best explains the measured traveltime differences over DIA. Parameter estimation can be realized on the basis of the derived traveltime differences. The resolved back azimuth ϕ and apparent sound velocity c_{app} are 306.5 deg and 342.6 m/s, respectively, as can be determined from the middle two frames of Figure 2.16. These values correspond to a p_x and p_y of -2.347×10^{-3} and 1.735×10^{-3} s/m, respectively. The best beam is displayed in the top frame and constructed with the slowness values at maximum F-ratio.

To illustrate a f/k analysis, equation 2.3.49 is evaluated. Instead of $\vec{k}$, slowness $\vec{p} = \frac{\vec{k}}{\omega}$ is substituted and the output is normalized. Figure 2.17 shows the results

of the analysis for the most coherent energy around 140 s. A time segment of 25.6 s is used resulting in a power value each 0.039 Hz. Individual frequencies are than summed between 0.1 and 5 Hz and finally averaged. The light blue slowness vector points to maximum power. The length of this vector represents an apparent sound speed c_{app} of 340.1 m/s. The angle of the vector with respect to the North (clockwise) is the back azimuth ϕ and has a value of 306.5 deg. These values follow from a p_x and p_y of -2.374×10^{-3} and 1.735×10^{-3} s/m.

The F-ratio is also described in the frequency domain (see equation 2.3.52). The results of such an analysis are given in Figure 2.18. Again, the data are split in 50% overlapping bins of 512 samples, which is 12.8 seconds with a sample rate of 40 Hz. The F-ratio as function of time and frequency is shown in the lower frame. The middle two frames give the back azimuth ϕ in degrees and apparent sound speed c_{app} in m/s, respectively. The maximum F-ratio is found around 140 s; the corresponding back azimuth is 304.8 deg and the apparent sound speed is 349.8 m/s around 1.3 Hz. The best beam is displayed in the top frame and constructed with the slowness at maximum Fisher ratio.

There is a small difference in the retrieved parameters in the time and frequency domain analysis. In frequency domain processing, each frequency is treated individually which results in a specific Fisher value and set of parameters. On the other hand, time domain analysis is intrinsically broad band from which an average value over all frequencies is derived.

Figure 2.19 shows the individual recordings and the best beam to illustrate the effectiveness of the presented processing methods. In the lower frame, the band-pass filtered recordings are plotted. The traveltime differences over DIA are still present in the recordings. The top frame shows the time aligned recordings and the best beam in black. The calculations are done for the maximum F-ratio found in the frequency domain analysis, around 140 s. Clearly, the recordings are very well aligned around 140 s. Other coherent energy around 95 s and 130 s is less well aligned because its parameters, or slowness, slightly differ from the values at the maximum F-ratio. Although, the energy belongs to the same source, the trajectories through the atmosphere might differ.

3

Meteors as natural impulsive sources of infrasound

3.1 Listening to sounds from an exploding meteor and oceanic waves

■ 3.1.1 Abstract

Low frequency sound (infrasound) measurements have been selected within the Comprehensive Nuclear-Test-Ban Treaty (CTBT) as a technique to detect and identify possible nuclear explosions. The Seismology Division of the Royal Netherlands Meteorological Institute (KNMI) operates since 1999 an experimental infrasound array of 16 microbarometers. In this chapter, we present the detection and identification of an exploding meteor above northern Germany on 1999, November 8 with data from the Deelen Infrasound Array (DIA). At the same time, sound was radiated from the Atlantic Ocean, South of Iceland, due to the atmospheric coupling of interacting ocean waves, called microbaroms. Occurring with only 0.04 Hz difference in dominant frequency, DIA proved to be able to discriminate between the physically different sources of infrasound, through its unique lay-out and instrumentation. The explosive power of the meteor being 1.5 kT TNT is in the range of nuclear explosions and therefore relevant to the CTBT.
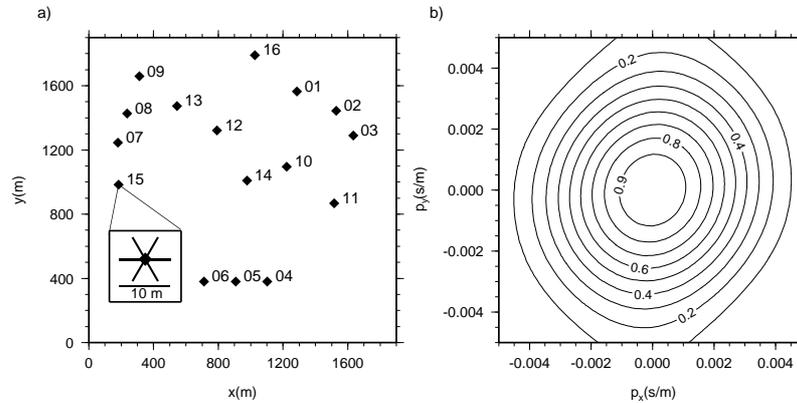
Figure 3.1: *The Deelen Infrasound Array (DIA). (a) DIA lay-out, showing 16 microbarometers in a 1.5 km aperture configuration. To each microbarometer six porous hoses are connected for noise reduction (see inlay). (b) Array response for a vertical incident plane wave of 0.1 Hz. The circular shape of the response reflects the omni-directional properties of the array.*

■ 3.1.2 Introduction

For Comprehensive Nuclear-Test-Ban Treaty (CTBT) purposes, a world-wide network of 60 infrasound arrays is currently being constructed [*PrepCom*, 1997]. Most arrays consist of four instruments in a lay-out with an aperture of 1–3 km. The Deelen Infrasound Array (DIA), not part of the stations for CTBT purposes, is configured with 16 microbarometers in a 1.5 km lay-out (Figure 3.1a), installed on an Air Force base near the village of Deelen in the Netherlands. The microbarometers, developed by the KNMI, consist of differential pressure sensors with a flat frequency response between 0.002 and at least 20 Hz. This frequency range is relevant for detecting sonic booms and CTBT related events. To each instrument six porous hoses of five meters length are connected in a star-like configuration (Figure 3.1a, inlay). This analog filter will reduce wind noise by integrating over the covered area, without affecting the signal. The array response to a vertical incident plane wave of 0.1 Hz is shown in Figure 3.1b. The absence of side-lobes within the infrasonic domain and the omni-directional properties of the array with respect to resolution and sensitivity guarantee ideal measurement conditions. The detection and identification of the 1999, November 8 meteor explosion above northern Germany provides an excellent illustration of the capacity of DIA.
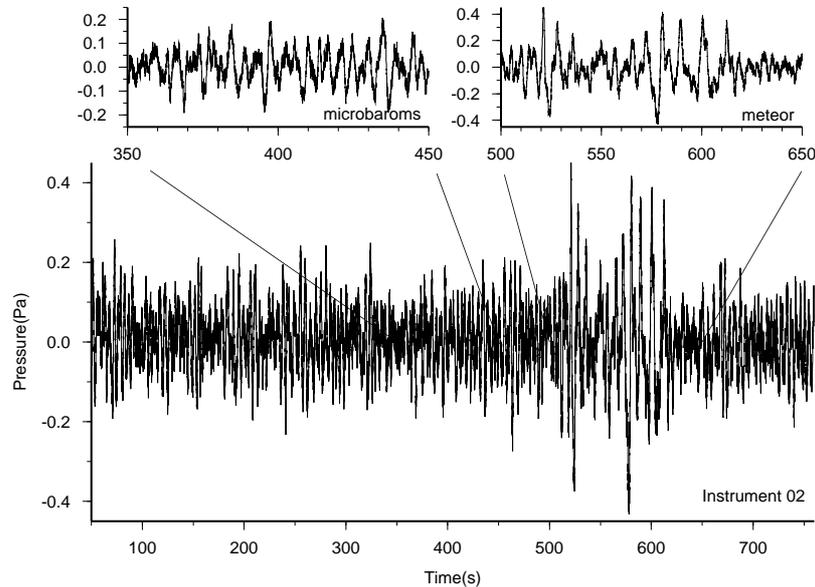
Figure 3.2: *Recording of instrument 02. Time is since 04h09m24.4s UTC on 1999, November 8. The data are high-pass filtered at a corner frequency of 0.05 Hz. Between 500 and 650 seconds infrasound from the meteor is recorded. The induced pressure variation equals 0.79 Pa on instrument 02. Microbaroms are present throughout the recording.*

■ 3.1.3 Infrasonic Data

A meteor generates infrasound upon entering the earth's atmosphere at altitudes lower than 50 km [*Donn and Balachandran*, 1974];[*McIntosh et al.*, 1976]. Shock waves are produced when the meteor explodes at an altitude of 20 km [*ReVelle*, 1975]. In Figure 3.2 we show a high-pass (corner frequency of 0.05 Hz) filtered signal from array element no 2 as an example of what we identified as the meteor explosion. The event was also detected on photos from all-sky cameras made in the Czech Republic and observed by humans in the Netherlands and Germany. On the basis of this, we estimate the meteor's explosion to have taken place above northern Germany. In Figure 3.2, the signal can be seen as a small increase in amplitude and slightly lower frequency content. The induced pressure variation by the meteor is 0.79 Pa on this specific instrument. A secondary arrival after 55 seconds is also visible in the signal. Microbaroms, produced by the atmospheric coupling of interacting ocean waves in the ocean, can be found through the whole record as packages of coherent energy [*Posmentier*, 1967] with a lower amplitude than the meteor's energy. This record is representative for all 16 array elements.

■ 3.1.4 Detection of infrasonic sources in the frequency domain

According to *Smart and Flinn* [1971], the frequency-wavenumber spectra can be calculated in a single summation. With the relation $\vec{k} = \omega\vec{p}$ between the slowness vector $\vec{p}$ and the wavenumber $\vec{k}$ for frequency ω, the frequency-wavenumber spectrum is converted to frequency-slowness power spectrum:

$$P(\omega, \vec{p}) = \left| \sum_{n=1}^{N} G(\omega, \vec{r}_n) \cdot e^{-i\omega\vec{p}\cdot\vec{r}_n} \right|^2 \tag{3.1.1}$$

with: $G(\omega, \vec{r}_n)$ being the Fourier transforms of recordings at N number of instruments located by $\vec{r}_n$ position vectors. $P(\omega, \vec{p})$ can be interpreted as a set of beams sampling the atmosphere above the array [*Haak*, 1996]. The beams are controlled by the slowness vector $\vec{p}$. Coherent energy can be detected, as energy originating from a specific direction in the atmosphere. In this case, the power of the spectrum will increase. The associated best beam has characteristic values for apparent sound speed c_{app} and back azimuth ϕ, following:

$$|\vec{p}| = \sqrt{p_x^2 + p_y^2} = \sqrt{\left(\frac{\cos\phi}{c_{app}}\right)^2 + \left(\frac{\sin\phi}{c_{app}}\right)^2} = \frac{1}{c_{app}} \tag{3.1.2}$$

The Fisher ratio F is defined as [*Smart and Flinn*, 1971]:

$$F(\omega, \vec{p}) = \frac{P_S(\omega, \vec{p})}{P_T(\omega) - P_S(\omega, \vec{p})} \cdot (N - 1) \tag{3.1.3}$$

where

$$P_S(\omega, \vec{p}) = \left| \frac{1}{N} \sum_{n=1}^{N} G(\omega, \vec{r}_n) \cdot e^{-i\omega\vec{p}\cdot\vec{r}_n} \right|^2 \tag{3.1.4}$$

$$P_T(\omega) = \frac{1}{N} \sum_{n=1}^{N} |G(\omega, \vec{r}_n)|^2 \tag{3.1.5}$$

$P_S(\omega, \vec{p})$ represents the spectral amount of energy belonging to the signal and can be obtained from the power spectrum $P(\omega, \vec{p})$. The total amount of spectral power, including both noise and signal, is described by $P_T(\omega)$. Thus, without the $(N-1)$ weighting factor F is a measure of the signal-to-noise power ratio. A coherent infrasonic wave traveling over the array will increase F. Incoherent or small scale coherent wind noise will result in a low value for F, typically between one and five. The top frame in Figure 3.3 shows the best beam for the meteor, Fisher ratios are plotted in the middle frame, with back azimuths of the incoming energy in the lower frame. The best beam has an amplitude summed over the sixteen traces. Therefore, the average amplitude of the first arrival from the meteor is the best approximation for the generated pressure variation. The maximum amplitude has a value of 0.75
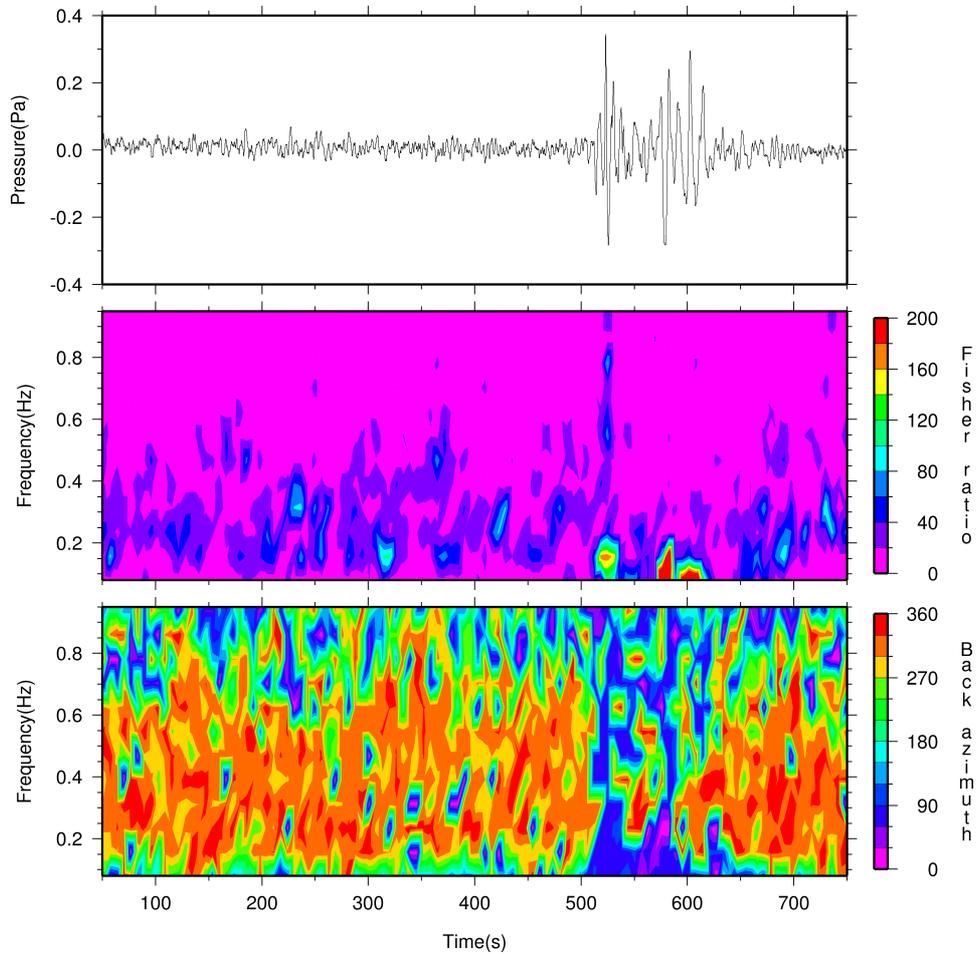
Figure 3.3: *The best beam for the meteor (top frame), Fisher ratios (middle frame) and back azimuth solutions (lower frame). Microbaroms are identified at distinct frequencies while the meteor is coherent over a wide range of frequencies. Maximum coherency, or the highest Fisher value, for the meteor is found at 0.15 Hz, while the secondary arrival is more low frequent. The meteor's energy is coming in from the northeast with respect to DIA. Microbarom energy originates from a more northwestern direction.*
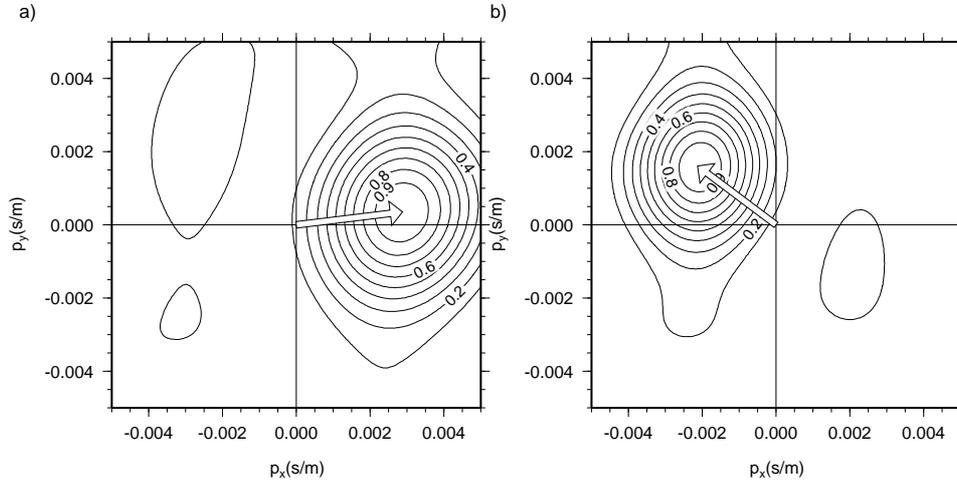
Figure 3.4: *Normalized frequency-slowness (fp) power plots. (a) The 0.15 Hz component of the meteor. The meteor is characterized by an apparent sound speed c_{app} of 353 m/s with a back azimuth ϕ of 82 degrees, in the NE quadrant. Some microbarom energy is present in the NW quadrant. (b) The 0.19 Hz component of the microbaroms. Resolved are c_{app} of 390 m/s and ϕ of 309 degrees.*

Pa. The Fisher ratio, which is a measure of the signal coherency, increases over a large range of frequencies at the meteor arrival time, after 510 seconds. The secondary arrival after 565 seconds has a lower frequency contents of 0.1 Hz. Its delay of 55 seconds and damped higher frequency part indicate an atmospheric refraction. On the other hand, microbarom coherency is bounded to smaller frequency ranges, showing up through the whole record. The coherency of the meteor signal is also reflected when evaluating the azimuth as plotted in the lower frame. The meteor energy is coming from the northeast, while yellow to red colors indicate a northwestern origin for the microbarom energy.

■ 3.1.5 Identification of infrasonic sources

From Figure 3.3 it follows that the first arrival of the meteor has maximum Fisher values, i.e. coherency, around 0.15 Hz. The power of the fp spectrum $P(\omega, \vec{p})$ is calculated for a frequency of 0.15 Hz and a range of $\vec{p}$ values in the infrasonic domain. Figure 3.4a shows the result for this calculation. The vector with length c_{app} and back azimuth ϕ points to the maximum power associated with the meteor explosion. The detected energy is characterized by a velocity c_{app} of 353 m/s coming in with an angle ϕ of 81.9 degrees (with respect to the North). Some microbaroms energy is present in the northwestern quadrant.
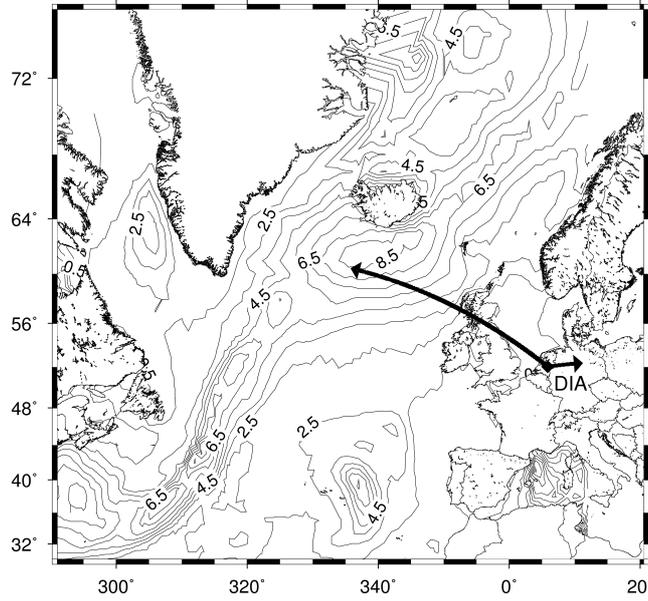
Figure 3.5: *Contoured are the pressure amplitudes of $a_w^2 \omega^2$ (in $m^2 s^{-2}$) of the generated pressure by ocean waves. The maximum South of Iceland has a wave period of 9.8 s, generating pressure variations with a frequency of 0.2 Hz. The vectors denote the resolved infrasonic sources by DIA. Infrasound from the meteor originates from a northeastern direction while the microbaroms are resolved by DIA at 0.19 Hz to the northwest.*

A large Fisher value for the microbaroms is found around 310 seconds in Figure 3.3. The coherent energy is centralized around 0.19 Hz. Locating this energy is done in Figure 3.4b. The microbarom energy is characterized by a c_{app} of 390 m/s and ϕ of 309 degrees. Comparing the apparent sound velocities of the different events, implies a steeper angle of incidence for the microbarom energy.

Standing wave patterns on the sea surface, generated by storm centers, produce infrasonic waves in the atmosphere [*Wilson*, 1981]. Based on theory for microseism described by *Longuet-Higgins* [1950], *Posmentier* [1967] concluded that the compressibility of air has no significant effect on the pressure fluctuations. Therefore, microseism and microbaroms are generated by standing ocean waves, with an oscillatory pressure of:

$$P = -2\rho_0 a_w^2 \omega^2 cos2\omega t \qquad (3.1.6)$$

where, ρ_0 is the density of air for microbaroms and of water for microseisms, a_w is the amplitude of the standing wave with frequency ω at time t. In Figure 3.5 the pressure amplitudes of $a_w^2 \omega^2$ are plotted, calculated from oceanic wave data. Furthermore, the

resolved azimuthal angles of DIA are denoted by the vectors. The $a_w^2 \omega^2$ data were obtained at 06h00m UTC on 1999, November 8. The wave period of the maximum is 9.8 seconds. By making use of equation 3.1.6, a pressure variation of 0.2 Hz is induced. This correlates with the 0.19 Hz found in the frequency domain analysis. A possible explanation for the difference between the observed azimuth and location of the maximum can be found in the source of the data. P describes the generated pressure due to standing ocean waves, while the contours in Figure 3.5 result from wave patterns as such. Wave interference, generating standing waves, occurs close to an atmospheric depression but does not necessarily coincide with $a_w^2 \omega^2$ maximum derived from non standing ocean waves. Furthermore, the atmospheric depression and associated meteorological temperature and wind profiles nearby will heavily influence the sound propagation and possibly deflect the acoustic waves [*Ørbæk and Naustvik*, 1995].

Infrasound from the meteor originates from the northeast of DIA. The location above northern Germany is confirmed by human observations and all-sky camera photos, giving an origin time of 03h54m10s UTC. The origin time and differential traveltime of 55 s between the first and second arrival are used to model the explosion altitude and range [*Garcés et al.*, 1998]. By raytracing through an atmospheric model (based on [*Hedin et al.*, 1996]), we fitted the explosion data to an estimated altitude of 15 km occurring at a distance of 320 km. The energy of the exploding meteor can be calculated by using the period T at maximum amplitude, A_{max}, as described by *ReVelle* [1997]. This semi-empirical approach connects the yield, Y, in kT TNT and the observed period, $T_{A_{max}}$:

$$\log Y = 3.34 \cdot \log T_{A_{max}} - 2.58 \rightarrow Y \leq 100 \, \text{kT TNT} \qquad (3.1.7)$$

Formula 3.1.7 is obtained on the basis of data from low altitude nuclear explosions. Following personal communication with Dr. R.O. ReVelle [2000] it was concluded that the condition of being at large range from the source is fulfilled. Thus, the total amount of energy released by the exploding meteor, taken a period of 6.7 s, equals 1.5 kT TNT.

■ 3.1.6 Conclusions

Infrasonic energy from a meteor and microbaroms, differing in frequency only 0.04 Hz, are resolved by DIA. Frequency-slowness analysis of the data, combined with Fisher statistics, enable a clear detection and identification of the meteor's explosion in the northeast and the microbaroms infrasonic energy northwest of DIA. The energy release of the exploding meteor of 1.5 kT TNT is in the range of nuclear explosions and therefore of CTBT interest.

3.2 Tracing a meteoric trajectory with infrasound

■ 3.2.1 Abstract

A bright bolide appeared over the Netherlands on the evening of 2003, February 19. Infrasound generated by this bolide was detected at two nearby infrasound arrays as two distinct events. The origins of the infrasonic signals were located in the stratosphere at altitudes of 30 and 57 km. The results were obtained independently of visual observations of the bolide but confirm the reported time of occurrence. The ability to distinguish between a moving and static source is crucial for the application of infrasound as a monitoring technique. This study also illustrates the dependence of the infrasound technique on signal coherency, inter-array distance and atmospheric knowledge.

■ 3.2.2 Introduction

Infrasound is inaudible sound with frequencies ranging between 0.002 and 20 Hz, i.e. the human hearing threshold. The infrasonic frequency band recently gained renewed attention because of the Comprehensive Nuclear-Test-Ban Treaty (CTBT). World-wide, 60 infrasound arrays are being installed to monitor the atmosphere as a verification technique for the CTBT [*PrepCom*, 1997]. In general, bodies traveling in the earth's atmosphere at super-sonic speeds generate infrasound. Meteors are one of the few natural impulsive sources of infrasound generating energies in kT TNT equivalent range [*ReVelle*, 1997]. Therefore, the study of the infrasound generated by meteors is essential to the CTBT. Detecting and tracing the trajectory of a bolide with infrasound also contributes to estimating the flux of near-earth objects and their energy [*Brown et al.*, 2002b]. Furthermore, knowing the path of the meteor and the location of a meteorite fall gives insight into streams of meteoritic objects [*Spurný et al.*, 2003]. In this paper, we show the ability to trace a meteor trajectory in the stratosphere with infrasound data from two arrays.

■ 3.2.3 Infrasound measurements

Data acquisition

Infrasound can be measured by tuning a traditional microphone for low frequencies or a barometer to high frequencies. The latter approach was chosen, for use by

the authors' institute, to guarantee durable outdoor operation of the instrument. The KNMI microbarometer was developed with the capability to measure infrasound between 0.002 and 20 Hz [*Evers and Haak*, 2001b]. Most natural infrasound and CTBT related events occur within this frequency band. The microbarometer is a differential pressure sensor based on a Validyne pressure transducer. Arrays of microbarometers are used to localize the infrasonic source and reduce noise which is mainly caused by wind. Analog noise reduction is achieved at each instrument by sampling the atmosphere over an area rather than one point. Due to its small coherency length, wind is filtered out while the infrasonic signal of interest remains unaffected [*Hedlin et al.*, 2003]. Porous hose can effectively reduce wind noise in a spatial filter by, for example, applying the hoses in a star-like configuration. Currently, three infrasound arrays are operational in the Netherlands: the Deelen (DIA), De Bilt (DBN) and Witteveen (WIT) Infrasound Arrays. All sensors of the arrays are equipped with porous hose noise reducers. Figure 3.6 illustrates the infrasound measurement capabilities of the KNMI. Shown are the location and configuration of the infrasound arrays.

Recordings from the meteor

An impressive and bright meteor occurred over the Netherlands on 2003, February 19. The bolide was reported by citizens all over the Netherlands. The following source characteristics were derived: time 18h13m05s UTC, duration 1 up to 5 seconds, brightness -5 to -8 (for comparison, the full moon has a defined visual brightness of -12.6 and the sun of -26.7), no sounds, some fragmentation and an approximate path from the South to the North. These characteristics are based on the author's observation (*LE*) and a summary of the reports. Two infrasound arrays, DIA and DBN, recorded infrasound from the meteor. All elements from these two arrays were used in the analysis. WIT was not operational around the time of the event. Representative signals are shown in Figure 3.7 of a selection of recordings by DIA and DBN. Two distinct arrivals of meteoric infrasound appear in both DIA and DBN. The typical blast waveform can be recognized in the second arrival; the first arrival appears to have an U-wave character or might originate from a summation of blast waveforms. The event's signal consists of high frequencies compared to other bolide recordings, implying a small object [*ReVelle*, 1976]. The arrivals have an average frequency content of 3.5 Hz.
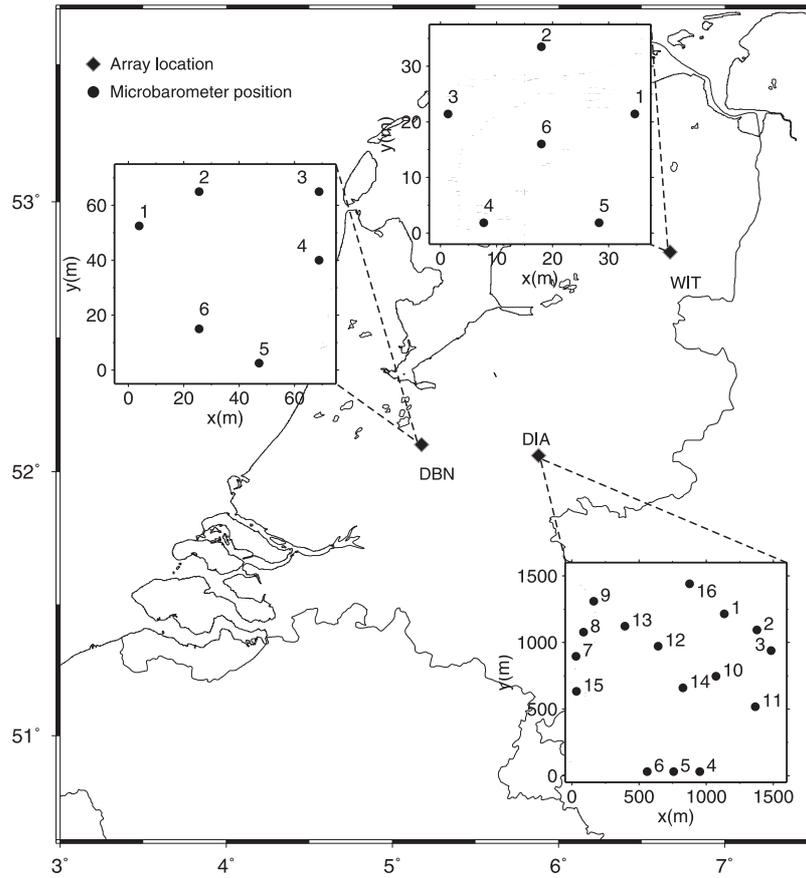
Figure 3.6: *Map showing the Netherlands with the locations of the three infrasound arrays. The array configurations are displayed in separate inlays. WIT was not operational during the event.*
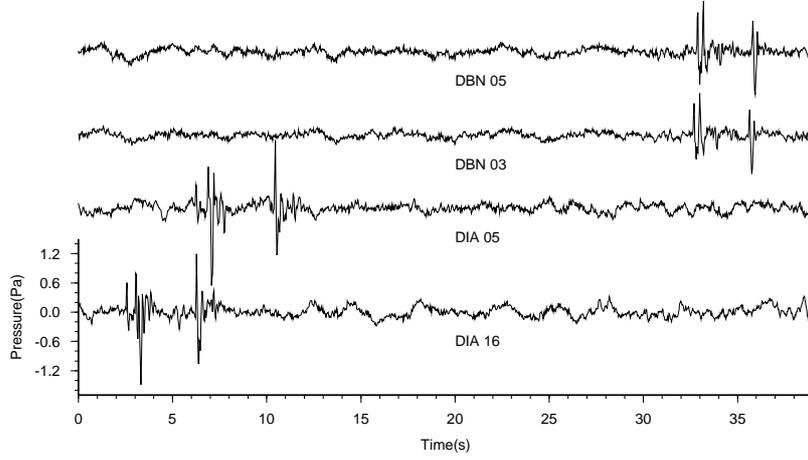
Figure 3.7: *Two representative recordings of DBN, elements 03 and 05, and DIA, elements 05 and 16. The data are band-pass filtered with a second order Butterworth filter having corner frequencies of 0.5 and 15 Hz. The time axis starts on 2003, February 19 at 18h17m57.28s UTC.*

■ 3.2.4 Infrasound data analysis

Time domain Fisher processing

Processing of array data is based on signal coherency. A statistical measure is given by the Fisher ratio, defined in *Melton and Bailey* [1957] as:

$$F = \frac{T(N-1)}{N(T-1)} \frac{\sum_{t=1}^{T}(\sum_{n=1}^{N} x_{nt})^2 - \frac{1}{T}(\sum_{t=1}^{T}\sum_{n=1}^{N} x_{nt})^2}{\sum_{t=1}^{T}\sum_{n=1}^{N} x_{nt}^2 - \frac{1}{N}\sum_{t=1}^{T}(\sum_{n=1}^{N} x_{nt})^2} \qquad (3.2.8)$$

where the variances of N independent observations of quantity x are evaluated over a timespan T and multiplied by the degrees of freedom. F is evaluated by beamforming in the slowness domain $\vec{p}$. At maximum F, event characteristics in terms of apparent sound speed c_{app} and back azimuth ϕ are resolved through:

$$|\vec{p}| = \sqrt{p_x^2 + p_y^2} = \sqrt{\left(\frac{\cos\phi}{c_{app}}\right)^2 + \left(\frac{\sin\phi}{c_{app}}\right)^2} = \frac{1}{c_{app}} \qquad (3.2.9)$$

The signal-to-noise power ratio (snr) can be calculated from the maximum F following: $F = N \cdot snr + 1$, assuming a plane wave and uncorrelated noise.
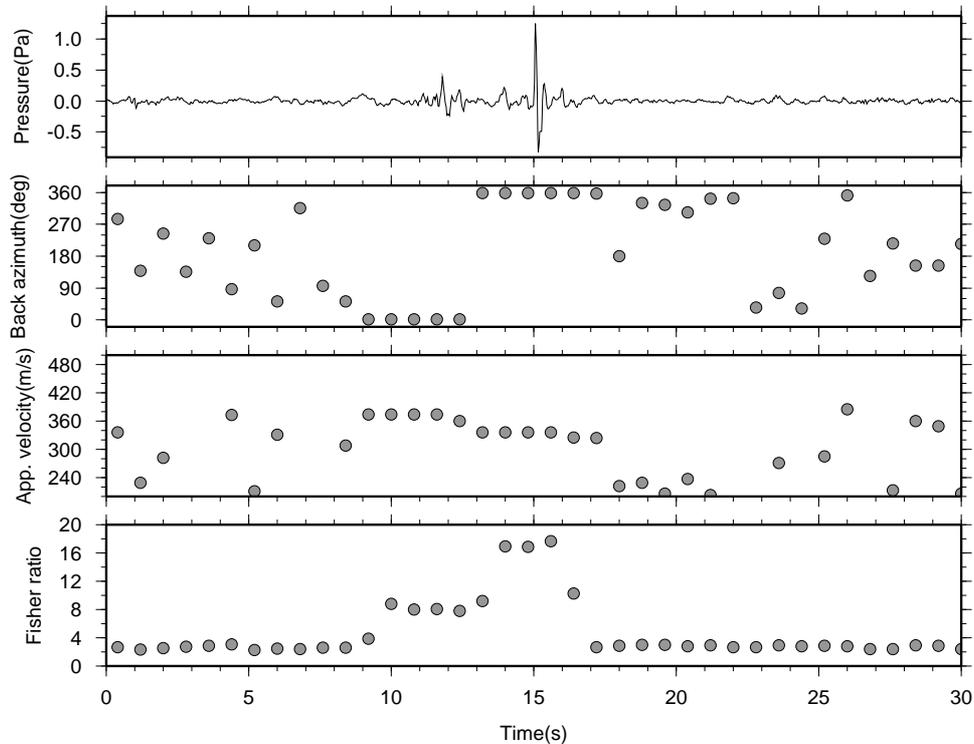
Figure 3.8: *Results of the time domain Fisher analysis for DIA. Data are processed with bins of 3.2 seconds (128 samples) with 25% overlap. The Fisher ratio is evaluated on 100×100 slowness grid. The maximum Fisher ratio is plotted in the lower frame for each bin. Resolved apparent sound speed and back azimuth are shown in the middle two frames. The top frame shows the best beam for the highest Fisher ratio value. A snr of 1.0 is calculated at maximum Fisher ratio.*

Processing results for DIA and DBN

The two distinct arrivals in the DIA data come from different directions, see Figure 3.8. The first arrival is incident at 1.0 deg back azimuth and 360 m/s, while the second at 359.0 deg and 336 m/s. The accuracy is 0.1 deg and 1 m/s. The top frame shows the best beam calculated for the second arrival. The first arrival is not well aligned in time for the corresponding slowness value and does not form a good beam.

The two arrivals in the DBN data, see Figure 3.9, have the following characteristics, 32 deg and 341 m/s and 36 deg and 374 m/s, respectively, with an accuracy of 1 deg and 5 m/s. These accuracies can be derived by evaluating the distributions of the
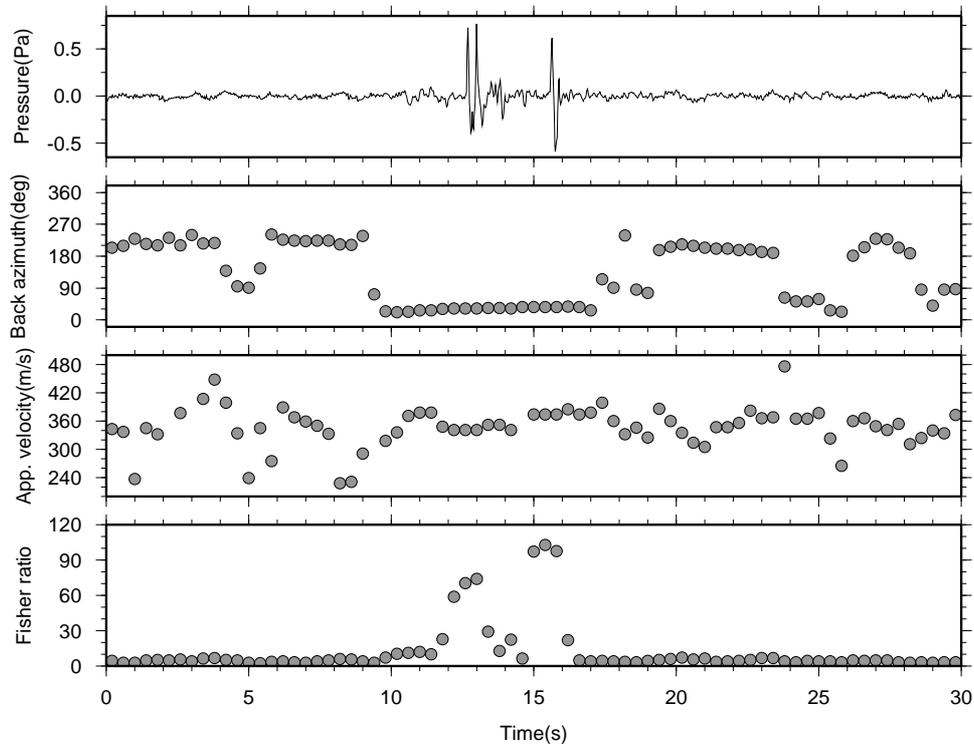
Figure 3.9: *A similar representation as in Figure 3.8 of the results for DBN. The bin size is reduced to 1.6 seconds (64 samples) with a 25% overlap because of the smaller aperture. A snr of 16.8 is derived at maximum Fisher ratio.*

slowness estimates. The best beam for DBN is calculated for the second waveform, but also amplifies the first arrival because of the much smaller travel time differences over the array than at DIA. Although the waveforms from DBN and DIA look very similar, DBN data have a *snr* of 16.8 and in DIA an apparent value of 1.0 is derived. Both waveforms are processed simultaneously in DIA which lowers the F ratio. By artificially splitting both waveforms a more realistic *snr* of 2 is calculated. The larger aperture of DIA causes loss of spatial coherency of these high frequency arrivals.

The locations of the waveforms' sources are obtained through cross bearing and are shown in Figure 3.10. The phase that arrived first in the infrasound arrays had its origin farther away than the phase arriving secondly. A phase is a coherent arrival that traveled over the array which can be pinpointed on the basis of its impulsive character.
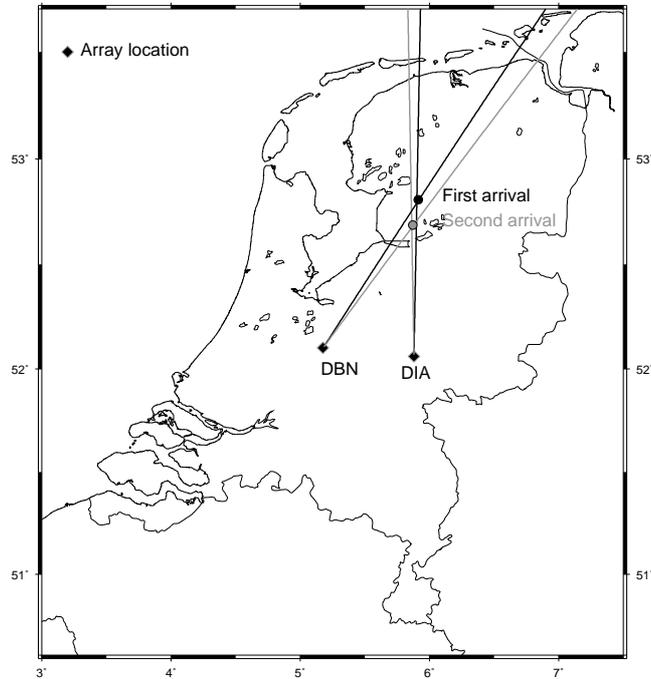
Figure 3.10: *Map showing the locations obtained through cross bearing. The black bearings are for the first arrival, gray bearings for the second arrival.*

■ 3.2.5 Tracing the bolide's energy

Atmospheric profiles

Infrasound wave propagation is dependent on the wind and temperature structure of the atmosphere. The effective sound speed is described by *Garcés et al.* [1998]:

$$c_{eff} = \sqrt{\gamma_g R_c T_a} + \hat{n}_{xy} \cdot \vec{u} \qquad (3.2.10)$$

where the multiplication of the ratio of specific heats with the gas constant for air is $\gamma_g R_c$=402.8 m^{2}s^{-2}K^{-1}, the absolute temperature is given by T_a, and $\hat{n}_{xy} \cdot \vec{u}$ projects the wind $\vec{u}$ in the direction from source to observer $\hat{n}_{xy}$.

Wind and temperature data of the lower atmosphere are commonly available because of meteorological interest. Above tropospheric altitudes data become sparse. Figure 3.11 shows the available atmospheric profiles. The European Centre for Medium-Range Weather Forecasts (ECMWF) models, in red, follow the KNMI profiles for the lower atmosphere. The Horizontal Wind Model/Mass Spectrometer and Incoherent Scatter Radar Extended Model (HWM/MSISE) [*Hedin et al.*, 1996], in brown, and
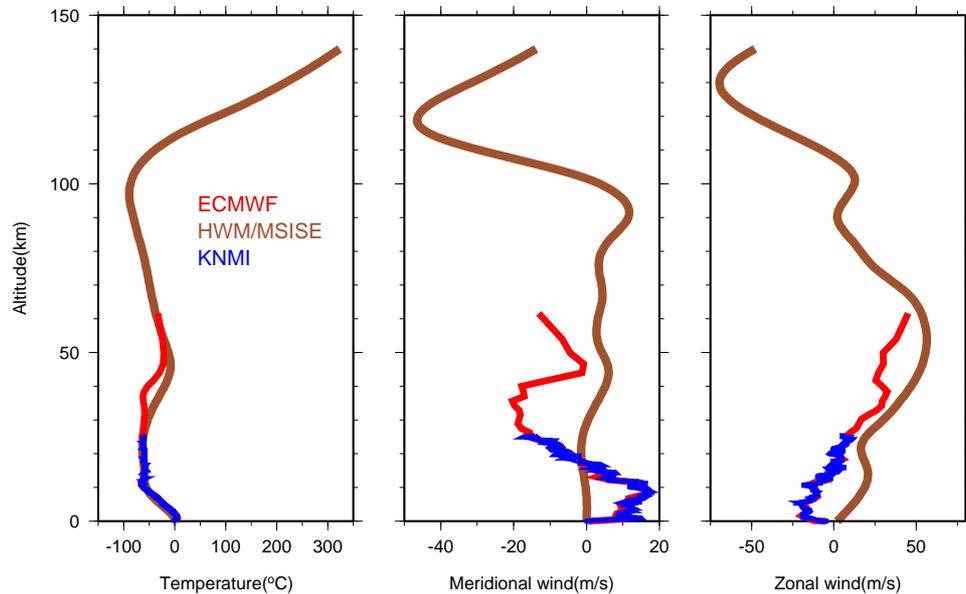
Figure 3.11: *The available atmospheric data for 52.5° N, 5.5° E on 2003, February 19 at 18h UTC. The KNMI balloon measurements, in blue, where taken at the location of DBN (52.1° N, 5.18° E) around 18h17. Models from the ECMWF are given in red, empirical models HWM/MSISE in brown.*

ECMWF models significantly differ up to stratospheric altitudes.

Effective velocity models for the atmosphere are constructed, based on the atmospheric profiles for each bearing.

Localizing the origins of infrasound

The known parameters are: the arrival time, the bearing and the range from each of the two phases at the two arrays. From the arrival times a differential time is calculated, between the two phases. The values are: 2.944 ± 0.001 s for DBN and 3.37 ± 0.15 s for DIA. The larger standard error in the differential travel time for DIA, again, shows the loss of spatial coherency of the signal over the large aperture array. The absolute difference between DBN and DIA is explained by the difference in propagation through the dynamic atmosphere. The bearing was used to construct effective velocity models for each phase. The range is used to calculate the travel times for rays from source altitudes at each kilometer, through the effective velocity models.

The difference in bearing and range per phase can be caused by infrasound origi-
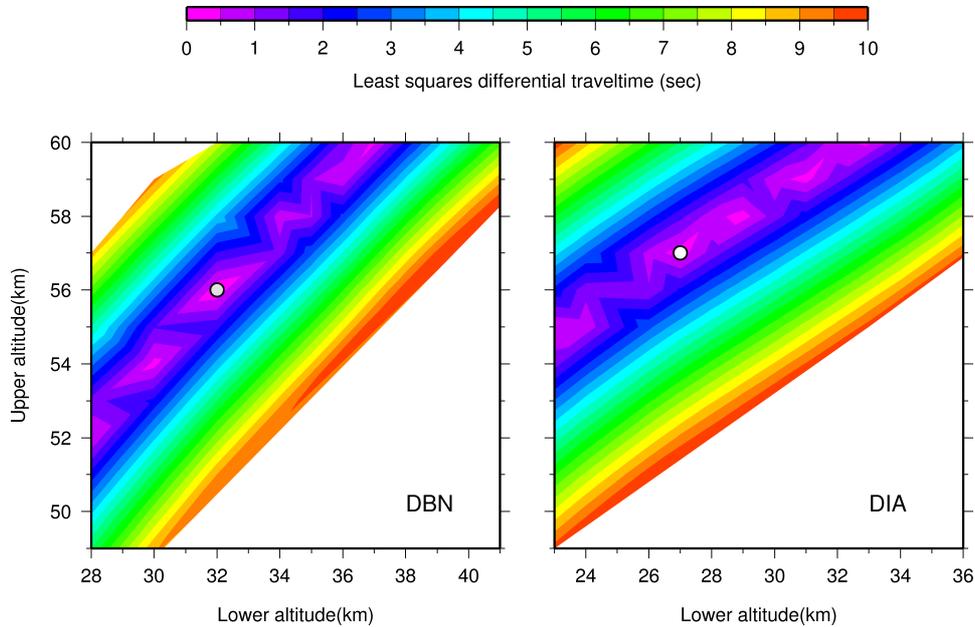
Figure 3.12: *Least squares optimization for the differential travel times between the two phases at DBN and DIA. The optimum combination of altitudes is searched for. The minima are denoted with the white dot. At DBN 32 km for the lower and 56 km for the upper altitude is found. At the DIA, 27 and 57 km explains the observed differential travel time.*

nating from different altitudes. Therefore, a least squares optimization is performed to minimize the differences between the observed and modeled differential travel times. Figure 3.12 shows the results for the derived lower and upper altitudes. The minimum for DBN of 0.03 s corresponds to a lower altitude of 32 km and upper altitude of 56 km. The minimum for DIA is at 0.22 s corresponding to 27 km and 57 km. Convergent solutions are only found for the ECMWF models within the shown ranges for the upper and lower altitudes. Other models give either solutions in the thermosphere, around 120 km, or solutions per array differing tens of kilometers in altitude. Thermospheric altitudes are unlikely because of the high attenuation at these altitudes. For this case, a more dispersed waveform should be expected instead of the recorded sharp onsets. The observed arrival times and modeled travel times resolve the origin times of the phases. These are for the first and second arrival at DBN 18h12m59.9s and 18h12m59.8s, respectively. For DIA the first and second arrival were generated at 18h13m08.0s and 18h13m08.2s, respectively. The average of the origin times confirms the time of occurrence from visual observations at 18h13m05s. The difference between DIA and DBN of 8 s is caused by uncertainties

in the atmospheric profiles and therefore in the effective velocity models. Slight changes in temperature, wind speed and direction can easily cause deviations in the order of seconds. More striking is the apparent simultaneous yield of the phases at different altitudes. The propagation velocity of infrasound is in the order of the speed of sound, i.e. 300 m/s. The velocity of the bolide, on the other hand, can be as high as tens of km/s. Therefore, the recorded differential arrival time of 3 s is caused by the inhomogeneous atmosphere, not by source duration and can be accounted for, as shown, by the different altitudes of origin. In an extreme case, with such a large difference between source duration and travel time, a phase generated last in time can arrive first. There is also a dependence on the angle of incidence with respect to the earth's surface.

■ 3.2.6   Conclusions

Two infrasound arrays in the Netherlands simultaneously recorded infrasound from a bolide. Two distinct phases were identified at each array using time domain Fisher processing. These arrivals could be pinpointed on the basis of their signal coherency and the impulsive nature of the signals. The phases appear to have originated from different altitudes in the atmosphere. This resulted from raytracing through ECMWF atmospheric models and least squares optimization of the observed and calculated differential travel times. Average altitudes in the stratosphere of 30 and 57 km are calculated for the two phases. These could derived because the bolide appeared close to the arrays. The travel times from these averaged altitudes confirm the origin time from visual observations as 2003, February 19 at 18h13m05s UTC. It is, therefore, concluded that infrasound as verification technique for the CTBT can distinguish between a moving, e.g. the observed bolide, and static, i.e. nuclear test, source. Furthermore, these results can be obtained independent of visual or other observations. Spatial coherency of infrasound, inter-array distance and the accuracy of atmospheric models play a decisive role in the applicability of the technique.

4

The detectability of infrasound in the Netherlands from the Italian volcano Mt. Etna

4.1 Abstract

Infrasound from the eruptions of Mt. Etna was detected in the Netherlands at the Deelen Infrasound Array (DIA) during the summer of 2001. Zonal cross winds lead to a deviation in the observed back azimuth. An average azimuthal deviation of 2.6° is explained by westward stratospheric winds along the infrasonic trajectories through the atmosphere. The signals have signal-to-noise power ratios lower than 0.6. The detectability of Mt. Etna's infrasound is tested on sub-arrays of the 13 elements of DIA. Doing so, sparse arrays used in the International Monitoring System (IMS) are mimicked. Both small aperture sub-arrays of 800 m and large aperture sub-arrays of 1400 m are applied. The results are evaluated on the basis of the number of detections made. The number of detections strongly increases with the number of elements. Small aperture sub-arrays perform significantly better than large aperture sub-arrays. With a factor of two reduction in the aperture, two instruments less can be used to obtain the same number of detections. Larger aperture arrays

perform less well because of the loss of spatial coherence of the infrasound. The average accuracy of the detections slightly increased, when the number of elements is increased. The result of the use of more elements is that lower signal-to-noise power ratio events could be detected. The trade-off between more detections and the larger average deviation in back azimuth and apparent sound speed causes the slight increase accuracy. The results were comparable to the detections obtained at IMS array IS26 in Germany. It is concluded that successfully applying infrasound as monitoring technique strongly depends on the array configuration. The frequency versus spatial coherence of signals will play a decisive role in detecting low signal-to-noise ratio events.

4.2   Introduction

The lowest acoustical frequency resolved by humans is about 20 Hz. Inaudible sound or infrasound has frequencies lower than this threshold. The lower frequencies for infrasound are limited by the thickness of the atmospheric layer. Therefore, the infrasonic frequency band is defined between 0.002 and 20 Hz.

Huge mass displacements in the atmosphere, like those caused by volcanic eruptions or nuclear tests, generate infrasound and can be detected at ranges of thousands of kilometres. The early period of infrasound developments came to an end with the Limited (Partial) Test Ban Treaty in 1963 that forced states to conduct nuclear tests underground. In recent years, since the signing of the Comprehensive Nuclear-Test-Ban Treaty (CTBT), infrasound research has been expanding again. Sixty infrasound arrays are currently being installed world wide as part of the International Monitoring System (IMS) for verification of the CTBT [*PrepCom*, 1997].

Infrasound from volcanoes measured in the far field is capable of penetrating the atmosphere over large ranges because of its low frequency content, i.e. between 0.5 and 2 Hz [*Liszka and Garcés*, 2002]. Near-field measurements of infrasound from volcanoes give information about tremor sources, conduit and melt properties [*Ripepe et al.*, 1996; *Garcés et al.*, 2000].

The detection of infrasonic signals with arrays is based on signal coherence. Signal coherence decreases with increasing inter-array element distance [*Mack and Flinn*, 1971] while higher resolution might be achieved with larger aperture arrays. The resolution performance of an array also depends on the position of the instruments [*Haubrich*, 1968]. The larger the array aperture, the lower the resolved frequencies. In this paper, we investigate the detectability of infrasound from the 2001 Mt. Etna eruptions, in Italy, at the Deelen Infrasound Array (DIA) in the Netherlands. The influence of zonal cross winds on the recorded back azimuth is analyzed. Furthermore, the number of sensing elements from DIA are systematically lowered from 13 to 4 to mimic sparse IMS arrays, like the five element array IS26 in Germany.
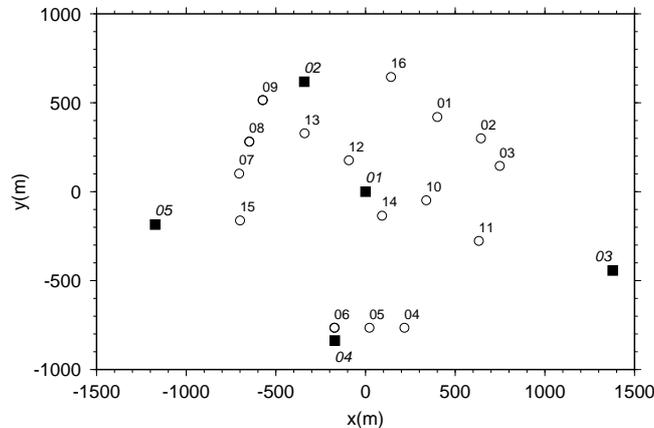
Figure 4.1: *The layout of 16 KNMI microbarometers of DIA (circles) and the five MB2000s of IS26 (filled squares, oblique numbers). Instruments 06, 08 and 09 of DIA were not operational.*

4.3   Infrasound data acquisition and processing

■ 4.3.1   The Deelen Infrasound Array and IMS array IS26

Infrasound is monitored with arrays of microbarometers. Arrays are deployed to increase the detectability of signals as signal-to-noise ratios are often lower than 1. Signal stacking enhances the signal-to-noise ratios. Furthermore, information on the signal's back azimuth ϕ, and apparent sound speed c_{app}, can be derived by applying array processing techniques. Spatial noise reducers are coupled to each instrument to reduce further noise caused by wind in an analog manner [*Hedlin et al.*, 2003].

DIA is equipped with 16 KNMI differential microbarometers and capable of measuring events of CTBT interest [*Evers and Haak*, 2001b]. Spatial noise reduction at each sensor is achieved by using six porous hoses. These are configured in a spider form, i.e. a radial layout of the hoses, with a total diameter of 10 m. DIA has an aperture of approximately 1400 m and is located in the eastern part of the Netherlands on an Air Force base. This non-IMS array is used to perform sonic boom monitoring and CTBT related research. Figure 4.1 gives the configuration of DIA as shown by the circles. Instruments 06, 08 and 09 were not operational at the time of the Etna eruptions in the summer of 2001. IMS array IS26 is located in the Bavarian Forest in southern Germany. IS26 consists of five absolute microbarometers (type: MB2000) and noise reduction is done with a metal pipe array of 18 m diameter at each sensor. The atmosphere is sampled with a total of 96 inlets connected to the pipe array's four arms [*Hartmann and Henger*, 2000]. The filled squares in Figure 4.1 give the configuration of IS26.

■ 4.3.2 Signal detection on the basis of the Fisher ratio

Array processing techniques are based on signal coherence. Detection algorithms trigger on specific threshold values, being for example: signal-to-noise ratio, correlation, coherency, LTA/STA. Evaluation of the Fisher ratio is another approach to find a systematic pattern in array data. *Melton and Bailey* [1957] defined the Fisher ratio as:

$$F = \frac{T(N-1)}{N(T-1)} \frac{\sum_{t=1}^{T}(\sum_{n=1}^{N} x_{nt})^2 - \frac{1}{T}(\sum_{t=1}^{T}\sum_{n=1}^{N} x_{nt})^2}{\sum_{t=1}^{T}\sum_{n=1}^{N} x_{nt}^2 - \frac{1}{N}\sum_{t=1}^{T}(\sum_{n=1}^{N} x_{nt})^2} \qquad (4.3.1)$$

where the variances of N independent observations of quantity x are evaluated over a timespan T. Basically, the recordings contain a part which can be attributed to a common cause as well as deviations not having the same origin. Therefore, the F-ratio is a scaled measure of coherent signal-to-noise power ratio and describes the signal likelihood. The F-ratio is evaluated for a variety of back azimuths ϕ and apparent sound speeds c_{app} of the energy, i.e. beamforming as commonly used in seismology [*Blandford*, 1974]. This evaluation is done on a slowness, $\vec{p}$, grid where $|\vec{p}| = \frac{1}{c_{app}}$. A grid search is performed to find the $\vec{p}$ value which explains the observed travel time differences over the array, resolving ϕ and c_{app} as event characteristics.

4.4 Volcanic infrasound from Mt. Etna

■ 4.4.1 Detections at DIA and IS26

Mt. Etna on the island of Sicily (Italy) violently erupted during the summer of 2001. Infrasound from explosions and huge mass displacements in the atmosphere were recorded at DIA and IS26. Although Mt. Etna was almost continuously active, data from two days of intense activity, being July 28 and 29, is concentrated on. Figure 4.2 gives the results for the F-ratio analysis of 24 hours of infrasound recorded at DIA and IS26 starting on 2001, July 28 12h00 UTC (local time−2h). The data for both arrays are band-pass filtered with a second order Butterworth filter having corner frequencies of 0.3 and 4.0 Hz. The F-ratio is evaluated on a $\vec{p}$ grid of 100 by 100 points forming 10.000 beams. The 24 hours recordings are split up in bins of 25.6 seconds overlapping 50%. The lower frames in Figure 4.2 give the maximum value for the F-ratio in each bin. The corresponding values for c_{app} and ϕ are given in the middle and top frames, respectively.

F-ratio values for DIA hardly show any infrasonic events during the day and early evening of July 28. The F-ratio increases around 21h. Coherent infrasound is detected as also indicated by the apparent sound speed velocity which converges to sound speed values. The reason for the sudden increase in F-ratio is twofold. Firstly and most importantly, the atmosphere becomes more stable after sunset, turbulent and convectional structures are no longer activated by solar heat fluxes. Secondly,
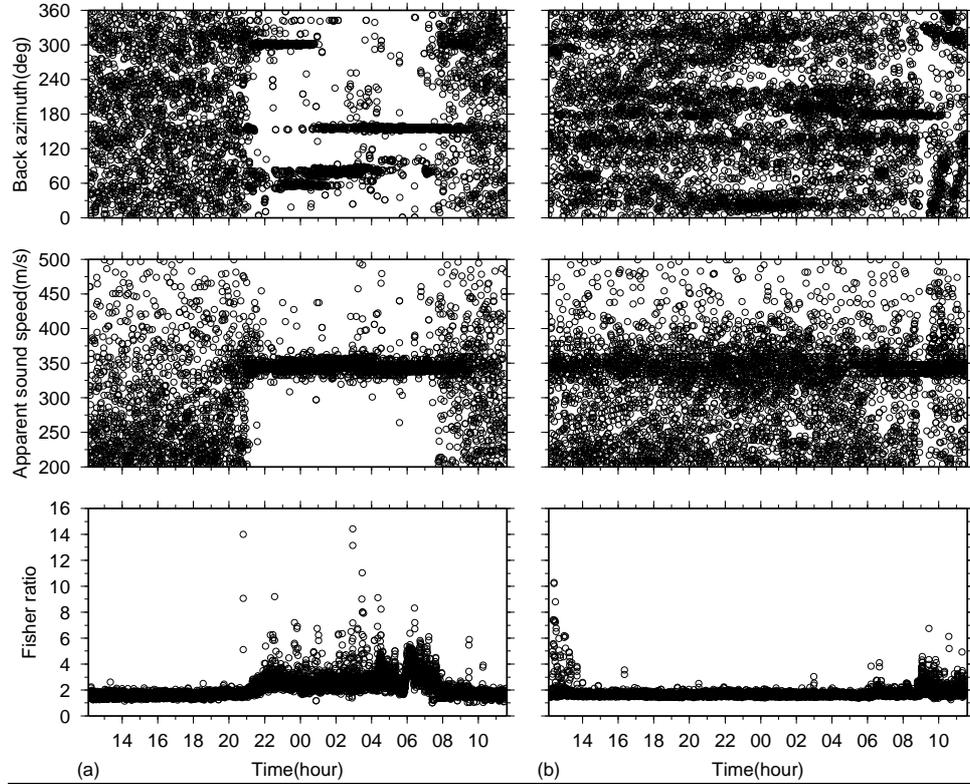
Figure 4.2: *F-ratio analysis of 24 hours of infrasound recorded in DIA (a) and IS26 (b), the time axis starts on 2001, July 28 12h00 UTC. The maximum F-ratio is plotted in the lower frame for each time bin of 25.6 s, the corresponding values for c_{app} and ϕ are plotted in the top two frames.*

noise around the array becomes less during the evening and night since human activity diminishes. The top frame of Figure 4.2(a) shows three distinct directions from which the infrasound is coming towards DIA. A stable source is present to the northeast of DIA at 300° between 21h and 1h on the next day. Oceanic waves interacting with the atmosphere are the source, called microbaroms [*Posmentier*, 1967], and are located in the Atlantic Ocean [*Evers and Haak*, 2001b]. A less well defined source is present eastwards of DIA. Between 21h and 4h30 a source seems to wander from 55° toward 85°. This energy is attributed to a local source because of its unstable character, no further explanation can be given for this source. A persistent back azimuth with an average value of 155.3 ± 0.1° is resolved from 00h until at least 09h. This back azimuth is in the direction of Mt. Etna. The average apparent sound speed is found to be 340.6 ± 0.3 m/s. The total number of detections used to calculate these averages is 973. A detection of Mt. Etna is defined as an arrival

with a F-ratio higher than 2 within a time segment of 25.6 s. The back azimuth variation may be between 7° West and 3° East around the true back azimuth and an apparent sound velocity between 180 and 480 m/s is acceptable. The tolerance can be set much sharper as will be seen in the next sections.

Data from IS26, Figure 4.2(b), appear more noisy. The stable and quiet nightly atmosphere does not result in the detection of coherent infrasound on the five element array. A stable back azimuth is visible between 06h and 10h on the morning of July 29, especially pronounced during a quiet moment around 09h. Its average back azimuth of 178.4 ± 0.1° points towards Mt. Etna, the corresponding apparent sound speed is 341.7 ± 1.1 m/s. These averages are taken over 184 detections.

■ 4.4.2 Azimuthal deviations

The true back azimuths for DIA and IS26 are 152.7° and 174.9°, respectively. Compared to the observed back azimuths an azimuthal deviation of 2.6° at DIA and 3.5° at IS26 is found. Figure 4.3 shows these azimuthal deviations with respect to Mt. Etna. The origin of the infrasound found by cross bearing is located to the West of Mt. Etna.

Infrasonic wave propagation through the atmosphere is dependent on the wind and temperature structure. Raytracing through a moving atmosphere is conducted following the tau-p method described by *Garcés et al.* [1998]. Infrasound travels through the atmosphere up to thermospheric altitudes. A model describing the wind and temperature structure up to these altitudes is provided by *Hedin et al.* [1996]. This so-called HWM/MSISE model is taken at the halfway position of 10°E, 45°N on 2001, July 29 at 06h UTC, to get an indication of the azimuthal deviation. Although, two-dimensional lateral variations between Mt. Etna and DIA may exist in the models, infrasonic paths will mainly be influenced by stratospheric zonal cross winds which are similar over Europe, justifying the use of the halfway model. Figure 4.4 shows the results for raytracing from Mt. Etna towards DIA through the HWM/MSISE model. The paths the rays follow (lower frame of Figure 4.4(a)), either bend in the stratosphere or in the thermosphere. Especially thermospheric returns are split in several branches originating from altitudes between 110 and 130 km. The corresponding travel times are shown in the top frame of 4.4(a). The first energy to arrive in DIA is from stratospheric origin and subsequently low to high thermospheric returns arrive. It takes the energy, on average, two hours to travel to DIA. Figure 4.4(b) shows the bounce points on the Earth's surface for rays shot in the direction from Mt. Etna to DIA. It follows that rays do not arrive at DIA because of zonal cross winds deviating the rays towards the West. Stratospheric winds cause the deviation and have an East to West direction during summer, with speeds over 50 m/s at around 60 km altitude. Rays that should arrive at DIA would have to leave Mt. Etna in a more easterly direction, leading to a translation of the wavefront. This translation causes the observed azimuthal deviations and it can range from 2° to 5° (Figure 4.4(b)).
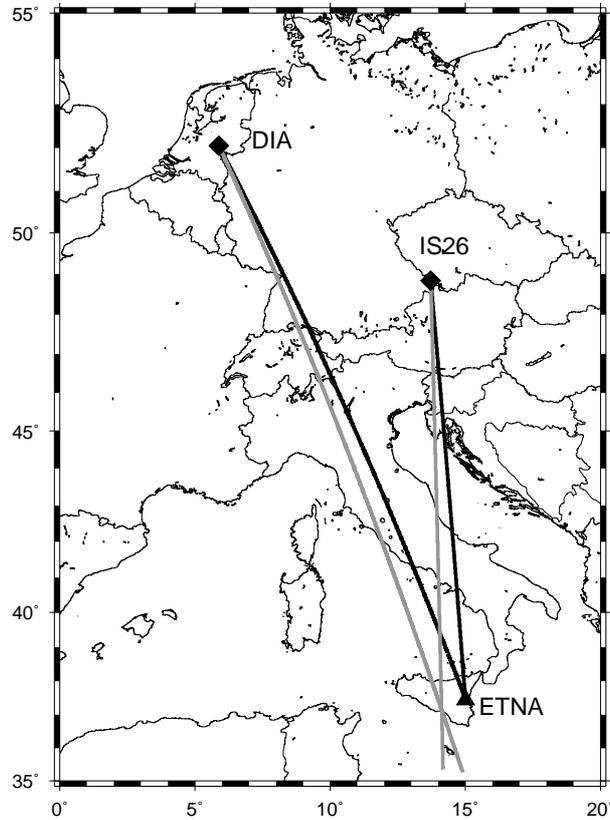
Figure 4.3: *Map showing the observed back azimuths (in gray) and true values (in black) from DIA and IS26 towards Mt. Etna.*

■ 4.4.3   Infrasonic waveforms from Mt. Etna

Infrasound from Mt. Etna is recorded at DIA for at least 9 hours. A wide variety of signal-to-noise power ratios are detected as indicated by the alternating F-ratio values, see Figure 4.2(a). Distinct events, i.e. sub-sonic and super-sonic airplanes, give rise to high F-ratios throughout the dataset. The most coherent waveforms from Mt. Etna are detected between 06h and 07h during the morning of July 29. One of the highest F-ratios from Mt. Etna's infrasound is 9 corresponding to a signal-to-noise power ratio of 0.6. Figure 4.5 shows the individual recordings around the time of the highest F-ratio in thin gray lines. These recordings are time-aligned in the direction of Mt. Etna. The best beam is shown as the black line. Infrasound from Mt. Etna can be identified there where the individual waveforms constructively add up in the best beam, see for example around 7 s and around 14 s. On the other
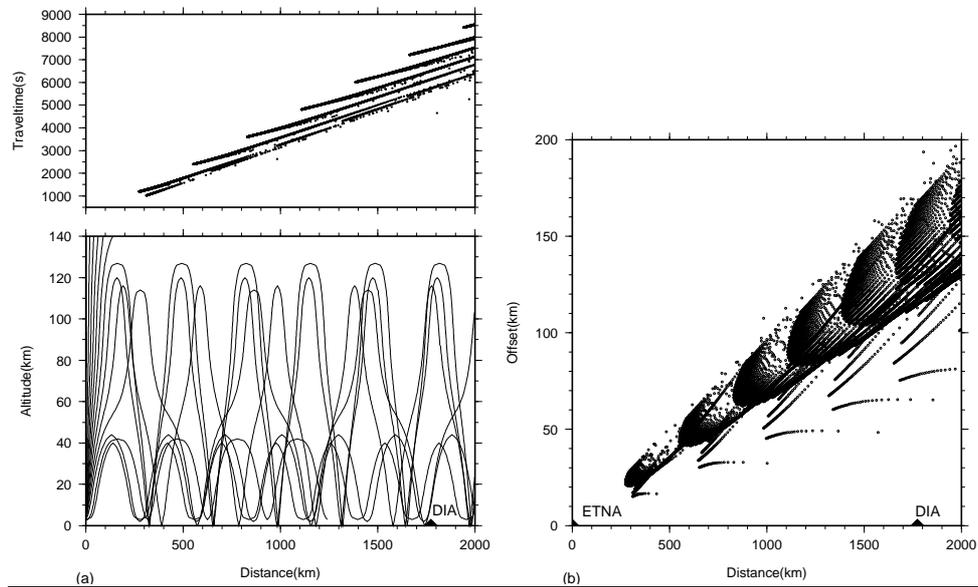
Figure 4.4: *The atmospheric trajectories and travel times as follows from raytracing from Mt. Etna towards DIA. The effective sound speed is calculated on the basis of HWM/MSISE models (a). The bounce points of the rays on the Earth's surface (b) for rays shot from Mt. Etna in the direction of DIA. The rays are deviated westwards under the influence of zonal stratospheric cross winds.*
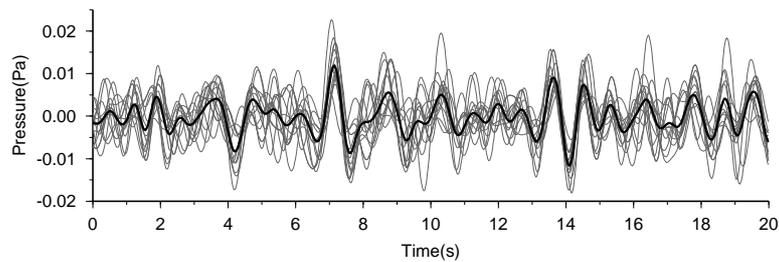
Figure 4.5: *Individual recordings of the 13 microbarometers of DIA in gray, the best beam in black. The time axis start at 06h14m38.8s on 2001, July 29 UTC. A second order Butterworth filter is applied with corner frequencies of 0.5 and 1.5 Hz.*
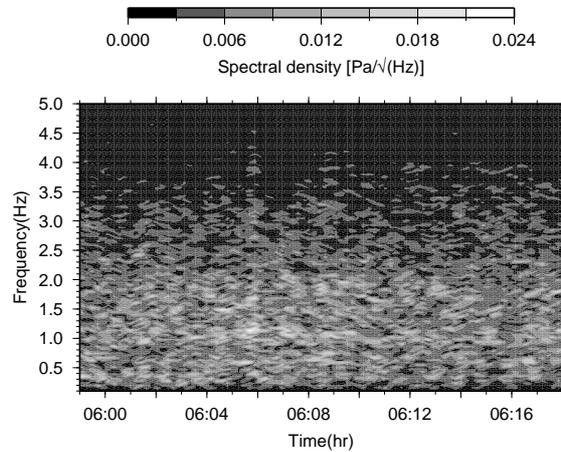
Figure 4.6: *Spectrogram for the best beam in the direction of Mt. Etna starting at 05:59 on 2001, July 29 UTC. The data are prefiltered with a second order Butterworth filter having corner frequencies of 0.3 and 4.0 Hz. The spectrogram is calculated for time bins of 25.6 s (1024 samples) with a 50% overlap, resolving spectral densities each 0.039 Hz.*

hand, noise is identified as non-coherent waveforms hardly contributing to the best beam, for example around 12 s and around 17 s. The spectral contents of the best beam towards Mt. Etna is displayed in Figure 4.6. The spectrogram shows spectral densities contoured for each 0.039 Hz as derived from time bins of 25.6 s (1024 samples). The dominant frequencies contributing to the best beam appear between 0.4 and 1.5 Hz as denoted by the light colors. An average frequency content of 1 Hz follows from a closer inspection of the actual waveforms.

4.5 The detection capability of sub-arrays of DIA

■ 4.5.1 Number of detections

IS26 detected less energy from Mt. Etna than DIA, although, IS26 is situated 500 km closer to the volcano (Figure 4.2). There can be several explanations why IS26 seems to be less sensitive. Firstly, IS26 could have less sensitive or more noisy instruments. Tests at the authors' institute have shown a comparable noise level and sensitivity for both instruments. The noise levels are low compared to the ambient noise in the atmosphere. Secondly, local noise levels could significantly differ at both arrays. IS26 is located in the forest which reduces the noise because the vegetation does not allow large turbulent structures to exist and also refracts the wind field. On the other hand, DIA is located on an open field and is thus more affected by
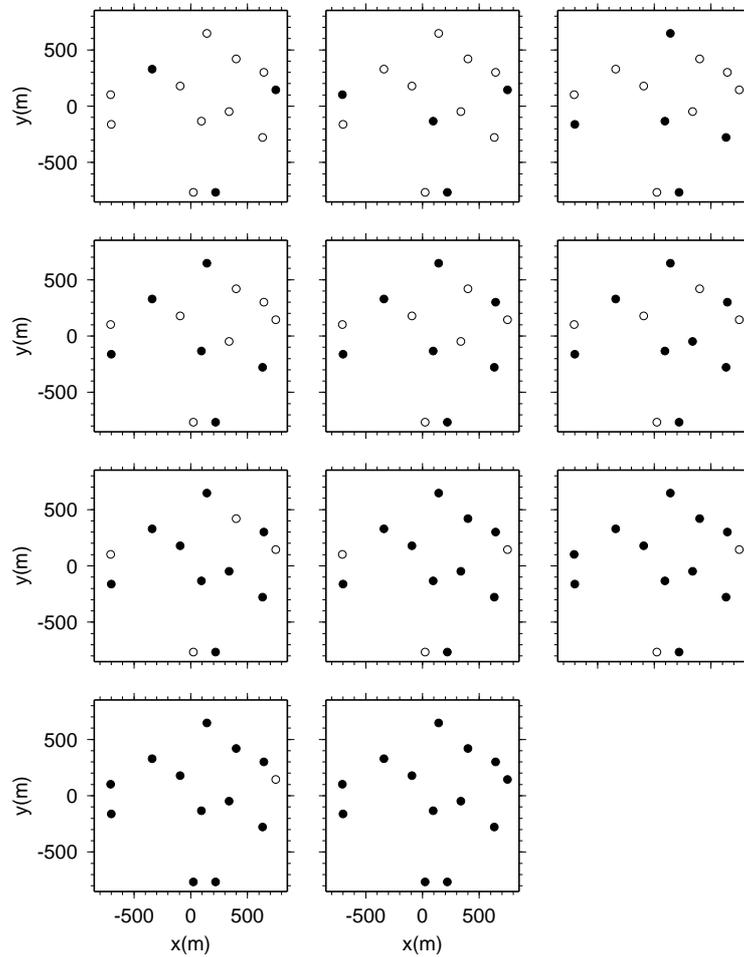
Figure 4.7: *Large sub-arrays of DIA with a maximum aperture of 1400 m. The elements used in the analysis are denoted by the filled circles. The number of active elements is increased from three, upper left corner, to 13 in the lower right corner.*

turbulence and wind. The noise level in DIA is, therefore, expected to be higher which should result in fewer detections. Thirdly, the array layout from IS26 differs in both configuration and number of elements from DIA which may influence the number of detections. The last hypothesis is tested by assessing several sub-arrays of DIA.

Two sets of sub-arrays are constructed of both small and large apertures. The large sub-arrays have a maximum aperture of 1400 m (Figure 4.7), while the small sub-
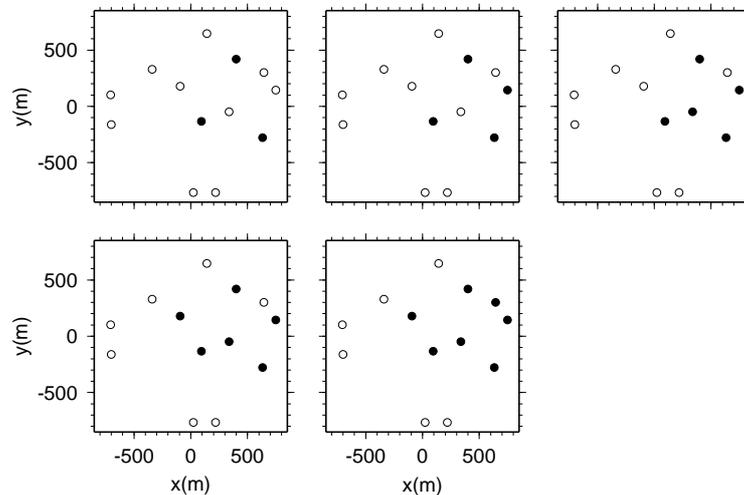
Figure 4.8: *Small sub-arrays of DIA with a maximum aperture of 800 m. The active elements, given by the filled circles, are increased from three to seven.*

arrays have a maximum aperture of 800 m (Figure 4.8). The sub-array layouts are chosen such that the array response has a circular and peaked main lob with low amplitude side lobes. This guarantees high resolution and omni-directional properties of the sub-array. Figure 4.9 shows the number of detections made by sub-arrays of DIA as a function of the number of elements as circles for the large aperture sub-arrays and triangles for the small sub-arrays. The number of detections for IS26 is given as a square. Clearly, the number of detections increases with the number of elements. The small aperture sub-arrays perform significantly better than the large aperture sub-arrays. The loss of spatial coherence of the infrasound causes the decrease in number of detections with large aperture arrays. There is an almost linear increase in the number of detections with the number of elements for small aperture sub-arrays. For large aperture sub-arrays, the largest gain in number of detections is indicated by the steepest part of the curve between seven and nine elements. Further increase of the number of elements seems to lead to saturation. The saturation effect is also partly controlled by the maximum number of detections possible; the amount of infrasound from Mt. Etna is limited. Significant increase is also seen between three and six elements in both aperture sub sets, but arrays of less than five elements suffer from resolution loss due to spatial aliasing [*Evers and Haak*, 2001].
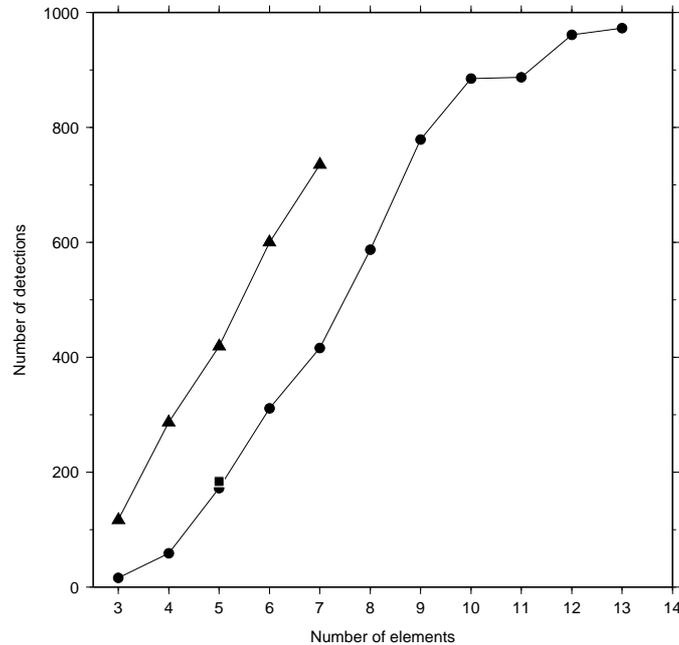
Figure 4.9: *Number of detections versus the number of elements for large aperture sub-arrays of DIA, circles, and IS26, square at five elements. The number of detections for small aperture sub-arrays are represented by the triangles.*

■ 4.5.2   Accuracy of the detections

Figure 4.10 shows the accuracy of the detections as function of the number of elements, circles for the large aperture sub-arrays and triangles for the small aperture sub-arrays. The averages are calculated by comparing the detections made by the sub-arrays with the 13 element solutions. The lower frame shows the average deviation in the resolved back azimuth. The middle frame shows these results for the apparent sound velocity. The top frame shows the average signal-to-noise power ratio of the detected events. There is a slight trend of increasing accuracy in both apparent sound speed and back azimuth frames. The average signal-to-noise power ratio clearly decreases with an increase in number of elements. This explains why the velocity and back azimuth curves only show a slight increase in accuracy. By increasing the number of elements, less coherent arrivals can be detected. This also follows from the decrease in signal-to-noise power ratios when more elements are used. These less coherent arrivals are more difficult to characterize in terms of apparent sound speed and back azimuth. The spread in resolved values increases, leading to larger standard deviation in the solutions. In general, the size of an ar-
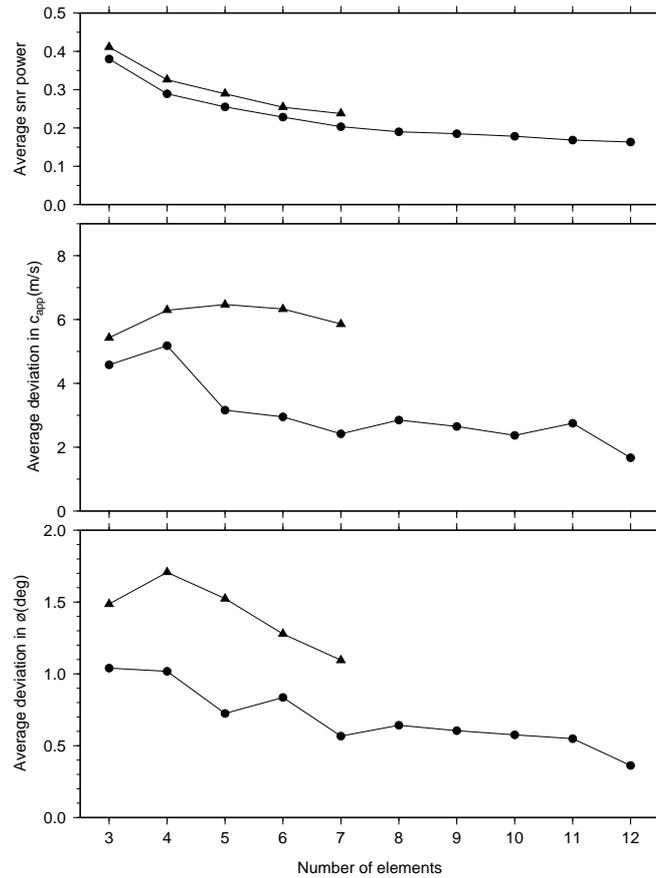
Figure 4.10: *The average deviation in back azimuth ϕ, lower frame, apparent sound velocity c_{app}, middle frame and signal-to-noise snr power ratio, top frame, as function of the number of elements. The results for the large aperture sub-arrays are given by the circles, the triangles represent the small aperture sub-arrays.*

ray controls the accuracy of the derived back azimuth and apparent sound speed. Therefore, the large aperture sub-arrays appear to perform slightly better in terms of accuracy than the small aperture sub-arrays.

4.6   Conclusions

Infrasound from Mt. Etna has accurately been detected by the Deelen Infrasound Array (DIA) in the Netherlands on 2001, July 28 and 29. The atmosphere becomes quiet and stable during the night enabling a clear identification of far-field volcanic infrasound. These ideal measurement conditions are due to minimization of the noise caused by human activity and the lack of solar heating. Daytime noise is partly generated by turbulent structures induced by heat fluxes. Energy that travels 1774 km from Mt. Etna to DIA is influenced by the wind and temperature structure of the atmosphere along its path. Impedance contrasts in the atmosphere lead to bending of the infrasonic rays in the stratosphere and thermosphere. Infrasound returns from approximately 40 km altitude in the stratosphere and several altitudes in the thermosphere between 100 and 130 km. Zonal cross winds explain the average 2.6° azimuthal deviation observed in DIA. Deviations are caused by westward winds in the stratosphere reaching over 50 m/s at 60 km altitude. The signals have low signal-to-noise power ratios; one of the most coherent waveforms has a signal-to-noise power ratio of 0.6. The detection capability of sub-arrays of DIA has been tested by lowering the number of active elements from 13 to three for small, 800 m, and large, 1400 m, aperture sub-arrays. The number of detections versus the number of elements is used as criterion. The two main findings are: small aperture sub-arrays perform much better than large aperture sub arrays and the number of detections strongly increases with the number of elements. With a reduction in size of the array with a factor of two, two instruments less can be used to obtain the same number of detections. These findings are based on the observations and calculations made for volcanic infrasound specifically with a frequency content of 0.4 to 1.5 Hz. Increasing the number of instruments will slowly lead to saturation in the number of detections. This is also partly caused by the limited amount of detections that can be made. Larger aperture arrays perform less well because of the loss of spatial coherence of the infrasonic data. The average accuracy of the detections is only slightly improved. Increasing the number of element leads to the ability to detect signals with lower signal-to-noise power ratios but the parameter estimation of these events is less accurate. The trade-off between more detections and less accuracy causes the rather constant average deviation. Large aperture sub-arrays perform slightly better than small aperture sub-arrays in terms of accuracy. The obtained results are comparable to the detections obtained from the five element IMS array IS26 in Germany.

The detection capability of infrasound arrays is not only a function of the number of elements. The position of the instruments with respect to each other control the

resolution and also the total aperture of the array. Therefore, the frequency versus the spatial coherence of the signals plays an important role in determining the array layout and, consequently, the success of infrasound as monitoring technique.

5

Ground truth infrasound from chemical explosions

5.1 Seismo-acoustic analysis of the gas-pipeline explosion near Ghislenghien in Belgium

■ 5.1.1 Abstract

A high pressure gas-pipeline exploded near Ghislenghien in Belgium, on 2004, July 30. Seismic energy of this event was recorded at three nearby seismometers. The origin time of the explosion was determined by analyzing the Rayleigh waves and found to be 06h55m27±2 s UTC. Ground truth of the explosion was invoked to assess the accuracy of the location derived from infrasound data recorded over western Europe. Different infrasonic phases were identified by using array processing techniques and raytracing through atmospheric models. The analysis showed that the derived location was situated 13 km from the true location. The total area of the uncertainty ellipse, or area to be searched if the source was of unknown origin, was 690 km^2. Next to the origin time and location, the yield was calculated by comparing infrasonic stratospheric amplitudes to those from a high explosives dataset and was estimated at 40.9 tons high explosives equivalent. In summary, this study

Figure 5.1: *Map of the explosion site and recording instruments. The star gives the position of the explosion in Belgium near the village of Ghislenghien at [3.87° E, 50.66° N], located approximately 40 km southwest of Brussels (triangle). Three short-period seismic stations are located nearby the explosion site and denoted by the circles. Furthermore, five diamonds represent the infrasound arrays that recorded energy from the explosion.*

illustrates the capability of seismic and infrasound data in forensic investigations. Furthermore, the potential of infrasound as a monitoring or verification technique is addressed.

■ 5.1.2 Introduction

Large explosions are known to generate both infrasound and seismic signals. Infrasound is inaudible sound with a lower frequency cut-off limited by the thickness of the atmosphere or an atmospheric layer. The human hearing threshold of 20 Hz is generally taken as upper limit. Examples of the wide variety of explosive sources are nuclear tests (e.g. [*Posey and Pierce*, 1971]) and truck bombs ([*Koper et al.*, 1999]). *Le Pichon et al.* [2002b] and *Evers and Haak* [2001b] reported infrasound from bolides and *Ripepe et al.* [1996] analyzed volcanic signals from Stromboli. The explosion of a high pressure gas-pipeline occurred near the city of Ghislenghien, Belgium, around 06h57 UTC on 2004, July 30 as reported by the operator Fluxys (personal communication). Ghislenghien is located approximately 40 km southwest of Brussels (Figure 5.1). The 1 m diameter pipe was split in two segments each extending over approximately 15 km until the first shutting-down valve. During the

following fire, a total of about two million cubic metres of gas were burned, being the content of the two pipe segments. Vegetation was burned in a radius of 200 to 300 m around the event. Flames were reported to reach an altitude of 200 m, as described by *Manders* [2004]. On a nearby highway 500 m away from the site, passing motorists had their skin burned. Nearby cars and buildings were set on fire. Seismic energy was recorded up to a distance of several tens of kilometers while infrasound traveled at least as far as southern Germany. The event resulted in the deaths of 18 people, immediately after the explosion. Recently, the study of infrasound gained renewed interest because of its use as verification technique for the Comprehensive Nuclear-Test-Ban Treaty (CTBT, see http://www.ctbto.org). In this context, we study the use of infrasound and seismic measurements to resolve explosion's characteristics like: origin time, location and yield. Furthermore, phase identification of the infrasonic waveforms is achieved by including empirical and actual atmospheric models. Simultaneous observations of infrasonic and seismic energy contribute to forensic investigations of explosions of both known and unknown origin, quantifying the capability of infrasound as monitoring technique.

■ 5.1.3 Seismic observations and origin time

The explosion was recorded at three nearby short period seismic stations operated by the Royal Observatory of Belgium (Figure 5.1). In Figure 5.2 we show the distance versus time relation of stations SKQ, SNF and BOU. The black line is described by a speed of 346 m/s, aligning the secondary arrival. This indicates that we are dealing with either an acoustic -infrasound- wave or an air-coupled Rayleigh wave [*Koper et al.*, 1999]. The particle motion from the one three component station SKQ was investigated to distinguish between an infrasound and an air-ground coupled wave. If the wave train shows retrograde particle motion it should be identified as a Rayleigh wave, otherwise longitudinal motions would reveal an infrasound wave. The wave appeared to be of Rayleigh wave nature.

The gray line through the first arrival has a velocity of 5 km/s and might be a P-wave as direct seismic wave from the explosion. From Figure 5.2 it follows that the origin time of the explosion was 06h55m27$\pm$2 s UTC. Photographic material shows huge roaring flames during the initial fire. In personal communication, Fluxys reported that the fire was active until at least 07h45 when small flames were still observed. However, the seismic data do not give any indication of acoustic or seismic waves associated with the fire, as observed by *Koper et al.* [2003]. The lack of clear P onsets from the explosion makes it difficult to localize the source on the basis of seismic data; most of the energy went into the atmosphere as infrasonic energy.
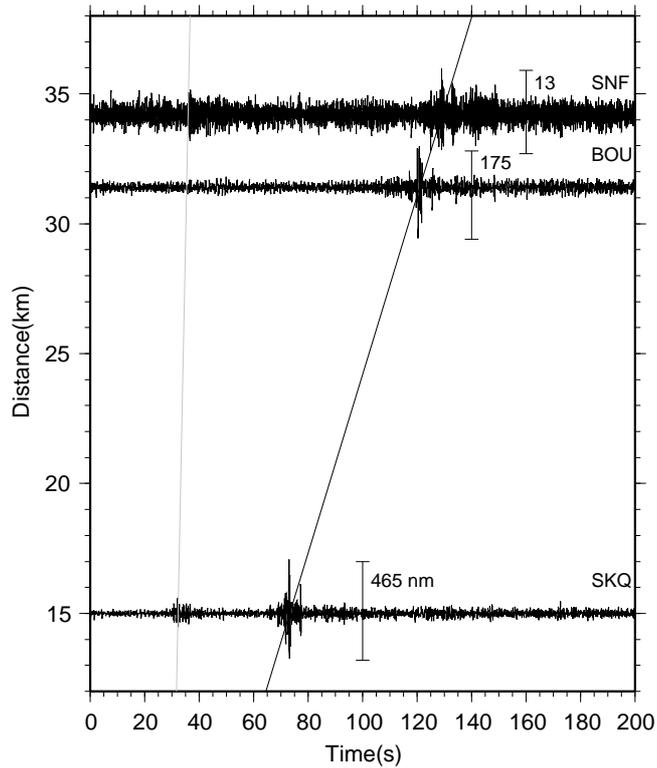
Figure 5.2: *The recordings from the seismic stations in Belgium plotted as epicentral distance versus time graph. The time axis zero time is 06h55m0.0s. The traces of stations SKQ and BOU are band-pass filtered with a second order Butterworth filter with corner frequencies of 0.5 and 5 Hz. The data from SNF are filtered between 1 and 10 Hz. The peak amplitude of the ground displacement is also given. The black line connects the Rayleigh wave arrivals and has a velocity of 346 m/s. The rather suggestive gray line has a velocity of 5 km/s and combines a possible P-wave. The resolved origin time of the explosion is 2004, July 30 06h55m27±2s UTC.*
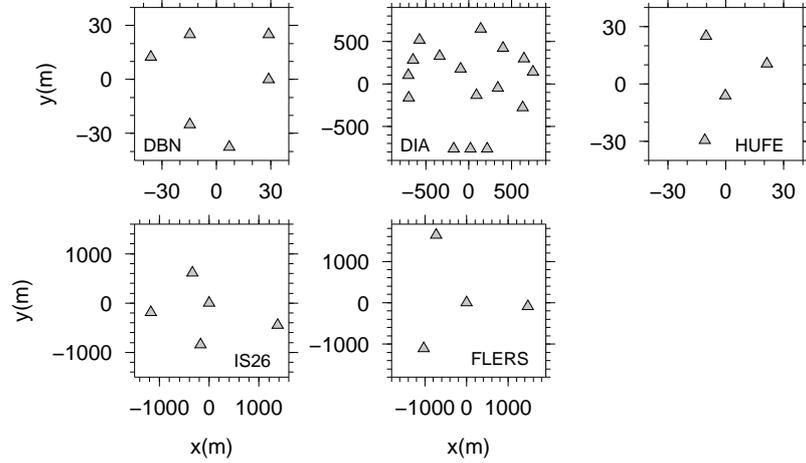
Figure 5.3: *The array layouts of the infrasound stations showing a wide variety in number of microbarometers and apertures.*

■ 5.1.4 Infrasound observations

The event was observed at five infrasound arrays in countries bordering Belgium. In the Netherlands, energy was found at microbarometer arrays in De Bilt (DBN) and in Deelen (DIA) [*Evers and Haak*, 2003]. Infrasound was recorded in France at an array near Flers deployed by the Commissariat à l'Energie Atomique (CEA) [*Le Pichon et al.*, 2002a]. In Germany, infrasonic signals were detected at the Bundesanstalt für Grund- und Rohstoffe (BGR), measured by infrasound array IS26 [*Hartmann and Henger*, 2000] which is part of the International Monitoring System for the CTBT. There was also a temporary array installed to the North of Hannover in the village of Hufe. In Figure 5.3, the array configurations are given; array apertures range from 60 to 2400 meters, while the number of microbarometers varies between 4 and 16.

Signal detection, processing and beam-forming were applied based on both the Fisher ratio as described by *Melton and Bailey* [1957] and the Progressive Multi Channel Cross Correlation (PMCC; [*Cansi*, 1995]) which are commonly used in infrasound processing (e.g. [*Le Pichon et al.*, 2002a]; [*Evers and Haak*, 2003]). For these two algorithms, the cross correlation and Fisher ratio are calculated in the time domain to detect coherent infrasound signals. The time domain Fisher ratio is given in equation 5.1.1.

$$F = \frac{T(N-1)}{N(T-1)} \frac{\sum_{t=1}^{T} (\sum_{n=1}^{N} x_{nt})^2 - \frac{1}{T}(\sum_{t=1}^{T} \sum_{n=1}^{N} x_{nt})^2}{\sum_{t=1}^{T} \sum_{n=1}^{N} x_{nt}^2 - \frac{1}{N} \sum_{t=1}^{T} (\sum_{n=1}^{N} x_{nt})^2} \qquad (5.1.1)$$

Essentially, the variances of N independent observations -the array elements- of quantity x -the air pressure fluctuations- are evaluated over a timespan T and multiplied by the degrees of freedom. Equation 5.1.2 relates the Fisher ratio to signal-to-noise power ratio (snr), assuming a plane wave and uncorrelated noise.

$$F = N \cdot snr + 1 \qquad\qquad (5.1.2)$$

Array processing techniques like beam-forming enable the construction of a best beam, being the sum of all phase aligned traces in the direction of the source. Figure 5.4 shows the detection and processing results for the 13 active elements of DIA. A huge increase in Fisher ratio triggers a detection of the infrasound from the initial explosion as visible in the lower frame. A stable back azimuth and apparent sound speed are retrieved through beam-forming on a 100x100 slowness grid. The best beam and its spectrogram are shown in the top two frames of Figure 5.4. A coda of infrasound after the initial explosion lasts for at least 15 minutes, as follows from the high Fisher ratios and a lasting stable back azimuth and apparent sound speed. This coda is caused by roaring flames reaching hundreds of meters into the atmosphere.

Table 5.1 summarizes the characteristics of the infrasound recordings for all arrays based on similar detection and parameter estimation as used for DIA. Infrasound is clearly detected at all arrays; the waveforms, back azimuths, frequency content and arrival times suggest that we are dealing with infrasound from the explosion. The average back azimuth is calculated by averaging over the complete duration of the signal.

Figure 5.5 shows the best beams for the different arrays as function of the distance. All traces start with an impulsive event, the initial explosion, followed by a coda of infrasound with decreasing amplitude, except for Flers where clear high amplitude arrivals are visible throughout the wave train. These are explained in the next section on phase identification. In the most distant arrays, Hufe and IS26, the coda's energy is buried in the noise earlier because of its rather high frequency content and low amplitude.

The map on the left of Figure 5.6 shows the results of cross bearing the derived back azimuths, their uncertainties (in gray) and a star denoting the true location. An ellipse is drawn through the outermost intersection points to confine the total area of interest in case the event was of unknown origin. The cross is the center of the ellipse located at 20 km distance of the source, the total area comprised by the ellipse is 1290 km^2 . The uncertainties in this ellipse are given by the accuracy of the determined bearings (in gray). An alternative average location is derived by analyzing each cross-bearing intersection individually. The trigonometric sine is taken from the difference of two bearings and used for weighting the intersection point. The difference of the two bearings ranges between 0 and 90 degrees and the associated weights, from taking the sine, vary between 0 and 1. Doing so, more importance is given to intersection points from more perpendicular bearings that are less sensitive to small errors in one of the bearings. An intersection point from two almost parallel bearings is more unreliable since it can be displaced over large distances by small
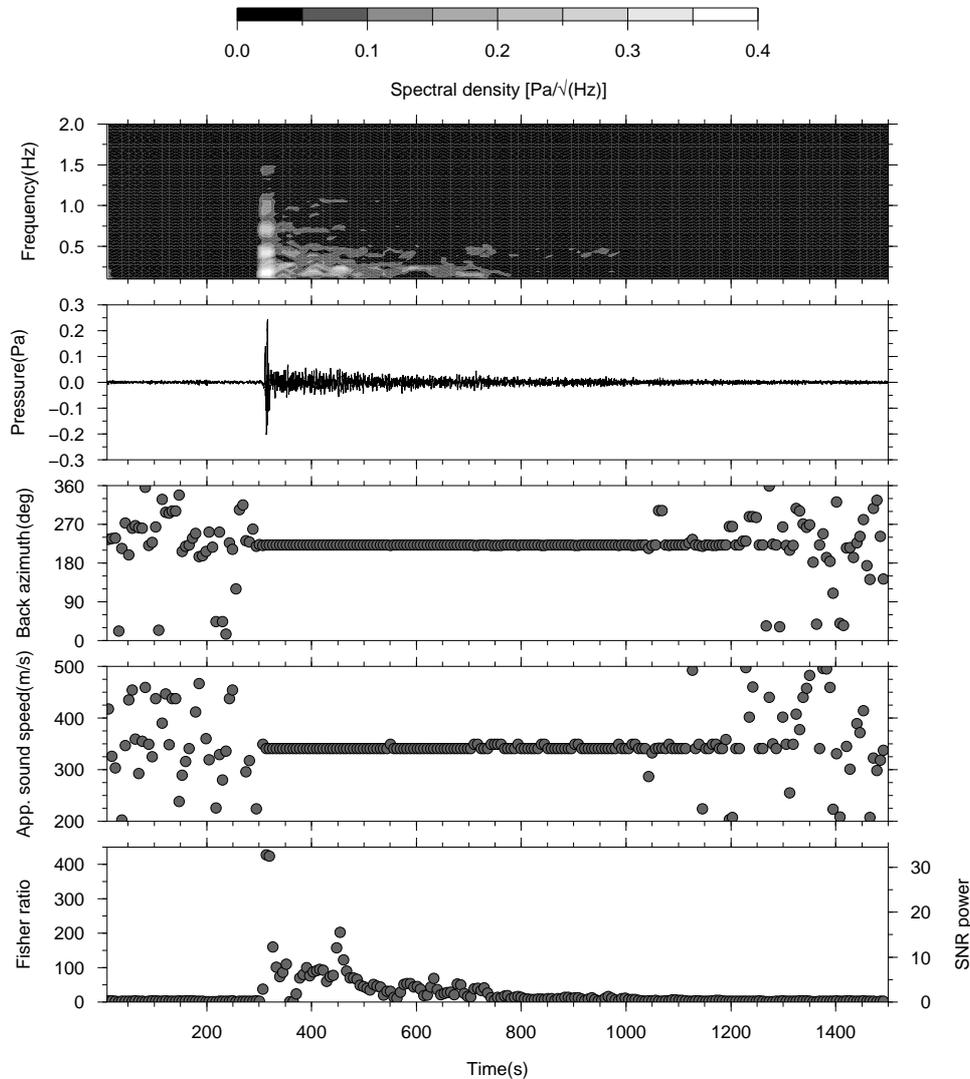
Figure 5.4: *Results of time domain Fisher ratio analysis on DIA data. The zero time of the horizontal axis is 2004, July 30 07h00m28.2s UTC. The data are filtered with a second order Butterworth filter with corner frequencies of 0.1 and 10 Hz. Beam-forming is done on a slowness grid $\vec{p}$ of 100x100 points of (p_x, p_y), forming 10,000 beams. The data are split in windows of 512 samples (12.8 s) and processed with a 50% overlap. The lower frame shows the Fisher ratio as function of time and the signal-to-noise power ratio. Apparent sound speed and back azimuth are given in the second and third frame while the best beam is shown in the fourth frame. The top frame shows the spectrogram of the best beam that peaks around 320 s and 0.2 Hz. The spectrogram is constructed with a sliding window FFT using 1024 samples with 50% overlap.*

Table 5.1: *Infrasonic stations and observations*

	DBN	DIA	Flers	Hufe	IS26
Distance(km)	183.6	208.8	378.6	453.1	737.3
True back azimuth(deg)	210.3	222.9	54.3	242.3	289.6
Arrival time (UTC)	07:04:24.5	07:05:39.0	07:15:27.1 07:17:29.9 07:18:57.6	07:23:19.2	07:43:07.0
Apparent sound speed(m/s)	354±10	346±5	343±5	328±10	336±5
Back azimuth(deg)	204.3	222.1	53.5	241.3	290.6
Dominant frequency(Hz)	0.2	0.2	0.2	0.2	0.2
Peak amplitude(Pa)	0.8	0.2	0.3	0.2	0.1
Trough amplitude(Pa)	−0.8	−0.2	−0.2	−0.3	−0.1
Duration(s)	1000	1000	1000	800	500
Average back azimuth(deg)	208.5±0.6	222.1±0.1	53.5±0.1	240.9±1.7	291.8±0.7
Celerity(km/s)	Iw: 0.34	Iw: 0.34	Is: 0.32 $IsIs$: 0.29 It: 0.27	It: 0.27	$ItIt$: 0.26

changes in the bearings. The average, called "sine loc" in Figure 5.6, is the sum of all sine-weighted intersection points divided by the sum of weights.

The atmosphere is a moving medium that causes deviations in the observations, leading to an offset between the true and observed location. This gives wave propagation an anisotropic nature, leading to a vectorial translation of the wavefront while traveling through the atmosphere.

■ 5.1.5   Infrasound propagation through the atmosphere

The sound speed is a function of wind and temperature in the atmosphere. The effective sound speed takes both temperature and wind into account by calculating
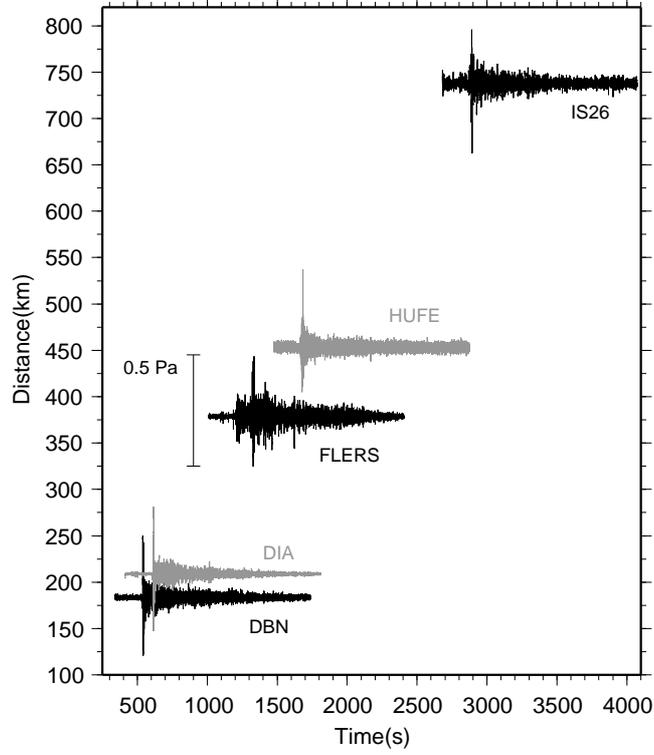
Figure 5.5: *Distance versus time graph of the infrasound data. The time axis zero time is 06u55m27.0s UTC, which is the explosion time as derived from seismic data. The maximum peak and trough amplitudes are indicated and also given in Table 5.1.*

their contributions along the propagation path, see equation 5.1.3.

$$c_{eff} = \sqrt{\gamma_g R_c T_a} + \hat{n}_{xy} \cdot \vec{u} \qquad (5.1.3)$$

where the multiplication of the ratio of specific heats with the gas constant for air is $\gamma_g R_c$=402.8 m^{2}s^{-2}K^{-1}. The absolute temperature is given by T_a, and $\hat{n}_{xy} \cdot \vec{u}$ projects the wind $\vec{u}$ in the direction from source to observer $\hat{n}_{xy}$. Atmospheric models were analyzed in order to account for their influence on the propagation of infrasound. The lower atmosphere up to an elevation of 15 km, i.e. the troposphere, is well probed because of its meteorological importance. Details on temperature and wind for the higher atmosphere are less well known. The European Center for Medium Range Weather Forecasting (ECMWF) models the atmosphere up to 65 km altitude in the stratosphere (see http://www.ecmwf.int). Models for the lower atmosphere are supported by observations from, for example, meteorological balloon measurements. Horizontal Wind Model/Mass Spectrometer and Incoherent Scatter
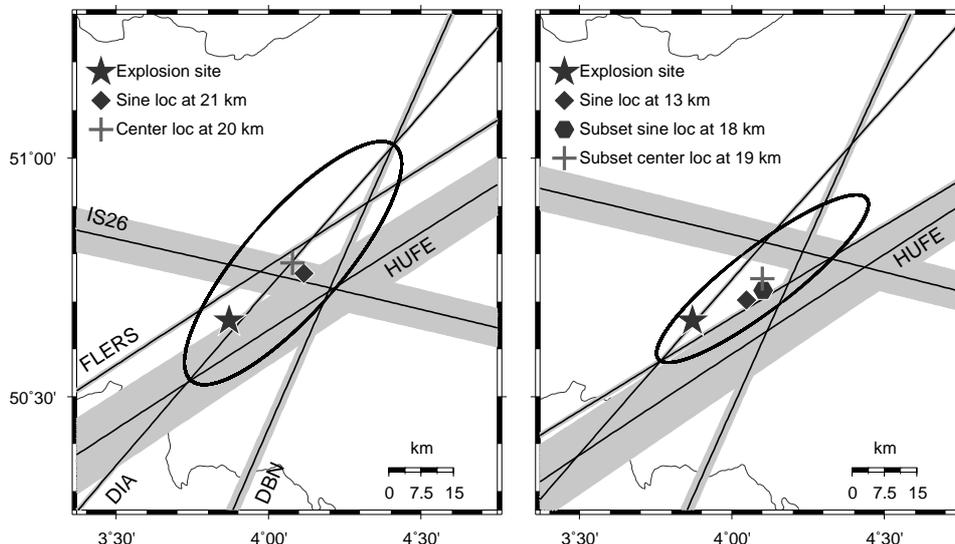
Figure 5.6: *The observed bearings from the infrasound array (left) and the wind corrected bearings (right), see table II for specific values on azimuthal deviations. The gray areas give the standard deviation in back azimuth averaged over the whole signal, see Table 5.1. The star represents the explosion site, the diamond the average location after sine weighting the cross bearings and the cross is the center of ellipse. The area of uncertainty is 1290 km^2 for raw bearings and 690 km^2 when a subset of wind corrected bearings is used, i.e. Flers, DIA and IS26. The hexagon gives the sine weighted location for the subset.*

Radar Extended Models (HWM/MSISE) [*Hedin et al.*, 1996] are used that give the climatology up to an altitude of 140 km. Depending on the atmospheric wind structure, infrasonic waves may propagate in acoustic waveguides between the ground and troposphere, stratosphere and lower thermosphere [*Brown et al.*, 2002a];[*Garcés et al.*, 2004]. Multiple arrivals, referred to as phases, may then be recorded at the receiver. They correspond to a specific family of ray paths and turning altitudes in the atmosphere and are characterized by specific values of frequency, amplitude, apparent sound speed and back azimuth along the array beam. Phases associated with waves refracted from the troposphere, referred to as Iw, are strongly dependent on local atmospheric conditions, and may not extend over very long ranges. Stratospheric phases correspond to infrasonic waves trapped between the stratopause and the ground. These phases, abbreviated as Is, are dependent on the season of the year and may fluctuate with the passing of storms and other large-scale atmospheric disturbances. They can propagate efficiently for thousands of kilometers. A phase is labeled $IsIs$ if the Is phase has experienced one bounce on the earth's surface. Thermospheric phases correspond to infrasonic waves trapped between the lower thermosphere and the ground. Considering the strong temperature gradient above

90 km, thermospheric paths, indicated as It, are always predicted. However, due to the low particle density and non-linear dissipation in the upper atmosphere, thermospheric returns are strongly attenuated and may not always be observed at large distances *Sutherland and Bass* [2004].

■ 5.1.6 Phase identification

The celerity is a useful signal characteristic to identify infrasonic phases and is defined as the epicentral distance divided by the total traveltime. Characteristic values for the celerity are: 0.23–0.28 km/s for It and 0.28–0.31 km/s for Is phases [*Brown et al.*, 2002a]. At DBN and DIA either the direct wave or Iw phase from the explosion is observed, as indicated by the celerity in Table 5.1, which equals the sound speed. The Iw phase and direct wave are hard to distinguish based on their celerity. In Figure 5.7, multiple arrivals are identified at Flers based on the celerity, apparent sound speed and frequency content.

Unambiguous phase identification can be achieved by not only taking into account the apparent sound speed but also knowledge of atmospheric winds and temperatures [*Garcés et al.*, 1998]. The Is phase is the first to arrive at Flers followed by the $IsIs$ phase. The slight but significant difference in apparent sound speed of 9 m/s (347 and 338 m/s) will be explained with raytracing later on. An It phase is identified, having the lowest frequency of 0.15 Hz of the whole trace. Further evidence for its thermospheric nature is found in the apparent sound speed of 390 m/s and the celerity of 270 m/s. At Hufe and IS26, stratospheric returns do not exist, because the increase of the effective sound speed in the stratopause is not strong enough to refract energy back to the ground. Therefore, It and $ItIt$ phases are identified at Hufe and IS26, respectively, as also follows from the derived celerities.

We applied the tau-p method as described by *Garcés et al.* [1998] to correct the observed back azimuth for the deviating effects of cross winds along the propagation path and to identify the phases at Flers further. Figure 5.8 shows an illustration of infrasound propagation from the source towards Flers both through HWM/MSISE (left) and ECMWF (right) models. Both the temperature dependent sound speed (c_t) and effective sound speed (c_{eff}) are given on the right of the lower frames. The dashed line represents the effective sound speed at the surface. Energy is refracted back to the surface from regions where c_{eff} becomes higher than the sound speed at ground level, i.e. $c_{eff,0}$. This is the case in the stratosphere and thermosphere as described earlier and as follows from the ray trajectories in the lower frames. The middle frames give the traveltime for refracted rays within the two models. The top frame shows the locations where rays impinge on the ground, if shot from the source in the direction of the receiver.

The HWM/MSISE model predicts strato- and thermospheric arrivals at Flers, where the thermospheric branch is split into two segments that represent lower and upper thermospheric refraction regions. The upper and lower branch correspond to a celerity of 0.26 and 0.29 km/s, respectively. Compared to the observed celerity of
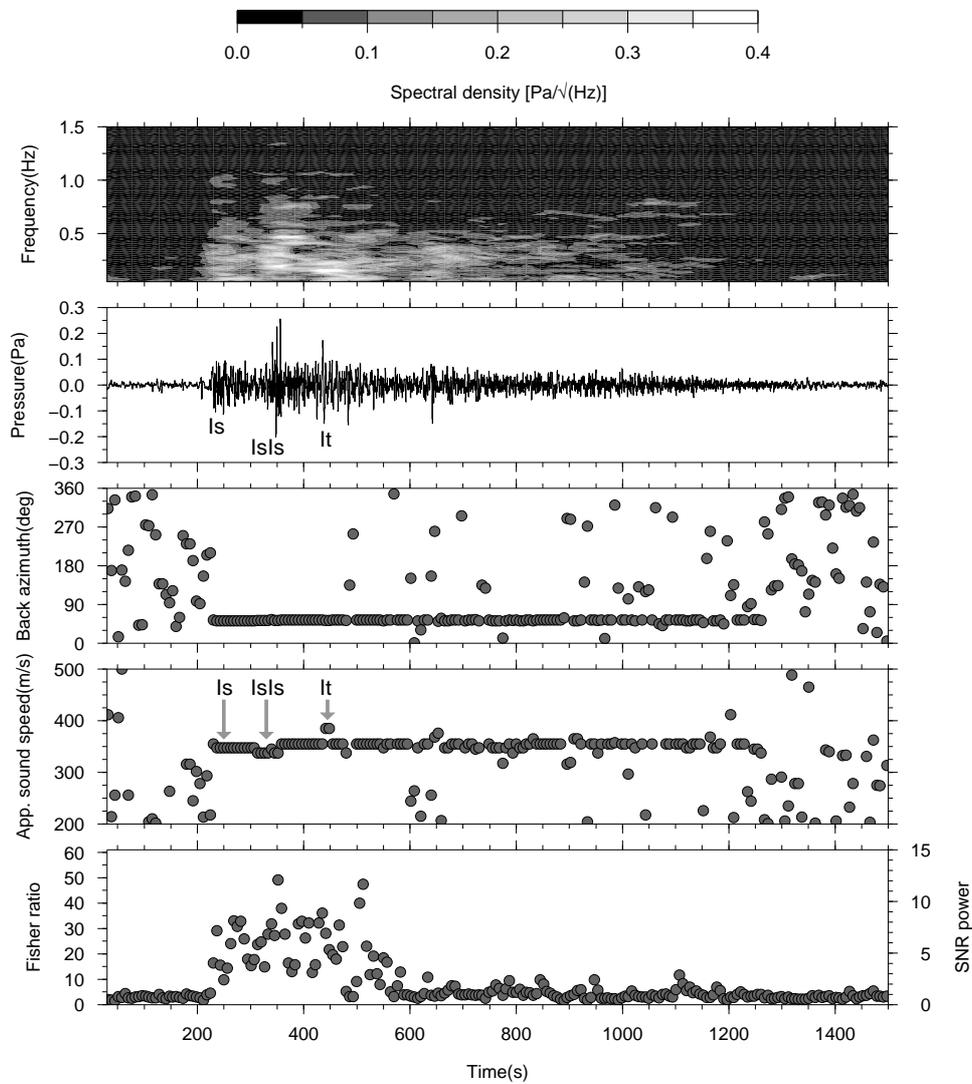
Figure 5.7: *Results of time domain Fisher ratio analysis on Flers data. The representation is similar to Figure 5.3. The zero time of the horizontal axis is 2004, July 30 07h11m40.0s GMT. The data are filtered with a second order Butterworth filter with corner frequencies of 0.05 and 1.5 Hz. The data are split in windows of 256 samples (12.8 s) and processed with a 50% overlap. Various stratospheric and thermospheric arrivals are indicated.*
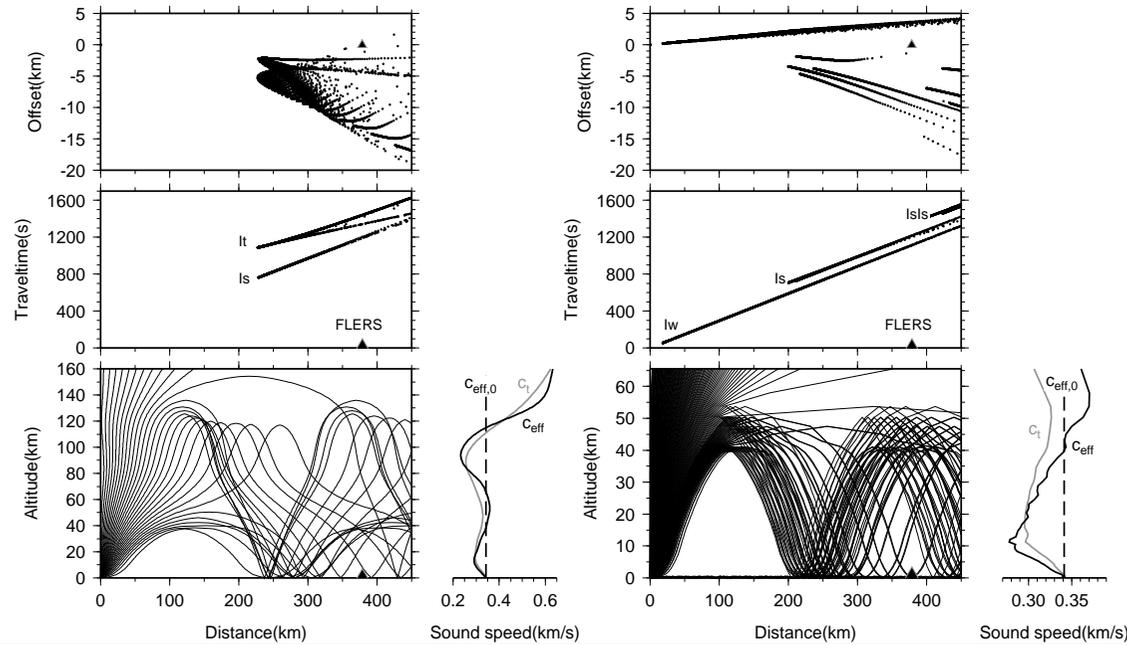
Figure 5.8: *Results from raytracing through HWM (left) and ECMWF (right) models for wind and temperature. The lower frame shows rays leaving the source in the direction of Flers. Rays bend towards the earth's surface between 40 and 55 km altitude, i.e. the stratosphere and from 120 km upwards, i.e. the thermosphere. The sound speed is plotted right of the lower frame. The effective sound speed (c_{eff} in black) accounts for both wind and temperature (c_t in gray). Refractions back to the surface occur from regions where c_{eff} becomes larger than the sound speed at the surface ($c_{eff,0}$) as indicated by the dashed line. The middle frame gives the traveltime for the rays. The upper frame shows the bounce point of the rays on the earth's surface. Rays shot from the source [0,0] to Flers [379,0] km are deviated towards the West by zonal cross winds. The azimuthal deviation follows from this representation by taking the tangent of the offset and range.*

Table 5.2: *Raytracing results*

	DBN	DIA	Flers			Hufe	IS26
Type of arrival	Iw/direct	Iw/direct	Is	$IsIs$	It	It	$ItIt$
Azimuth deviation(deg)	0.5	0.4	1.5	1.0	2.0	−0.6	0.7
Wind corrected azimuth(deg)	204.8	222.5	55.0	54.5	55.5	240.7	291.3
Traveltime(s)	535	610	1215	1355	1340	1700	2840
Celerity(km/s)	0.34	0.34	0.31	0.28	0.26	0.27	0.26

0.27 km/s, the thermospheric phase at Flers is identified as originating from the upper thermosphere. This is further supported by the higher ray density of the upper thermospheric branch. Strong westward zonal cross-winds deflect the rays towards the West of Flers, as indicated by the negative offsets in the upper frame. The ECMWF model shows the presence of a tropospheric onset due to a temperature inversion that is hardly visible in the lower frame but clear from the upper two frames and that fills up the first shadow zone with arrivals, between a distance of 0 and 200 km. An Is phase reaches Flers and an $IsIs$ phase nearly hits Flers but misses it by 20 km. This $IsIs$ phase is not predicted by the HWM/MSISE model. The $IsIs$ phase is predicted by the ECMWF model because the amplitude of the zonal wind is 10 m/s higher at 60 km altitude than in the HWM/MSISE model. Underestimating zonal winds might be expected from a climatological model such as HWM/MSISE. As the $IsIs$ phase is identified in the data we expect only the fastest $IsIs$ phase to occur at Flers. This corresponds to the phase with the lowest refraction altitude in the stratosphere of 40 km. Therefore, the difference in apparent sound speed between the Is and $IsIs$ phase of 9 m/s is explained by refraction altitudes of 40 and 50 km, respectively.

In the top frame, energy misses Flers and arrives to the West of the station because of stratospheric zonal cross winds. An azimuthal deviation of 1.5 degrees is calculated by taking the tangent of the offset and the source-receiver distance. The wind-corrected back azimuths and modeled celerities are given in Table 5.2 for all arrays, following the same approach as described above. The wind corrected back azimuths are plotted in Figure 5.6. The decrease in size of the ellipse is clearly noticeable. Here we also discarded the contribution of DBN and Hufe since the apertures of the arrays are too small to characterize correctly an event of 0.2 Hz. The main lobe of the array response is far too broad. With such an aperture precise measurements of back azimuth and apparent sound speed, or slowness, can be obtained for infrasound with a frequency 1.0 Hz and higher.

The analysis and modeling of infrasound would lead to searching of an area of 690 km² in the case of a similar explosion of unknown origin. This area is described by

the ellipse through the relevant outermost intersection points. The various distances between the true and estimated locations range from 13 to 19 km.

■ 5.1.7 Yield of the explosion

In personal communication, Fluxys reported a crater diameter of 19 to 20 m and an average depth of 4 m. A relation between crater size and yield was found from nuclear tests by [*Glasstone*, 1957]. The dataset contained depths and diameters of the craters formed by a surface explosion in dry soil with a weapon of energy or yield Y in kilotons TNT (ranging from 1 to 20,000 kilotons). The crater diameter scales according to $Y^{1/3}$ and the depth according to $Y^{1/4}$. *Kinney and Graham* [1985] described the explosive yield Y in kilograms TNT as function of the crater diameter d in meters more precisely, as:

$$d = 0.8Y^{1/3} \tag{5.1.4}$$

Equation 5.1.4 is based on data from two hundred large surface explosions An estimate of the explosive yield of the gas-pipeline is 14.5 ton TNT, using an average value of 19.5 m for the crater diameter.

An alternative approach is tested by using the high explosives (HE) dataset from Los Alamos National Laboratory. A relation between infrasonic stratospheric amplitude and yield has been derived from this dataset. The high explosive shots cover yield of 20 to 4880 tons observed at stations varying in distance from 250 to 5330 km. The total range R_t in km is scaled as shown in equation 5.1.5 with the yield Y in kilotons of high explosives.

$$R_s = \frac{R_t}{\sqrt{2 \times Y}} \tag{5.1.5}$$

Furthermore, the amplitudes of observed stratospheric arrivals are wind corrected, using the wind speed at 50 km altitude in the direction of propagation. Equation 5.1.6 shows the projection of the meridional Mw and zonal wind Zw in m/s, in the direction from source to observing station, as also used for calculating the effective sound speed.

$$V_d = -(Zw \sin \phi + Mw \cos \phi) \tag{5.1.6}$$

The observed raw amplitudes, peak-to-peak in microbars, are wind corrected with the empirical relation given in equation 5.1.7.

$$\log P_{wca} = \log P_{raw} - 0.018 V_d \tag{5.1.7}$$

The aim of the wind correction is to normalize to a zero wind condition. Thus if one is in favorable wind propagation, i.e. down wind, the normalized amplitude would be less than the observed. In the northern hemisphere summer, a source West of the receiver is favorable since the receiver is down wind of the source due to westward stratospheric zonal winds. Figure 5.9 gives the wind corrected stratospheric ampli-
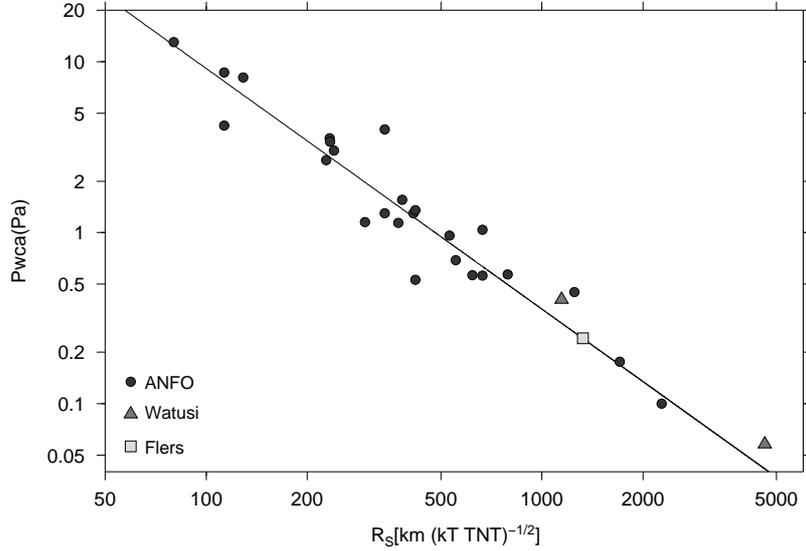
Figure 5.9: *The Watusi and ANFO data from Los Alamos National Laboratory, displayed as wind corrected peak amplitude versus scaled range. The wind corrected amplitude of Flers is fitted to the curve resolving a yield of 40.9 tons high explosives equivalent.*

tude as function of the scaled range for high explosives. The line is formed by the regression relation given as equation 5.1.8.

$$P_{wca} = 5.95 \times 10^4 (R_s)^{-1.4072} \qquad (5.1.8)$$

ANFO stands for Ammonium Nitrate Fuel Oil, a widely used explosive, data points are given by the circles. The triangles relate to the Watusi test, a high explosives experiment done at the Nevada test site in the US during 2002. Flers is the only station where clear stratospheric arrivals could be identified and is, therefore, the only station for which this empirical relation can be applied. Here, we use the regression relation in an inverse manner. Based on the observed amplitude we calculate the yield. The amplitude of 0.5 Pa, corresponding to the initial explosion, is wind corrected to 0.2 Pa with a zonal wind of -39.3 m/s (EW) and meridional wind of -6.2 m/s (NS) from ECMWF model at 50 km altitude. The wind corrected amplitude is fitted to the regression curve as shown by the square in Figure 5.9. From the scaled range a yield of 40.9 tons high explosives is calculated. The difference with the yield derived from the crater size will be discussed in the next section.

■ 5.1.8 Discussion and conclusions

The explosion of a high pressure gas-pipeline near Ghislenghien, Belgium, generated both seismic and acoustic or infrasound signals. The seismic signals, recorded at nearby seismometers, revealed an origin time of 06h55m27±2s UTC on 2004, July 30, based on the arrival times of Rayleigh waves.

Infrasound traveled over western Europe and was recorded as far as southern Germany, at a distance of 738 km. Other recording infrasound arrays were located in France and the Netherlands. Several phases were observed due to the broad epicentral coverage of infrasound arrays. These phases were identified by using their celerities, apparent sound speed and frequency contents, and by raytracing through both climatological and event-specific atmospheric models. The arrays in the Netherlands recorded direct or tropospheric refracted phases, Iw. In France both stratospheric, Is, and thermospheric, It, phases were identified. Even an $IsIs$ phase was extracted from the data corresponding to waves having one bounce against the earth's surface coming from the stratosphere. The German arrays received energy refracted in the thermosphere: the It and $ItIt$ phases.

The source location was estimated by correcting the observed back azimuths for winds and discarding less reliable small arrays. Comparing the results to the ground truth location, it was found that the source location could be confined up to a distance of 13 km leaving a search area of 690 km^2 by using wind corrected bearings. This quantifies the capability and accuracy of infrasound as monitoring technique for this specific event.

The strength of the source was determined by comparing the observed stratospheric amplitude in France to the high explosives (HE) dataset of Los Alamos National Laboratory. The HE dataset contains wind corrected stratospheric amplitudes of a wide variety of ranges and yields. A yield of 40.9 tons HE yield equivalent was derived by fitting the wind corrected amplitude from the Flers station to the regression curve of the HE dataset. Although, the yield derived from the crater size is of the same order of the magnitude, i.e. 14.5 tons TNT, the unknown source mechanisms make this value unreliable. Gas was smelt prior to explosion, therefore, the explosion might well be the result of the ignition of an area of gas saturated soil. Rather than being a confined explosion at one point, this source should be regarded as distributed over an area. To estimate the yield from the crater diameter, assuming a point source, is in this case less applicable as it is unknown how such a distributed source affects the crater volume.

In conclusion, the seismo-acoustic analysis of an explosion can reveal the origin time, location and yield of the explosion. To reach this goal accurately, infrasonic phases should be interpreted based on array processing techniques and the use of climatological and event-specific atmospheric models. The use of broad band arrays, in terms of frequency, enhances the detection and location capability for a large range of possible explosion sizes and locations.

5.2   Infrasonic forerunners: exceptionally fast acoustic phases

■ 5.2.1   Abstract

A vapor cloud explosion occurred at an oil depot near Buncefield in the UK in 2005. Three infrasound arrays in the Netherlands detected various stratospheric phases. Some of these phases appeared with celerities, i.e. the epicentral distance divided by total traveltime, in the conventional range of 0.28 to 0.31 km/s. Exceptionally fast arrivals, infrasonic forerunners, were identified with celerities of 0.31 to 0.36 km/s. These phases could be explained by head-wave-like propagation in a high velocity acoustic channel between 40 and 50 km altitude, where stratospheric zonal winds reached values of 120 m/s. The manifestation of infrasonic forerunners is validated by modeling with raytracing through actual atmospheric models and determining the celerity, apparent sound speed and back azimuth. One phase occurred with a celerity of 0.25 km/s. Hence, we propose a new celerity range for fast stratospheric phases of 0.31 to 0.36 km/s and to lower the limit of the conventional range to 0.25 km/s.

■ 5.2.2   Introduction

Large surface explosions can generate seismic and infrasound signals. The location and origin time are often known with great accuracy or can be derived from e.g. seismic data. Seismo-acoustic studies give information for forensic investigations on location, time and yield, also in the case of an unknown event. Consequently, infrasound was chosen as a verification technique for the Comprehensive Nuclear-Test-Ban Treaty [*PrepCom*, 1997]. The study of infrasound from explosions offers the opportunity to test detection algorithms, phase identifiers, localization procedures and the validity of propagation models. The results of such studies will enhance the applicability of infrasound as a monitoring technique.

A large explosion occurred at an oil depot in Buncefield, UK, on 2005, December 11. The analysis of P-waves from this massive vapor cloud explosion, revealed an origin time of 06h01m31.45s ± 0.5 s [*Ottemöller and Evers*, 2008], also no indications for secondary events were found. Infrasound from this event was detected by arrays of microbarometers in France, Germany, the Netherlands and Sweden [*Le Pichon and Ceranna*, 2006]. Propagation of infrasound over these large distances is highly influenced by stratospheric zonal winds, causing refraction of the energy. *Brown et al.* [2002a] gave a celerity range of 0.23 to 0.28 km/s for thermospheric (*It*) and 0.28 to 0.31 km/s for stratospheric phases (*Is*). Celerity is used to indicate the

quotient of epicentral distance and total traveltime. The fastest infrasonic phases are assumed to be of tropospheric origin (Iw) where direct acoustic arrivals can propagate with the sound speed, e.g. 340 m/s. Lamb waves and refractions from the jet stream may also exhibit high celerities.

In this paper, we will concentrate on modeling of stratospheric arrivals observed in the Netherlands. We have observed exceptionally fast arrivals with celerities of 0.31 to 0.36 km/s, next to regular Is phases. Fast arrivals have also been reported by *Kulichkov et al.* [2004].

■ 5.2.3   Detection and parameter estimation

Three infrasound arrays were operational in the Netherlands during the explosion. The apertures of the arrays range from 70 to 1500 m, while the number of microbarometers varies between six and 16, see Figure 5.10. Signal detection is performed by evaluating the signal coherency through the Fisher ratio [*Melton and Bailey*, 1957]. Estimates of slowness are obtained by beamforming on a 100x100 slowness grid, between -0.005 and 0.005 s/m, and are translated to apparent sound speed (c_{app}) and back azimuth (ϕ). The result of such an analysis is shown in Figure 5.11. DIA data are split in segments of 12.8 s after being band-pass filtered between 0.05 and 5 Hz. The Fisher ratio is then calculated for windows of 50% overlapping segments. Several sharp onsets trigger a detection in DIA and are associated with the explosion based on their arrival time and back azimuth. Table 5.3 summarizes the characteristics of each arrival at the infrasound arrays. The azimuthal deviation ($\Delta\phi$) is the difference between the observed and true back azimuth. The small aperture of DBN prohibits accurate estimates of c_{app} and ϕ because of the low frequency signals. Parameter estimates in EXL also suffers from its limited aperture and values for celerity are not given due to a timing problem. There is a clear trend in the data of either high c_{app} and large $\Delta\phi$ or low c_{app} and small $\Delta\phi$. Furthermore, two distinct arrivals are detected in both DBN and DIA with celerities of 0.31 km/s and 0.36 km/s. Identification of this wide variety of phases will be achieved by raytracing through actual atmospheric models. We will mainly consider the observations at DIA since this array is most suited for the low frequency signals.

■ 5.2.4   Phase identification

State-of-the-art atmospheric models have been developed at the US Naval Research Laboratory (NRL). These so-called ground-to-space (NRL-G2S) models combine actual six-hourly models from, for example, the European Centre for Medium-Range Weather Forecasts (ECMWF) with climatological models for the upper atmosphere [*Drob et al.*, 2003]. Tau-p raytracing through these models [*Garcés et al.*, 1998] is performed, to predict the type of arrivals as can be seen in Figure 5.12. The frame on the right gives the various sound speeds for 06h UTC at [52°N,3°E] deg, roughly
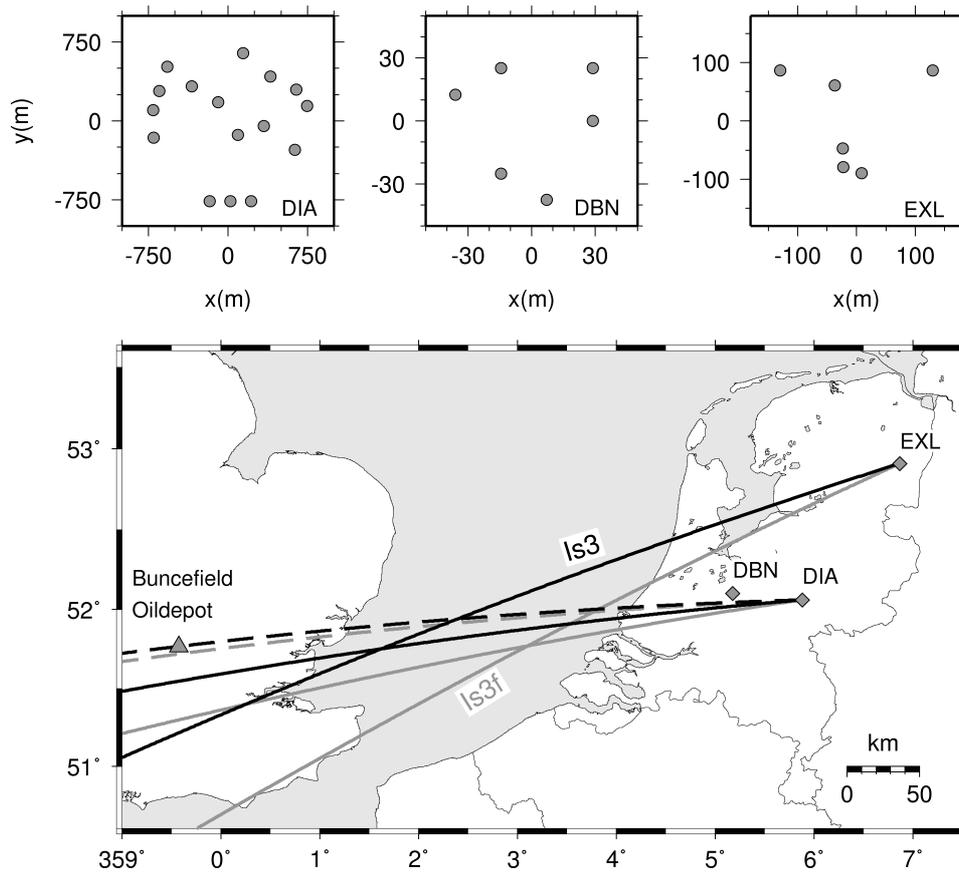
Figure 5.10: *Map showing the location of the Buncefield oil depot in the UK and infrasound arrays in the Netherlands. The array layouts are given above the map. Cross bearing results for fast, Is3f in gray, and regular, Is3 in black, dashed lines are used for wind corrected back azimuths from DIA.*
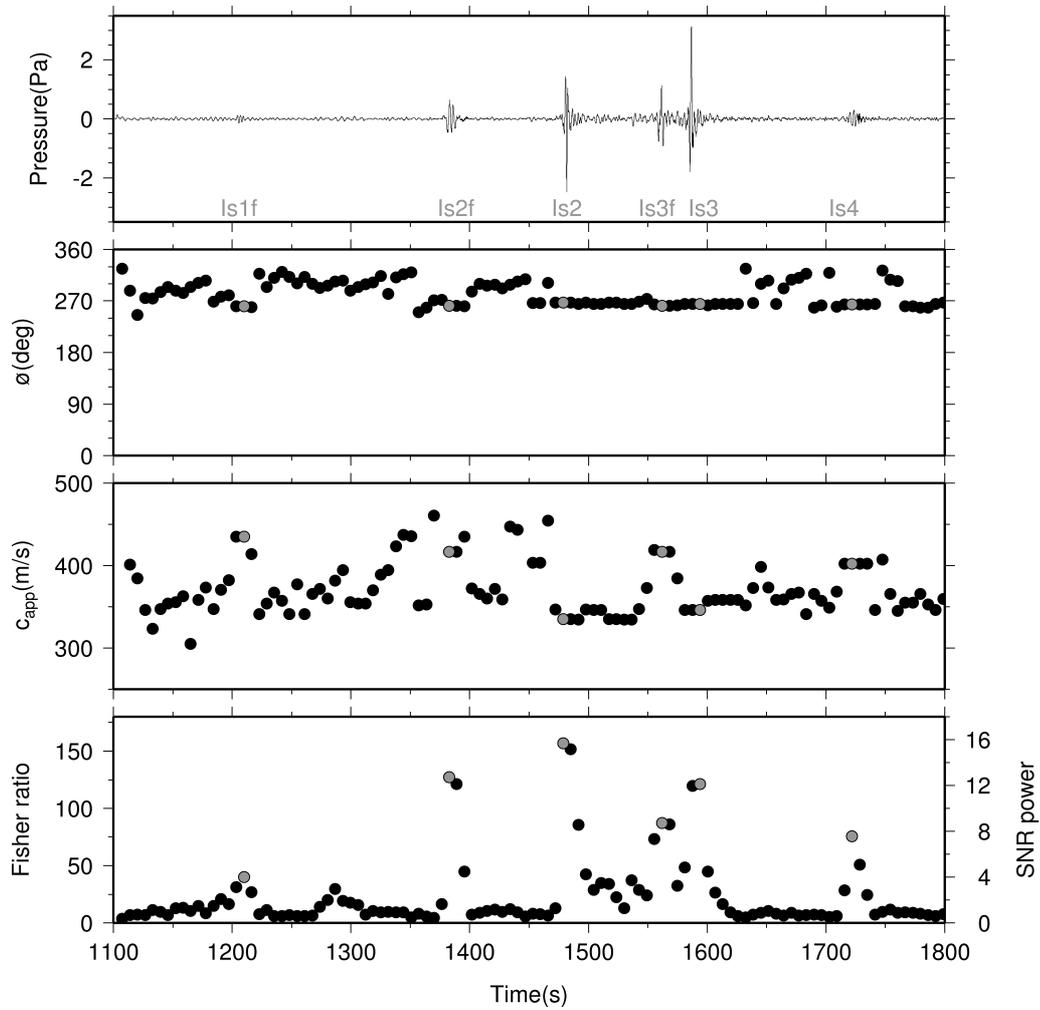
Figure 5.11: *Results of a time domain Fisher analysis on DIA data, band-pass filtered between 0.05 and 5 Hz with a second order Butterworth filter. The time axis starts 1100 s after the event time of 2005, December 11 06h01m31.45s UTC. The top frame shows the best beam for the most coherent waveform around 1480 s.*

Table 5.3: *Summary of beam forming results*

	DBN	DIA	EXL	*phase*
Distance(km)	387	435	513	
Celerity(km/s)	0.36	0.36		Is1f
	0.31	0.32		Is2f
	0.29	0.29		Is2
	0.27	0.28		Is3f
	0.27	0.28		Is3
		0.25		Is4
Frequency(Hz)	0.4	0.4		Is1f
	0.5	0.3		Is2f
	0.5	0.5		Is2
	0.4	0.5	0.4	Is3f
	0.2	0.4	0.3	Is3
		0.5	0.3	Is4
Amplitude(Pa)	0.6	0.5		Is1f
	3.1	1.6		Is2f
	17.5	3.9		Is2
	6.0	3.1	2.9	Is3f
	7.5	5.1	7.6	Is3
		0.8	10.3	Is4
c_{app}(m/s)		435		Is1f
		417		Is2f
		335		Is2
		417	438	Is3f
		346	356	Is3
		402	396	Is4
$\Delta\phi$(deg)		−7.0		Is1f
		−6.7		Is2f
		−1.1		Is2
		−6.7	−13.4	Is3f
		−3.2	−6.3	Is3
		−4.0	−8.4	Is4
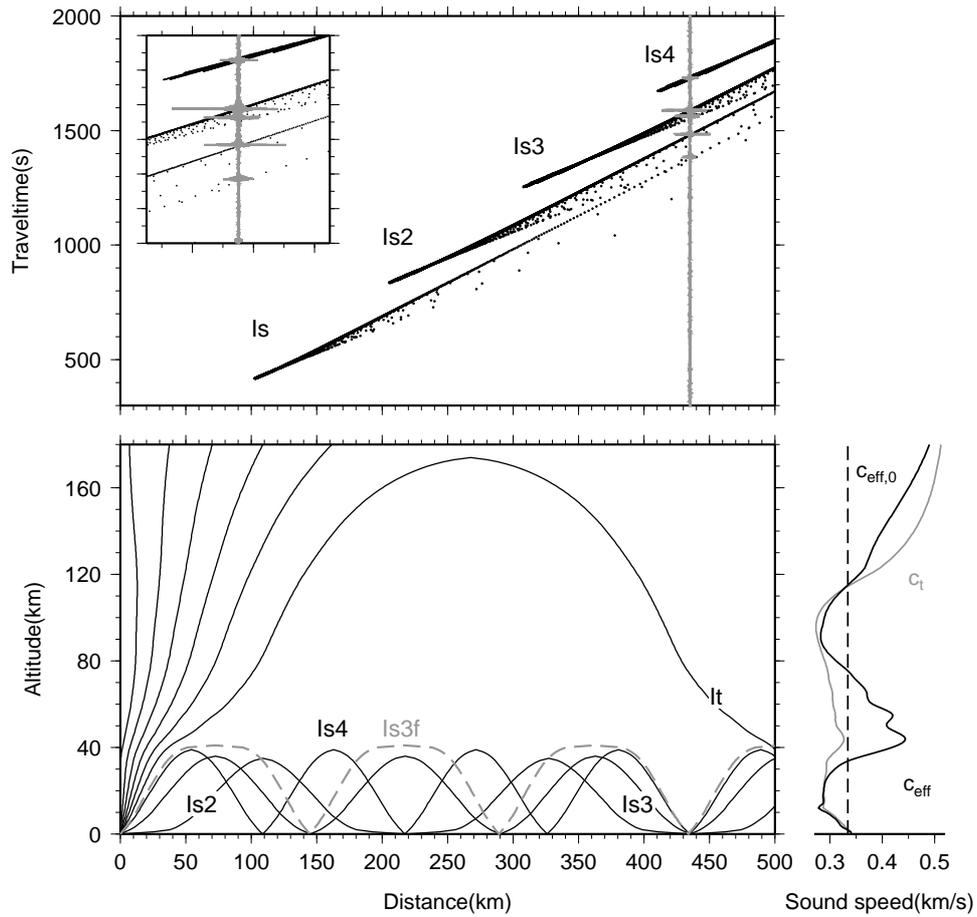
Figure 5.12: *Raytracing results for energy traveling from the source to DIA. The sound speed (c_t), effective sound speed (c_{eff}) and surface sound speed ($c_{eff,0}$) are given in the right frame. The top frame shows the traveltimes, the inlay zooms in on arrivals at DIA.*

halfway between Buncefield and DIA. Shown are the temperature dependent (c_t), effective sound speed (c_{eff}) and the sound speed at the surface ($c_{eff,0}$). c_{eff} takes into account both the effect of wind and temperature. The temperature increase in the ozone layer is not enough to lead to refractions back to the surface of infrasound since c_t is smaller than $c_{eff,0}$. A strong zonal stratospheric wind, i.e. 120 m/s, leads to a large increase in c_{eff} around 40 km altitude. These winds are directed eastwards during the northern hemisphere winter and lead to efficient ducting of the energy. Thermospheric phases, It, are always predicted but have a large shadow zone due to the strong stratospheric wind and suffer from strong attenuation in the rarefied upper atmosphere [*Sutherland and Bass*, 2004]. At DIA several Is phases are observed when comparing the modeled and observed traveltimes. $Is2$ refers to the phase that experienced one reflection on the earth's surface, $Is3$ to two reflections and so on (Figure 5.11 and 5.12). It follows from raytracing that at least $Is2$ up to $Is4$ can be identified. The early pronounced arrival might be associated to a forerunner of $Is2$, being $Is2f$. Furthermore, the $Is3$ phase appears also to be split in two distinct arrivals: an $Is3f$ and a regular one. The observations of the different arrays are labeled in Table 5.3. It should be noted that the waveform of $Is1f$ is not visible in the type of representation chosen in Figure 5.12.

Some of the amplitude variations can also be understood considering these results. DIA is at 435 km just capable of receiving $Is4$ while EXL at 513 km is at a more favorable range. The amplitude of $Is4$ is, therefore, much larger at EXL. The same considerations hold for $Is2$ at DBN and DIA, where DBN is situated in a better position. The arrays seem equally sensitive to the $Is3$ phase. It also follows from Table 5.3 that the forerunners, $Is2f$ and $Is3f$, have a high c_{app} and large $\Delta\phi$. These observations and the occurrence of an even faster phase, labeled as $Is1f$, will be examined in more detail.

■ 5.2.5   Evidence for infrasonic forerunners

What kind of propagation paths do and which do not allow phases to travel with a celerity of 0.36 km/s? These are certainly not tropospheric phases since the highest c_{eff} is 0.34 km/s (Figure 5.12). Further proof for non-tropospheric propagation is found in the high propagation velocity between DBN and DIA of the various phases. These are 0.42 km/s for $Is1f$ and $Is2f$ and 0.41 km/s for $Is3f$. The cross-bearing results in Figure 5.10 show a source location off the coast of the Netherlands for $Is3f$. Although, care should be taken with the unreliable back azimuths from EXL because of its limited aperture. The observed bearings should be corrected for the deviating effects of zonal cross-winds. Doing so, the cross-bearing location will move towards Buncefield because of the eastward directed stratospheric wind. A strong wind continuously affecting the wavefront orientation is needed to explain this unusual large $\Delta\phi$ for the fast phases. The stratosphere is the area where strong winds occur that may lead to high celerity and large $\Delta\phi$. Exceptionally fast arrivals will be observed, especially, when the energy is caught in the stratosphere. Steep angles
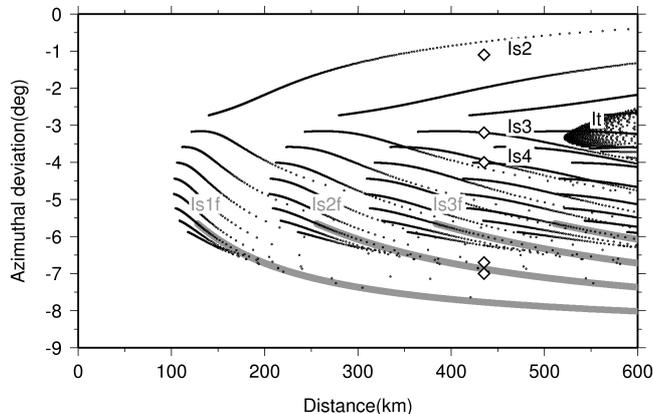
Figure 5.13: *Modeled and observed azimuthal deviations as diamonds, regular phases are given in black while infrasonic forerunners are shown in gray for DIA.*

of incidence at the surface, i.e. high c_{app}, will results from this kind of propagation. The propagation paths have similar characteristics to those of head waves known from seismology. Head waves follow from Snell's law that predicts critical refraction. A head wave will travel horizontally along the interface of a velocity contrast, continuously transmitting energy back into the layer it originates from (see the example of $Is3f$ in Figure 5.12). This gives rise to a strong decrease in amplitude with distance. *Kulichkov et al.* [2004] could explain observed waveforms and arrival times for anomalously fast phases by the pseudo-differential parabolic equation method. Here we will now concentrate on $\Delta\phi$, the celerity and c_{app}.

Figure 5.13 shows the modeled azimuthal deviations for DIA. The modeled values for the forerunners were obtained by shooting rays with a launch angle of 54 to 55 deg from the source (0 deg means vertical departure) to DIA. Values of $\Delta\phi$ are calculated by taking the tangent of the modeled southeastern offset, induced by stratospheric winds, with distance. The rays travel almost horizontally at an altitude of 41 km for energy that leaves the source in this narrow range of angles from 54 to 55 deg. The largest azimuthal deviations, in gray, are for $Is1f$, followed by $Is2f$ and $Is3f$. The longer the energy has been trapped in the stratosphere, the higher the azimuthal deviation will be. These results indicate that the unusually large azimuthal deviations can be explained. Azimuthal deviations in EXL will even be larger because its bearing has a larger northward component. Therefore, these deviations are more affected by cross-wind than DIA's deviations. In Figure 5.10, wind corrected back azimuths for DIA are plotted as dashed lines, showing agreement with the source location.

The corresponding traveltimes are given in Figure 5.14. There is good agreement between modeled and observed traveltimes. The traveltime residuals vary from 0.6
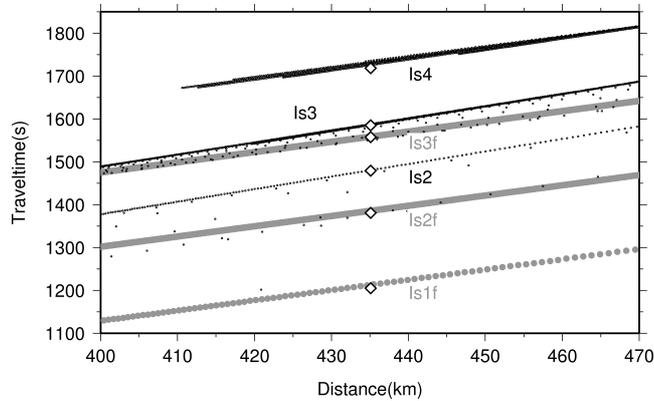
Figure 5.14: *Modeled traveltimes for regular phases (black) and forerunners (gray). The observed traveltimes are denoted by the diamonds.*
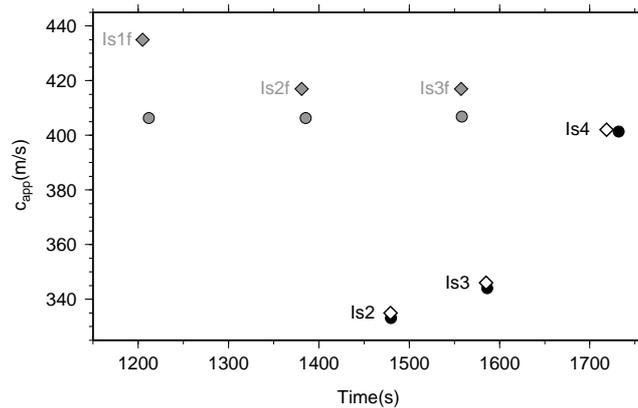
Figure 5.15: *Modeled (circles) and observed (diamonds) apparent velocities. Results for the forerunners are given in gray, regular phases are shown in black.*

s for $Is3$ to 11.6 s for $Is4$. The average residual for the three forerunners equals 4.3 s.

Apparent velocities are modeled by evaluating the inclination of the rays (Figure 2.8) The surface sound speed used for the calculation in DIA was 332.8 m/s, corresponding to a temperature of 2.4 °C. Figure 5.15 gives the results for the observed and modeled phases as a function of time. Head-wave like propagation results in a constant c_{app} for the forerunners. High c_{app} values are obtained for energy captured in the stratosphere, although, there is some disagreement between the modeled and

observed values. The differences are regarded as small in view of the highly dynamic and anisotropic nature of the atmosphere. The increase in c_{app} with time, for the regular phases, is well modeled as are the absolute values.

■ 5.2.6 Discussion and conclusion

At DIA the fastest phase, $Is1f$, arrived with an azimuthal deviation of 7 deg, 275 s before a usual phase, $Is2$. At first sight, the forerunners might also be interpreted as regular phases from another event. However, we have been able to explain the large $\Delta\phi$, short traveltime and high c_{app}, identifying the phases as coming from the same explosion. Additional evidence comes from the non-tropospheric effective velocity of 414 to 420 m/s, for the forerunners between DBN and DIA, in agreement with the effective velocity around 40 km altitude. Furthermore, the average frequency contents of the correlative impulsive signals is 0.4 ± 0.09 Hz, making a similar source being active at the same time unlikely.

In this study, we have shown that infrasound can travel with celerities up to 0.36 km/s. The resulting forerunners were guided by a high velocity layer in the stratosphere, where zonal winds reached 120 m/s. Therefore, we propose to modify the conventional celerity range for Is phases, being 0.28–0.31 km/s, to 0.25–0.31 km/s for $Is4$ to $Is1$. Furthermore, we found a new celerity range for fast stratospheric phases, i.e. Isf, of 0.31 to 0.36 km/s. The lower limit is now well into the It range, while the upper limit also covers Iw phases, making phase identification ambiguous if performed only on the basis of celerity.

6

Conclusions and outlook

6.1 Conclusions

■ 6.1.1 Introduction

In this thesis techniques have been presented for the measurement, processing and interpretation of infrasound data. The acquisition of infrasound data is realized with arrays of microbarometers to reduce noise. Furthermore, array processing techniques are applied to detect coherent signals in the continuous recordings and estimate characteristic event parameters. Signals are detected by using a statistical test on the basis of the Fisher ratio. The signal's back azimuth and apparent sound speed are resolved through beamforming. Sources of infrasound have been identified ranging from natural events, like meteors and volcanoes, to man-made events, like accidental chemical explosions. Knowledge on the atmosphere appeared to be essential in understanding the atmospheric propagation of infrasound.

■ 6.1.2 Conclusions from Chapter 2 on acquisition and processing

In Chapter 2 the construction and operational principles of a differential microbarometer were explained. The KNMI microbarometer which was developed is capable of measuring infrasound in the frequency range of 0.002 up to at least 20 Hz. The amplitude response is flat in this interval. The low frequency cut-off of the microbarometer is controlled by a high acoustic resistance. This was realized with a thin capillary mounted in the backing volume that redirects air pressure fluctuations with too long periods, i.e. longer than 500 s, back to the atmosphere. Air pressure

fluctuations can be sensed in the range from 10^{-2} to 10^2 Pa with a sensitivity of 5.65×10^{-2} Pa/mV.

Five infrasound arrays have been designed, based on the array response which was derived theoretically in Chapter 2. Ideally, the response is a delta function centered around the frequency and wavenumber, or slowness, of interest. In this case, spatial sampling is infinite and the wavefield can be fully reconstructed. Both spatial and temporal sampling are limited in practical applications and this discretization leads to aliasing. Optimal sparse arrays have been designed by optimizing the number of inter-array element distances and array aperture for a limited number of sensors. An example of such an array is a six element configuration in the form of a pentagon with one central element.

Continuous array recordings of infrasound have become available through the internet. A signal detector has been derived in Chapter 2 for the extraction of coherent events out of these data streams. A statistical test is evaluated with a null hypothesis stating that all recordings consist of noise. The alternative hypothesis becomes true if signal is present. The corresponding Fisher ratio is one if the null hypothesis is not rejected, e.g. accepted, and will be biased positively in case signal is present and the null hypothesis is rejected. Beamforming is applied by time shifting the recordings; the F-ratio is evaluated for each beam. At the maximum F-ratio, the signal characteristics are derived which are back azimuth and apparent sound speed.

■ 6.1.3   Conclusions from Chapter 3 on meteors

The developed measurement technique and array processing algorithms have been utilized in Chapter 3. The detection and identification of meteors is of crucial importance to the verification of the Comprehensive Nuclear-Test-Ban Treaty (CTBT). Meteors are one the few natural sources mimicking a nuclear test with energies in the kT TNT range. The high sensitivity of the Deelen Infrasound Array (DIA) was proved by the simultaneous detection of a meteor, on 1999, November 8, and infrasound from the non-linear interaction of oceanic waves, called microbaroms. The difference in frequency of these phenomena was 0.04 Hz where the F-ratio enabled a clear detection of both. The energy release of the exploding meteor of 1.5 kT TNT is in the range of nuclear explosions and probably occurred at a distance of 320 km from DIA and altitude of 15 km. The microbaroms found their origin South of Iceland as derived from ocean wave amplitude and frequency data. Since microbarom activity is very common, careful processing is necessary in identifying small-sized nuclear tests.

A meteoroid is a moving object in the atmosphere, while an atmospheric nuclear test can be considered as a point source located on the earth's surface. Chapter 3 continues with exploiting this characteristic in distinguishing between a meteor and a nuclear test. Infrasound from a meteor was detected at two arrays in the Netherlands on 2003, February 19. Two separate impulsive events were measured by each

array and appeared to come from different directions. The differential traveltimes of these phases were used to locate the origin of the energy in the atmosphere. Appropriate propagation models are necessary as input for this exercise. Raytracing was performed by using both actual and climatological models for the wind and temperature. The energy was located in the stratosphere at 30 and 57 km altitude. The calculated traveltimes confirmed the origin time from visual observations. The results strongly depend on the accuracy of the atmospheric models. In this case, actual or event-specific atmospheric models from the European Centre for Medium-Range Weather Forecasts (ECMWF) could best explain the observations. It was concluded that moving sources in the atmosphere can successfully be identified with infrasound.

■ 6.1.4   Conclusions from Chapter 4 on Mt. Etna

Chapter 4 describes the detection of infrasound from the eruptions of Mt. Etna, on Sicily in Italy, in the Netherlands by DIA during 2001, July 28 and 29. This far-field infrasound was well detected at night when the atmosphere stabilizes due to lack of solar heat fluxes. During daytime, solar radiation induces turbulent structures which lead to decorrelation of the infrasonic signals in the boundary layer. The energy reached altitudes of 130 km and was affected by zonal cross winds. Deviations in back azimuth up to 2.6 degrees could be explained by stratospheric westward winds of 50 m/s at 60 km altitude. The signals have low signal-to-noise power ratios; one of the most coherent waveforms has a signal-to-noise power ratio of 0.6. The detection capability of sub-arrays of DIA has been assessed by lowering the number of active elements from 13 to three for small, 800 m, and large, 1400 m, aperture sub-arrays. Doing so, sparse arrays as used for the verification of the CTBT were mimicked. The two main findings were: small aperture sub-arrays perform much better than large aperture sub arrays, due to the loss of spatial coherency, and the number of detections strongly increases with the number of elements. With a reduction in size of the array with a factor of two, two instruments less can be used to obtain the same number of detections. This also indicates the loss of spatial coherency in the boundary layer.

■ 6.1.5   Conclusions from Chapter 5 on explosions

Seismic and infrasonic signals resulting from accidental chemical explosions are analyzed in Chapter 5. A high pressure gas-pipeline exploded near Ghislenghien in Belgium, on 2004, July 30. Seismic energy of this event was recorded at three nearby seismometers, resolving an origin time of 06h55m27±2 s UTC. Infrasound was recorded in France, Germany and the Netherlands. Several phases were observed due to the broad epicentral coverage of infrasound arrays. These phases were

identified by using their celerities, apparent sound speed and frequency contents, and by raytracing through both climatological and event-specific atmospheric models. The arrays in the Netherlands recorded direct or tropospheric refracted phases, Iw. In France both stratospheric, Is and $IsIs$, and thermospheric, It, phases were identified. The German arrays received energy refracted in the thermosphere: the It and $ItIt$ phases. The source location was estimated by correcting the observed back azimuths for winds and discarding less reliable results from small arrays. Comparing the results to the ground truth location, it was found that the source location could be confined up to a distance of 13 km within a total area of 690 km^2 by using wind corrected bearings. The strength of the source was determined by comparing the observed stratospheric amplitude in France to the high explosives (HE) dataset of Los Alamos National Laboratory. A yield of 40.9 tons HE yield equivalent was derived by fitting the wind corrected amplitude from the French Flers station to the regression curve of the HE dataset.

A vapor cloud explosion occurred at an oil depot near Buncefield in the UK on 2005, December 11. Infrasound from this explosion was also discussed in Chapter 5. Three infrasound arrays in the Netherlands detected various stratospheric phases. Some of these phases appeared with celerities in the conventional range of 0.28 to 0.31 km/s. Exceptionally fast arrivals were identified with celerities of 0.31 to 0.36 km/s. The resulting infrasonic forerunners were guided by a high velocity layer in the stratosphere, where zonal winds reached 120 m/s. Propagation within this layer also explained the large deviations in back azimuth of at least 7 degrees and the high apparent velocities of 435 m/s.

6.2   Outlook

■ 6.2.1   Introduction

Infrasound is generated by a wide variety of natural and man-made sources, as discussed in this thesis. The recorded waveforms are a convolution of the source function, the influence of the atmosphere and the response of the measurement system. Therefore, continuous infrasonic recordings contain information on the spatial and temporal variations in the atmosphere, up to thermospheric altitudes. Section 6.2.2 describes the possible future usage of infrasound as passive atmospheric probe in acoustic remote sensing.

The measurement and processing techniques described in this thesis can also be applied to phenomena traveling with sub-acoustic velocities. Examples of such waves are: gravity waves and solitary waves. Section 6.2.3 describes the observation of a density current traveling with a sub-acoustic velocity. Monitoring of gravity waves is of interest for climatological studies.
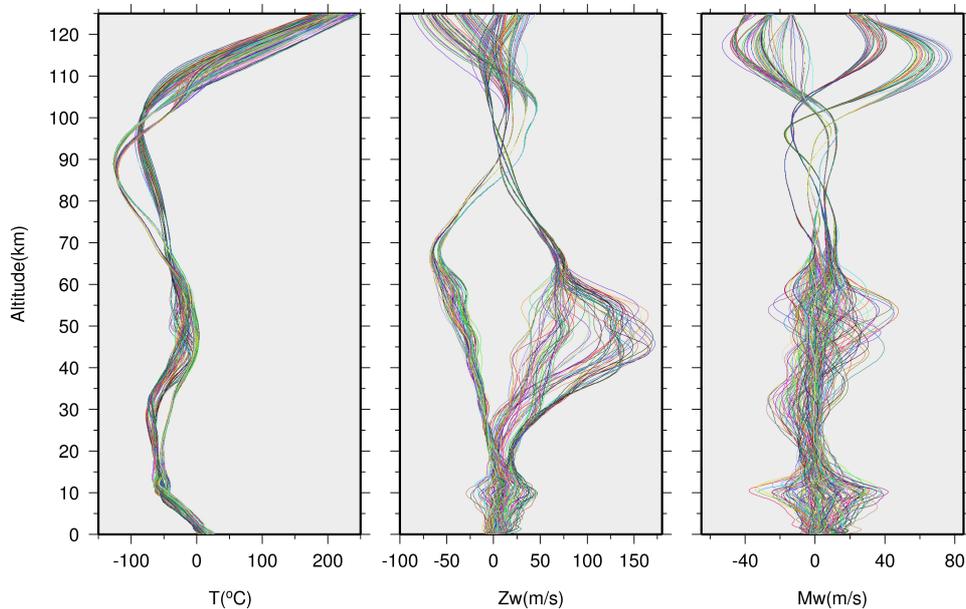
Figure 6.1: *NRL-G2S temperature and wind profiles for De Bilt, the Netherlands, at $52°N$, $5°E$ [Drob et al., 2003]. The wind is split in a zonal (Zw) and meridional (Mw) component. The zonal wind has a positive sign when directed from West to East, i.e a westerly wind, the meridional is positive when directed from the South. Shown are four profiles a day (at 00, 06, 12 and 18 UTC) for five days in summer and winter. The period spans the years 2003 through 2006 on day July 01–05 and December 01–05, adding up to a total of 160 profiles per parameter.*

■ 6.2.2 Acoustic remote sensing

The propagation of infrasound is controlled by the wind and temperature structure of the atmosphere. Consequently, infrasound contains information on these atmospheric properties. For example, the state of the stratosphere can be identified in azimuthal deviations and propagation velocity as was seen in Chapter 4 and 5. The troposphere is well probed with a variety of ground and space based sensors because of its meteorological importance. Knowledge degrades rapidly as function of altitude and models become the preferred source of information. ECMWF currently models the atmosphere up to an altitude of roughly 85 km. Climatological models are the main source of information for the upper atmosphere, i.e. 85 km and upwards.

Infrasound has the unique property of passively probing the atmosphere up to thermospheric altitudes. A large variety of sources continuously transmit infrasound, e.g. oceanic waves and volcanoes, and can be used to validate atmospheric models. An example of a set of models is shown in Figure 6.1. These models are valid for

De Bilt, the Netherlands, at 52°N, 5°E, four times a day for five days in winter and summer from the years 2003 through 2006. Figure 1.3 showed the signature of infrasonic phases on the earth's surface on 2006, July 01 at 12 UTC. This intriguing picture is the result of one of the 160 realizations of the atmosphere as shown in Figure 6.1.

The variability in the whole atmosphere can be imaged with infrasound by using for example traveltime inversion in a tomographic approach. Information can be retrieved on a wide variety of spatial scales, depending on the source-receiver distance [*Antier et al.*, 2007]. The temporal resolution may vary from hourly to seasonally fluctuations. Ambient noise can be used in an interferometric application [*Godin*, 2006] to increase the spatial coverage and temporal resolution.

Obtaining detailed information about the whole atmosphere, i.e. up to thermospheric altitudes, is of interest for the following two subjects:

- Atmospheric models can be validated or improved with infrasound which will result in factual instead of climatological information. Accurate knowledge on the wind and temperature structure will lead to more precise results, like location, time and yield, when infrasound is used as verification techniques. Currently, errors are determined by uncertainties in the atmospheric models and propagation.

- The troposphere has long been considered an isolated layer responsible for weather and climate. Evidence is emerging that the tropopause is not an impermeable layer and processes in the stratosphere have influence in the troposphere on seasonal and decadal timescales [*Shaw and Shepherd*, 2008].

An example is a Sudden Stratospheric Warming (SSW) which is an event in the stratosphere that can be monitored with infrasound. A SSW is an increase in temperature, in the stratosphere, of tens of degrees Celsius within a couple of days during the northern hemisphere winter. Simultaneously, the polar vortex slows down and sometimes reverses direction [*Holton*, 1979]. The dramatic change in wind and temperature is notable in the infrasonic amplitudes of microbaroms [*Rind and Donn*, 1978] or disappearance of the stratospheric duct [*Evers and Haak*, 2005]. SSWs of variable size and intensity occur each winter in the northern hemisphere. Their impact on the weather and climate are currently being studied.

■ 6.2.3   Detection of non-acoustic phenomena

If the wavelength of infrasound becomes too large, gravity starts acting on the mass displacement. Gravity becomes the preferred restoring force above molecular vibration. Acoustic waves first become acoustic-gravity waves and as the wavelengths increase, gravity waves start occurring [*Gossard and Hooke*, 1975]. The amplitude of gravity waves is larger, i.e. tens of Pa, than the amplitude of acoustic waves
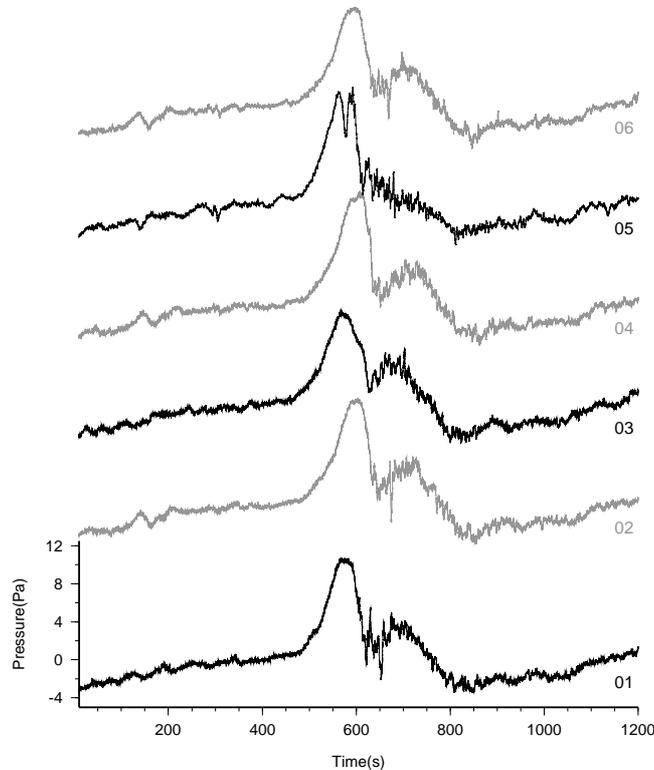
Figure 6.2: *Unfiltered recordings from the EXL infrasound array on 2007, February 05, with a time axis starting at 15h43m43.82s UTC. The low frequency event, peaking around 550 s, is a density current.*

described in this thesis. Furthermore, the propagation velocity is in the order of 10 m/s which is much lower that the sound speed.

Detection of gravity waves is of interest because of their destabilizing effect on the boundary layer. Uncertainties in the representation of the atmospheric stable boundary layer (SBL) in climate models contribute to uncertainties in climate prediction. Turbulence is the dominating mechanism for transport in the weakly stable boundary layer. When the SBL becomes more stable, turbulence is suppressed and other phenomena like low level jets, radiation and gravity waves may become important. With infrasound, gravity waves can be distinguished from turbulence and other disturbing influences based on the coherency length of the features (Dr. F. Bosveld (KNMI), personal communication).

Figure 6.2 shows low frequency signals traveling over the Exloo Infrasound Array (EXL) followed by a tail of more high frequency pressure fluctuations. This event was
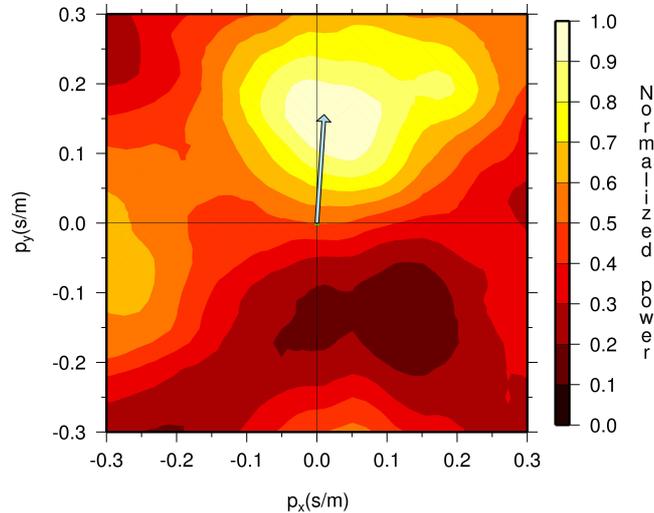
Figure 6.3: *Broad-band frequency slowness analysis between 0.01 and 0.1 Hz. A time segment of 409.6, 16384 samples at a sample rate of 40 Hz, is chosen starting at 400 s. Resolved are a back azimuth of 3.8 deg and an apparent sound speed of 6.6 m/s, corresponding to a p_x and p_y of 1.01×10^{-2} and 0.15 s/m.*

explained by Dr. D.R. Christie, Research School of Earth Sciences - The Australian National University, in personal communication. Following Dr. D.R. Christie, the event is a density current (or gravity current) followed by oscillations corresponding to density-current induced turbulence. Density currents that propagate into a stable layer may slowly evolve into a family of solitary waves. Solitary waves are described in *Christie et al.* [1978], *Christie* [1989] and *Christie* [1992].

Gravity waves and solitary waves can conveniently be measured with arrays of microbarometers. Parameter estimation of back azimuth and apparent velocity can be achieved with the infrasound arrays described in this thesis. Although, the periods of the waves is much longer, their propagation velocity are much lower than infrasound. Consequently, traveltime or phase differences can still be used to get an accurate estimate of the slowness. Figure 6.3 shows the result of a broad-band frequency slowness analysis of the density current. The slowness range of interest is enlarged to sub-acoustic velocities. The density current traveled with an apparent sound speed of 6.6 m/s and came from the North with a back azimuth of 3.8 deg.

A

List of symbols and abbreviations

A.1 Symbols

The symbols used in this thesis are alphabetically listed.

Symbol	unit	explanation
α_t	Pa	Signal amplitude at time t
$A_j(\omega)$	Pa	Fourier amplitude from jth instrument at ω
a	m	Radius of capillary
a_w	m	Amplitude of oceanic waves
b	$\mathrm{m}^3\ \mathrm{Pa}^{-1}$	Volume change
$C(g,h)$		Correlation of signals $g(t)$ and $h(t)$
c_{app}	$\mathrm{m}\ \mathrm{s}^{-1}$	Apparent sound speed
c_{eff}	$\mathrm{m}\ \mathrm{s}^{-1}$	Effective sound speed
Δ	s	Sample rate
$\delta()$		Delta function
D		Microbarometer response
d	m	Crater diameter
ϵ_{nt}	Pa	Noise amplitude at instrument n on time t
η	$\mathrm{Pa}\ \mathrm{s}^{-1}$	Viscosity of air
$E(V)$		Expected value of variation V

Symbol	unit	explanation
F		Time domain Fisher ratio
$F(\omega, \vec{k})$		Frequency domain Fisher ratio
f_N	Hz	Nyquist frequency
f_l	Hz	Low frequency cut-off microbarometer
f	Hz	Frequency
γ_g		Ratio of specific heats
$G(f, \vec{r})$	Pa s$^{-1/2}$	Fourier transform of $g(t, \vec{r})$
g	m s^{-2}	Gravitational constant
$g(t, \vec{r})$	Pa	Wavefield at time t and position $\vec{r}$
h	m	Altitude
$\vec{k}$	m^{-1}	Wavenumber vector (k_x, k_y, k_z)
l	m	Length of capillary
Mw	m/s	Meridional wind
N		Number of microbarometers $n = 1, ..., N$
$\hat{n}$		Vector normal to the wavefront
$\hat{n}_{xy}$		Projection of the normal vector on the xy-plane
ω	rad s^{-1}	Angular frequency
ΔP	Pa	Pressure difference
ϕ	degrees	Back azimuth clockwise from the North
$\varphi_j(\omega)$	rad	Fourier phase from jth instrument at ω
P	Pa	Pressure
P_A	Pa	Ambient pressure
$P_S(\omega, \vec{k})$	Pa^2 s	Signal power
$P_T(\omega)$	Pa^2 s	Total power in recordings
P_e	Pa	External pressure
P_{raw}	Pa	Non-wind corrected amplitude
P_t	Pa	Time indexed pressure
P_{wca}	Pa	Wind corrected amplitude
$P(\omega, \vec{k})$	Pa^2 s	Frequency-wavenumber power spectrum
p	Pa	Pressure in backing volume
$\vec{p}$	s m^{-1}	Slowness vector (p_x, p_y)
ρ	kg m^{-3}	Density
R	kg m^{-4}s^{-1}	Low acoustical resistance of inlet
R_t	km	Total range
R_s	km (kT TNT)$^{-1/2}$	Scaled range
R_c	J mol^{-1}K^{-1}	Universal gas constant
$R(\omega, \vec{p})$		Array response

Symbol	unit	explanation
r	kg m^{-4}s^{-1}	High acoustical resistance of capillary
$\vec{r}$	m	Three dimensional spatial coordinate (x, y, z)
$\vec{r}_j$	m	Coordinate of jth instrument (x_j, y_j)
σ^2		Variance
$S_{jm}(\omega)$	Pa^2 s	Cross spectrum of jth and mth instrument at ω
τ	s^{-1}	Relaxation time of microbarometer
T		Number of samples $t = 1, ..., T$
$T_{A_{max}}$	s	Infrasonic period at maximum amplitude
T_a	K	Absolute temperature
t	s	Time
$\vec{u}$	m s^{-1}	Vectorial wind
V	m^3	Size of backing volume
V_B		Variation between recordings
V_T		Total variation
V_W		Variation within recordings
V_d	m/s	Projection of wind on source-receiver path
V_t	V	Time indexed voltage
v	m^3	Size of fore volume
$w(\vec{r}_j)$		Sensitivity of jth instrument
x_{nt}	Pa	Recording of instrument n at time t
$\bar{x}$	Pa	Grand average over all recordings
$\bar{x}_t$	Pa	Average over all recordings at time t
Y	kT TNT	Yield of explosion
Zw	m/s	Zonal wind

A.2 Abbreviations

CTBT	Comprehensive Nuclear-Test-Ban Treaty
DBN	De Bilt Infrasound Array
DIA	Deelen Infrasound Array
ECMWF	European Centre for Medium-Range Weather Forecasts
EXL	Exloo Infrasound Array
F-ratio	Fisher ratio
F-distribution	Fisher distribution
GPS	Global Positioning System
HE	High Explosives
HWM/MSISE	Horizontal Wind Model/Mass Spectrometer and Incoherent Scatter Radar Extended Model

IMS	International Monitoring System
KNMI	Royal Netherlands Meteorlogical Institute
LOFAR	Low Frequency Array
NRL-G2S	US Naval Research Laboratory-Ground To Space
PMCC	Progressive Multi Channel Correlation
PVC	Polyvinyl chloride
SBL	Stable Boundary Layer
STA/LTA	Short Term Average over Long Term Average
TEMA	Texel Experimental Monitoring Array
TCP/IP	Transmission Control Protocol/Internet Protocol
TNT	Trinitrotoluene
UTC	Universal Time Coordinated
WIT	Witteveen Infrasound Array

B

Constructional drawing of the KNMI microbarometer
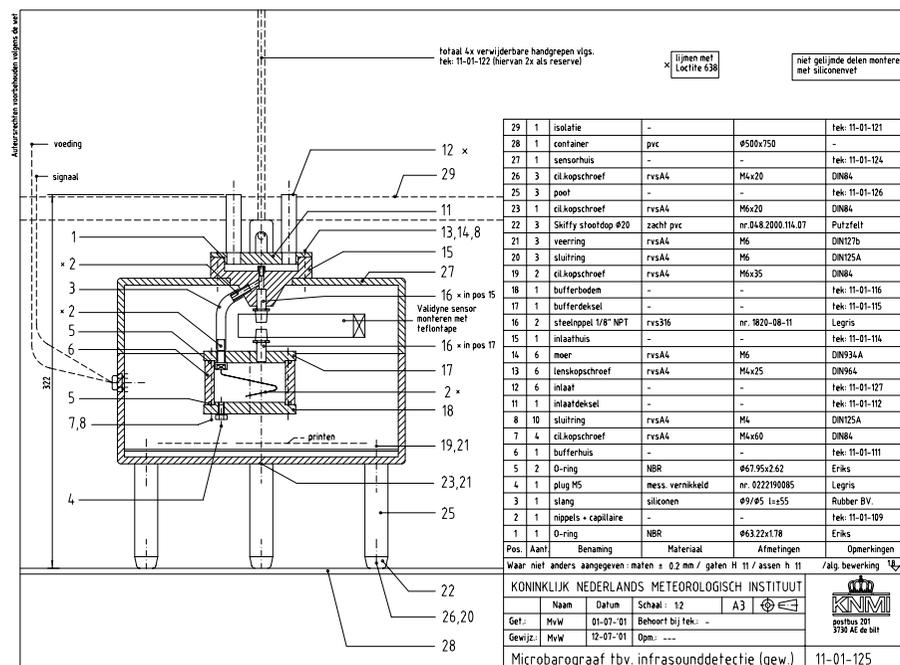
Figure B.1: *The constructional drawing of a KNMI microbarometer. The following main elements can distinguished, from top the bottom, the inlets (12) and inlet box (15), the Validyne sensor and the backing volume (6) with the capillary (2) included. More detail on each element is given in consecutive figures in this appendix.*

φ13x1.5

60

10

φ12 ×

× speling ±0.03 ivm. lijmen
tov. tek: 11-01-112

SCHERPE KANTEN BREKEN R=0.2

BLANK ANODISEREN MAATVAST 25 MICRON

| 1 | 1 | pijp | al. 50ST | φ13x1.5 l=60 | -- |
| Pos. | Aant. | Benaming | Materiaal | Afmetingen | Opmerkingen |

Waar niet anders aangegeven : maten ± 0.2mm / gaten H 9 / assen h 9   /alg. bewerking 63

KONINKLIJK NEDERLANDS METEOROLOGISCH INSTITUUT

	Naam	Datum	Schaal : 1:1	A4
Get.:	MvW	12-07-'01	Behoort bij tek.: 11-01-125	
Gewijz.:	MvW	-	Opm.: ---	

inlaat tbv. 11-01-125

11-01-127

postbus 201
3730 AE de bilt

Figure B.2: *Drawing of one of the six inlets for attaching the noise reducer.*

Auteursrechten voorbehouden volgens de wet

88

stc.48

stc.76

90°

ϕ12 ×
(6x60°)

ϕ7.5
(6x60°)

1x45°

10

6

ϕ4.2
(6x60°)

0.5x45°

ϕ64g8

SCHERPE KANTEN BREKEN R=0.2

BLANK ANODISEREN MAATVAST 25 MICRON

× speling ±0.03 ivm. lijmen
tov. tek:11-01-113

1	1	staf	al. 51ST	ϕ88x10	--
Pos.	Aant.	Benaming	Materiaal	Afmetingen	Opmerkingen

Waar niet anders aangegeven : maten ± 0.2mm / gaten H 9 / assen h 9 /alg. bewerking 63

KONINKLIJK NEDERLANDS METEOROLOGISCH INSTITUUT

	Naam	Datum	Schaal : 1:1	A4	
Get.:	MvW	26-10-'98	Behoort bij tek.: 11-01-108		
Gewijz.:	MvW	20-11-'98	Opm.: ---		

KNMI

postbus 201
3730 AE de bilt

inlaatdeksel tbv. 11-01-108

11-01-112

Figure B.3: *Top of the inletbox where the six inlets are mounted on.*
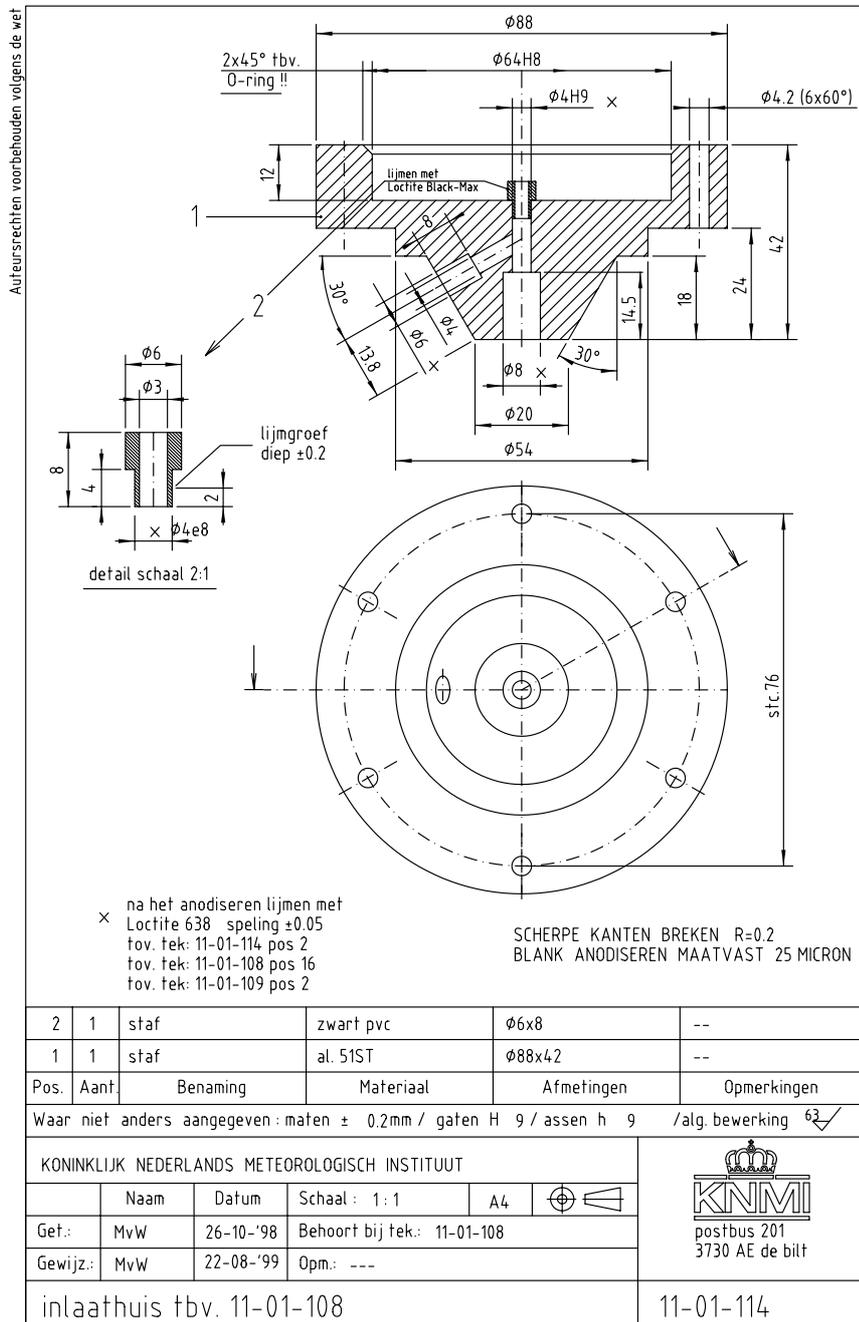
Figure B.4: *The inlet house for connecting the inlet box to the sensor.*
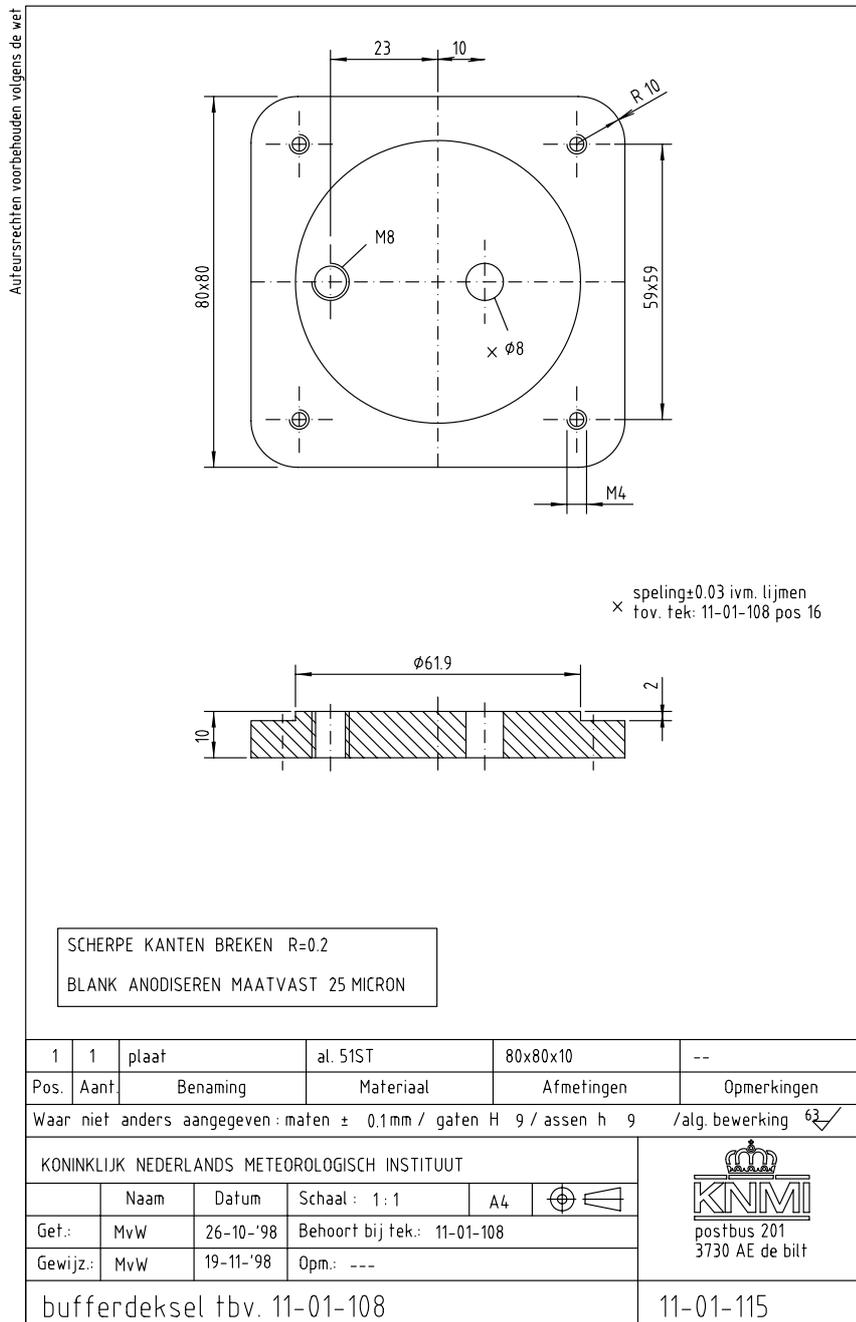
Figure B.5: *The top plate of the backing volume, enabling the connection of the sensor to the backing volume.*

⌀67.3 3.2

38

2.1

⌀62

⌀78

SCHERPE KANTEN BREKEN R=0.2

BLANK ANODISEREN MAATVAST 25 MICRON

| 1 | 1 | pijp | al. 50ST | ⌀78/⌀62x38 | -- |
| Pos. | Aant. | Benaming | Materiaal | Afmetingen | Opmerkingen |

Waar niet anders aangegeven : maten ± 0.2mm / gaten H 9 / assen h 9 /alg. bewerking 63

KONINKLIJK NEDERLANDS METEOROLOGISCH INSTITUUT

	Naam	Datum	Schaal : 1:1	A4		
Get.:	MvW	26-10-'98	Behoort bij tek.: 11-01-108			
Gewijz.:	MvW	20-11-'98	Opm.: ---			

KNMI

postbus 201
3730 AE de bilt

bufferhuis tbv. 11-01-108

11-01-111

Figure B.6: *The backing volume*
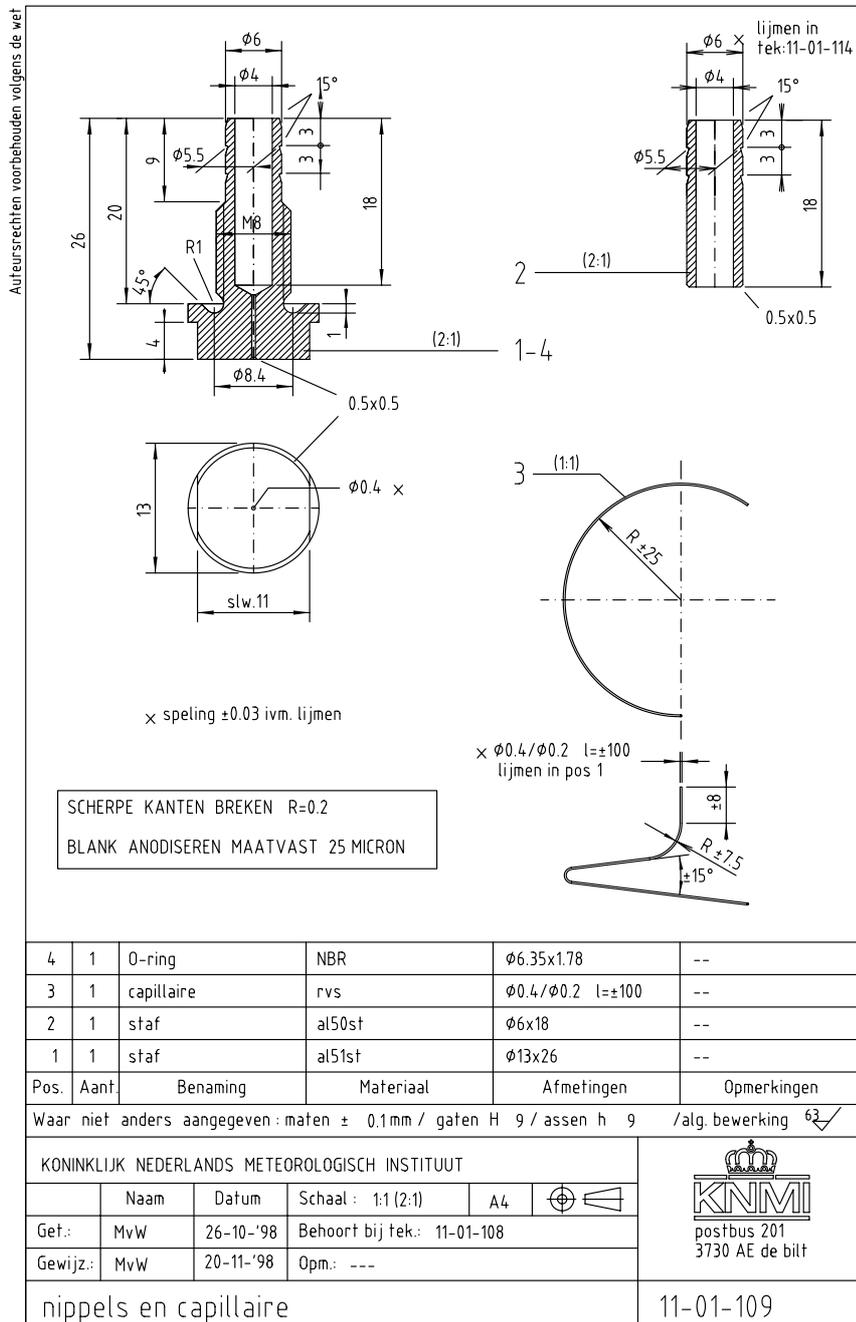
Figure B.7: *The capillary as mounted within the backing volume.*

R 10

80x80

59x59

25

4.2

Ø61.9

10

2

M5

SCHERPE KANTEN BREKEN R=0.2

BLANK ANODISEREN MAATVAST 25 MICRON

| 1 | 1 | plaat | al. 51ST | 80x80x10 | -- |
| Pos. | Aant. | Benaming | Materiaal | Afmetingen | Opmerkingen |

Waar niet anders aangegeven : maten ± 0.2mm / gaten H 9 / assen h 9 /alg. bewerking 63

KONINKLIJK NEDERLANDS METEOROLOGISCH INSTITUUT

	Naam	Datum	Schaal : 1 : 1	A4	
Get.:	MvW	26-10-'98	Behoort bij tek.: 11-01-108		
Gewijz.:	MvW	30-10-'98	Opm.: ---		

KNMI
postbus 201
3730 AE de bilt

bufferbodem tbv. 11-01-108   11-01-116

Figure B.8: *The bottom plate of the backing volume*
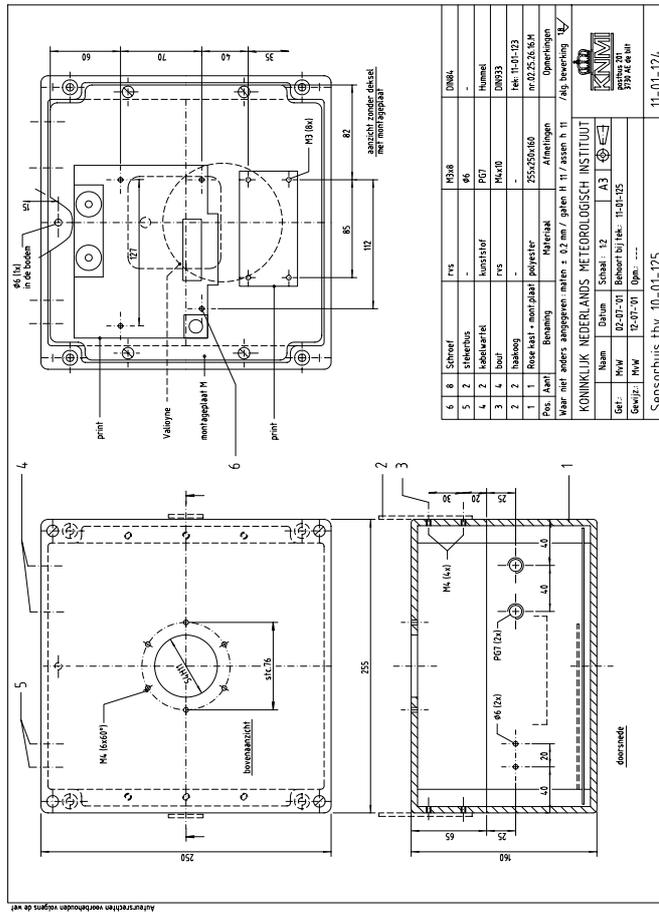
Figure B.9: *The housing of the microbarometer*

Coordinates of the KNMI infrasound arrays

The coordinates of the microbarometers in the KNMI infrasound arrays are given in decimal geographical coordinates (latitude and longitude in degrees) and in Rijks-driehoek coordinates (x_{RD},y_{RD}), in meters. The RD coordinate system is an approximate orthogonal grid for the Netherlands. The relative coordinates (x,y) as used in Figure 2.10 are also given. Within the labels, the average array coordinates are given.

Table C.1: *Coordinates of DBN (52.1000,5.1764)°, (140525.00,456775.00)m*

	lat.(°)	lon.(°)	x_{RD}(m)	y_{RD}(m)	x(m)	y(m)
01	52.1001	5.1758	140488.92	456787.50	−36.08	12.50
02	52.1002	5.1761	140510.57	456800.00	−14.43	25.00
03	52.1002	5.1768	140553.87	456800.00	28.87	25.00
04	52.1000	5.1768	140553.87	456775.00	28.87	0.00
05	52.0997	5.1765	140532.22	456737.50	7.22	−37.50
06	52.0998	5.1761	140510.57	456750.00	−14.43	−25.00

Table C.2: *Coordinates of DIA (52.0573,5.8819)°, (188896.66,452120.24)m*

	lat.(°)	lon.(°)	x_{RD}(m)	y_{RD}(m)	x(m)	y(m)
01	52.0612	5.8878	189297.09	452549.12	400.43	428.88
02	52.0600	5.8913	189536.46	452423.86	639.80	303.62
03	52.0586	5.8928	189642.07	452264.96	745.41	144.72
04	52.0504	5.8850	189112.59	451355.81	215.93	−764.43
05	52.0504	5.8821	188912.56	451353.56	15.90	−766.68
06	52.0504	5.8792	188711.60	451351.82	−185.06	−768.42
07	52.0582	5.8717	188197.39	452212.29	−699.27	92.05
08	52.0599	5.8726	188254.83	452403.74	−641.83	283.50
09	52.0621	5.8737	188325.41	452642.36	−571.25	522.12
10	52.0568	5.8868	189232.81	452064.77	336.15	−55.47
11	52.0548	5.8909	189515.85	451839.73	619.19	−280.51
12	52.0589	5.8808	188816.42	452297.47	−80.24	177.23
13	52.0603	5.8771	188560.82	452454.47	−335.84	334.23
14	52.0560	5.8834	188997.00	451974.27	100.34	−145.97
15	52.0560	5.8717	188198.27	451967.79	−698.39	−152.45
16	52.0631	5.8840	189035.40	452767.84	138.74	647.60

Table C.3: *Coordinates of EXL (52.9086,6.8664)°, (254465.63 547732.42)m*

	lat.(°)	lon.(°)	x_{RD}(m)	y_{RD}(m)	x(m)	y(m)
01	52.9091	6.8660	254441.08	547791.12	−24.55	58.70
02	52.9079	6.8662	254455.81	547649.62	−9.82	−82.80
03	52.9094	6.8647	254348.55	547815.40	−117.08	82.98
04	52.9078	6.8667	254486.25	547639.74	20.62	−92.68
05	52.9093	6.8685	254607.17	547815.52	141.54	83.10
06	52.9082	6.8662	254454.92	547683.12	−10.71	−49.30

Table C.4: *Coordinates of TEMA (53.1718,4.8721)°, (120531.47,576124.41)m*

	lat.(°)	lon.(°)	x_{RD}(m)	y_{RD}(m)	x(m)	y(m)
01	53.1720	4.8732	120602.73	576147.40	71.25	23.00
02	53.1725	4.8721	120531.70	576199.19	0.23	74.79
03	53.1720	4.8710	120459.96	576146.98	−71.51	22.57
04	53.1713	4.8715	120487.24	576063.54	−44.24	−60.87
05	53.1713	4.8728	120575.34	576063.91	43.87	−60.49
06	53.1718	4.8721	120531.87	576125.41	0.39	1.01

Table C.5: *Coordinates of WIT (52.8135,6.6693)°, (241395.44,536901.90)m*

	lat.(°)	lon.(°)	x_{RD}(m)	y_{RD}(m)	x(m)	y(m)
01	52.8136	6.6695	241413.03	536906.59	17.59	4.69
02	52.8137	6.6693	241395.53	536921.43	0.09	19.53
03	52.8136	6.6690	241377.99	536906.89	−17.45	4.99
04	52.8134	6.6691	241385.06	536888.47	−10.38	−13.43
05	52.8134	6.6694	241406.24	536888.23	10.80	−13.67
06	52.8135	6.6692	241394.79	536899.77	−0.65	−2.13

The F-ratio

D.1 Splitting of the total variation

The aim is to split the equation for the total variation V_T in a within V_W and between recording component V_B [*Spiegel and Stephens*, 2008]. The total variation was given as:

$$V_T = \sum_{t=1}^{T} \sum_{n=1}^{N} (x_{nt} - \bar{x})^2 \tag{D.1.1}$$

with:

$$\bar{x} = \frac{1}{N} \sum_{n=1}^{N} x_n \tag{D.1.2}$$

can be written as:

$$V_T = \sum_{t=1}^{T} \sum_{n=1}^{N} (x_{nt} - \bar{x}_t)^2 + \sum_{t=1}^{T} \sum_{n=1}^{N} (\bar{x}_t - \bar{x})^2 + 2 \sum_{t=1}^{T} \sum_{n=1}^{N} (x_{nt} - \bar{x}_t)(\bar{x}_t - \bar{x}) \tag{D.1.3}$$

or:

$$V_T = \sum_{t=1}^{T} \sum_{n=1}^{N} (x_{nt} - \bar{x}_t)^2 + N \sum_{t=1}^{T} (\bar{x}_t - \bar{x})^2 + 2 \sum_{t=1}^{T} \sum_{n=1}^{N} (x_{nt} - \bar{x}_t)(\bar{x}_t - \bar{x}) \tag{D.1.4}$$

with:

$$\bar{x}_t = \frac{1}{N} \sum_{n=1}^{N} x_{nt} \tag{D.1.5}$$

Thus:

$$V_T = V_W + V_B \tag{D.1.6}$$

if:

$$\sum_{t=1}^{T} \sum_{n=1}^{N} (x_{nt} - \bar{x}_t)(\bar{x}_t - \bar{x}) = 0 \tag{D.1.7}$$

which is true, since:

$$\sum_{t=1}^{T} \sum_{n=1}^{N} (x_{nt} - \bar{x}_t)(\bar{x}_t - \bar{x}) = \sum_{t=1}^{T} (\bar{x}_t - \bar{x}) \left(\sum_{n=1}^{N} (x_{nt} - \bar{x}_t) \right) \tag{D.1.8}$$

$$= \sum_{t=1}^{T} (\bar{x}_t - \bar{x}) \left(\sum_{n=1}^{N} x_{nt} - N\bar{x}_t \right) = 0 \tag{D.1.9}$$

because:

$$\bar{x} = \frac{1}{N} \sum_{n=1}^{N} x_n \tag{D.1.10}$$

D.2 Derivation of the F-ratio

The general definition of the variance, of the measured value x by N instruments, is given by:

$$\sigma^2 = \frac{\sum_{n=1}^{N} (x_n - \bar{x})^2}{N-1} \tag{D.2.11}$$

with the average:

$$\bar{x} = \frac{1}{N} \sum_{n=1}^{N} x_n \tag{D.2.12}$$

This can be rewritten to:

$$\sigma^2 = \frac{\sum_{n=1}^{N} x_n^2 + \sum_{n=1}^{N} \bar{x}^2 - 2\sum_{n=1}^{N} x_n \bar{x}}{N-1} \tag{D.2.13}$$

$$= \frac{\sum_{n=1}^{N} x_n^2 + N\bar{x}^2 - 2\bar{x} \sum_{n=1}^{N} x_n}{N-1} \tag{D.2.14}$$

$$= \frac{\sum_{n=1}^{N} x_n^2 + N\bar{x}^2 - 2N\bar{x}^2}{N-1} \tag{D.2.15}$$

$$= \frac{\sum_{n=1}^{N} x_n^2 - N\bar{x}^2}{N-1} \tag{D.2.16}$$

$$= \frac{\sum_{n=1}^{N} x_n^2 - \frac{1}{N}(\sum_{n=1}^{N} x_n)^2}{N-1} \tag{D.2.17}$$

where, the cross term and averages have been handled such that σ^2 is now only a function of x_n.

By using the above result, the variation within the recordings, or total power within the data:

$$V_W = \sum_{t=1}^{T} \sum_{n=1}^{N} (x_{nt} - \bar{x}_t)^2 \tag{D.2.18}$$

with:

$$\bar{x}_t = \frac{1}{N} \sum_{n=1}^{N} x_{nt} \tag{D.2.19}$$

can be rewritten to:

$$V_W = \sum_{t=1}^{T} \sum_{n=1}^{N} x_{nt}^2 - \frac{1}{N} \sum_{t=1}^{T} (\sum_{n=1}^{N} x_{nt})^2 \tag{D.2.20}$$

The variation between the recordings, or signal power, was given as:

$$V_B = N \sum_{t=1}^{T} (\bar{x}_t - \bar{x})^2 \tag{D.2.21}$$

with:

$$\bar{x} = \frac{1}{NT} \sum_{t=1}^{T} \sum_{n=1}^{N} x_{nt} \tag{D.2.22}$$

can be written as:

$$V_B = N \sum_{t=1}^{T} \bar{x}_t^2 - NT\bar{x}^2 \tag{D.2.23}$$

$$V_B = N \sum_{t=1}^{T} (\frac{1}{N} \sum_{n=1}^{N} x_{nt})^2 - NT \frac{1}{(NT)^2} (\sum_{t=1}^{T} \sum_{n=1}^{N} x_{nt})^2 \tag{D.2.24}$$

$$V_B = \frac{1}{N} \left(\sum_{t=1}^{T} (\sum_{n=1}^{N} x_{nt})^2 - \frac{1}{T} (\sum_{t=1}^{T} \sum_{n=1}^{N} x_{nt})^2 \right) \tag{D.2.25}$$

The F-ratio was given by:

$$F = \frac{V_B/(T-1)}{V_W/T(N-1)} \tag{D.2.26}$$

by substituting equation D.2.20 and D.2.25, the *Melton and Bailey* [1957] expression for the Fisher ratio is obtained, as:

$$F = \frac{T(N-1)}{N(T-1)} \frac{\sum_{t=1}^{T} (\sum_{n=1}^{N} x_{nt})^2 - \frac{1}{T} (\sum_{t=1}^{T} \sum_{n=1}^{N} x_{nt})^2}{\sum_{t=1}^{T} \sum_{n=1}^{N} x_{nt}^2 - \frac{1}{N} \sum_{t=1}^{T} (\sum_{n=1}^{N} x_{nt})^2} \tag{D.2.27}$$

Bibliography

Antier, K., A. Le Pichon, S. Vergniolle, C. Zielinski, and M. Lardy (2007), Multiyear validation of the NRL-G2S wind fields using infrasound from Yasur, *J. Geoph. Res.*, *112*, D23110.

Assink, J. D., L. G. Evers, I. Holleman, and H. Paulssen (2008), Characterization of infrasound from lightning, *Geoph. Res. Lett.*, *35*, L15802.

Balachandran, N. M., W. L. Donn, and D. Rind (1977), Concorde sonic booms as an atmospheric probe, *Science*, *197*, 47–49.

Bass, H. E., H. J. Bauer, and L. B. Evans (1972), Atmospheric absorption of sound: analytical expressions, *J. Acoust. Soc. Am.*, *52*, 821–825.

Benioff, H., and B. Gutenberg (1939), Waves and currents recorded by electromagnetic barographs, *Bull. Am. Meteo. Soc.*, *20*, 412–426.

Blanc, E. (1985), Observation in the upper atmosphere of infrasound waves from natural and artificial sources, *Annales Geophysicae*, *3*, 673–688.

Blandford, R. R. (1974), An automatic event detector at the Tonto Forest seismic observatory, *Geophysics*, *39*, 633–643.

Bowman, H. S., and A. J. Bedard (1971), Observations of infrasound and subsonic disturbances related to severe weather, *Geoph. J. R. Astr. Soc.*, *26*, 215–242.

Brown, D. J., C. N. Katz, R. L. Bras, M. P. Flanagan, J. Wang, and A. K. Gault (2002a), Infrasonic signal detection and source location at the Prototype Data Centre, *Pure and App. Geoph.*, *159*, 1081–1125.

Brown, P., R. E. Spalding, D. O. ReVelle, E. Tagliaferri, and S. P. Worden (2002b), The flux of small near-Earth objects colliding with the Earth, *Nature*, *420*, 294–296.

Burridge, R. (1971), The acoustics of pipe arrays, *Geoph. J. R. Astr. Soc.*, *26*, 53–69.

Calais, E., and J. B. Minster (1995), GPS detection of ionospheric perturbations following the January 17, 1994, Northridge Earthquake, *Geoph. Res. Lett.*, *22*, 1045–1048.

Caljé, L. (2005), Exploring the boundaries of the Fisher and PMCC signal-detectors using infrasound signals, Master thesis, Utrecht University.

Cansi, Y. (1995), An automatic seismic event processing for detection and location: The P.M.M.C. method, *Geoph. Res. Lett.*, *22*, 1021–1024.

Capon, J. (1969), High-resolution frequency-wavenumber spectrum analysis, *Proceedings of the IEEE*, *57*, 1408–1418.

Christie, D. R. (1989), Long nonlinear waves in the lower atmosphere, *J. Atmos. Sc.*, *46*, 1462–1491.

Christie, D. R. (1992), The Morning Glory of the Gulf of Carpentaria: a paradigm for nonlinear waves in the lower atmosphere, *Aust. Met. Mag.*, *41*, 21–60.

Christie, D. R. (2007), Recent progress in wind noise reduction at infrasound monitoring station, in *Infrasound Technology Workshop 2007*, Japan Weather Association and Center for the Promotion of Disarmament and Non-Proliferation, Tokyo, Japan.

Christie, D. R., K. J. Muirhead, and A. L. Hales (1978), On solitary waves in the atmosphere, *J. Atmos. Sc.*, *35*, 805–825.

Daniels, F. B. (1950), On the propagation of sound waves in a cylindrical conduit, *J. Acoust. Soc. Am.*, *22*, 563–564.

Daniels, F. B. (1959), Noise-reducing line microphones for frequencies below 1 cps, *J. Acoust. Soc. Am.*, *31*, 529–531.

Denholm-Price, J. C. W., and J. M. Rees (1999), Detecting waves using an array of sensors, *Monthly Weather Review*, *127*, 57–69.

Dessler, A. J. (1973), Infrasonic thunder, *J. Geoph. Res.*, *78*, 1889–1896.

Donn, W. L., and N. K. Balachandran (1974), Meteors and meteorites detected by infrasound, *Science*, *185*, 707–709.

Drob, D. P., J. M. Picone, and M. A. Garcés (2003), The global morphology of infrasound propagation, *J. Geoph. Res.*, *108*, 4680.

Evers, L. G. (2005), Infrasound monitoring in the Netherlands, *J. of the Neth. Acoust. Soc.*, *176*, 1–11.

Evers, L. G., and H. W. Haak (2000), The Deelen Infrasound Array: on the detection and identification of infrasound, *Technical Report 225*, Royal Netherlands Meteorological Institute.

Evers, L. G., and H. W. Haak (2001), An optimal infrasound array at Apatity (Russian Federation), *KNMI-publication 195*, Royal Netherlands Meteorological Institute.

Evers, L. G., and H. W. Haak (2001b), Listening to sounds from an exploding meteor and oceanic waves, *Geoph. Res. Lett.*, *28*, 41–44.

Evers, L. G., and H. W. Haak (2003), Tracing a meteoric trajectory with infrasound, *Geoph. Res. Lett.*, *30*, 2246.

Evers, L. G., and H. W. Haak (2005), Atmospheric processes controlling the number of infrasound detections, in *Infrasound Technology Workshop 2005*, Commissariat a l'Energie Atomique, Papeete, Tahiti, French Polynesia.

Farges, T., E. Blanc, A. Le Pichon, T. Neubert, and T. H. Allin (2005), Identification of infrasound produced by sprites during the Sprite2003 campaign, *Geoph. Res. Lett.*, *32*, L01813.

Few, A. A. (1969), Power spectrum of thunder, *J. Geoph. Res.*, *74*, 6926–6934.

Fisher, R. A. (1948), *Statistical methods for research workers*, Oliver and Boyd, London.

Garcés, M. A., R. A. Hansen, and K. G. Lindquist (1998), Traveltimes for infrasonic waves propagating in a stratified atmosphere, *Geoph. J. Int.*, *135*, 255–263.

Garcés, M. A., S. R. McNutt, R. A. Hansen, and J. C. Eichelberger (2000), Application of wave-theoretical seismoacoustic models to the interpretation of explosion and eruption tremor signals radiated by Pavlof volcano, Alaska, *J. Geoph. Res.*, *105*, 3039–3058.

Garcés, M. A., M. Willis, C. H. Hetzer, A. Le Pichon, and D. Drob (2004), On using ocean swells for continuous infrasonic measurements of winds and temperature in the lower, middle and upper atmosphere, *Geoph. Res. Lett.*, *31*, L19,304.

Glasstone, S. (1957), *The effect of nuclear weapons*, United States Atomic Energy Commission, Washington D.C.

Godin, O. A. (2006), Recovering the acoustic Green's function from ambient noise cross correlation in an inhomogeneous moving medium, *Phys. Rev. Lett.*, *97*, 054301.

Gossard, E. E., and W. H. Hooke (1975), *Waves in the atmosphere*, Elsevier Scientific Publishing Company, Amsterdam.

Gutenberg, B. (1939), The velocity of sound waves and the temperature in the stratosphere in southern California, *Bull. Am. Meteo. Soc.*, *20*, 192–201.

Haak, H. W. (1996), An acoustical array for subsonic signals, *Technical Report 96-03*, Royal Netherlands Meteorological Institute.

Haak, H. W., and G. J. de Wilde (1996), Microbarograph systems for the infrasonic detection of nuclear explosions, *Technical Report 96-06*, Royal Netherlands Meteorological Institute.

Hartmann, G., and M. Henger (2000), Milestones of the IS26 installation, in *Infrasound Workshop 2000*, BGR, Passau, Germany.

Haubrich, R. A. (1968), Array design, *Bull. Seism. Soc. Am.*, *58*, 977–991.

Hedin, A. E., et al. (1996), Empirical wind model for the upper, middle and lower atmosphere, *J. Atm. Terr. Phys.*, *58*, 1421–1447.

Hedlin, M. A. H., B. Alcoverro, and G. D'Spain (2003), Evaluation of rosette infrasonic noise-reducing spatial filters, *J. Acoust. Soc. Am.*, *114*, 1807–1820.

Heyburn, R., and D. Bowers (2007), The relative amplitude method: exploiting F-statistics from array seismograms, *Geoph. J. Int*, *170*, 813–822.

Holton, J. R. (1979), *An introduction to dynamic meteorology*, Academic Press, London.

Kinney, G. F., and K. J. Graham (1985), *Explosive shocks in air*, Springer Verlag, New York.

Koper, K. D., T. C. Wallace, and D. Hollnack (1999), Seismic analysis of the 7 August 1998 truckbomb blast at the American Embassy in Nairobi, Kenya, *Seism. Res. Lett.*, *70*, 512–521.

Koper, K. D., T. C. Wallace, and R. C. Aster (2003), Seismic recording of the Carlsbad, New Mexico, pipeline explosion on 19 August 2000, *Bull. Seism. Soc. Am.*, *93*, 1427–1432.

Kulichkov, S. N., K. V. Avilov, G. A. Bush, O. E. Popov, O. M. Raspopov, A. K. Baryschnikov, D. O. ReVelle, and R. W. Whitaker (2004), On anomalously fast infrasonic arrivals at long distances from surface explosions, *Izvestiya, Atmospheric and Oceanic Physics*, *40*, 1–9.

Lacoss, R. T., E. J. Kelly, and M. N. Toksöz (1969), Estimation of seismic noise structure using arrays, *Geophysics*, *34*, 21–38.

Le Pichon, A., and L. Ceranna (2006), The Buncefield fire: A benchmark for infrasound analysis in Europe, in *Infrasound Technology Workshop 2006*, University of Fairbanks, Alaska, Fairbanks, United States of America.

Le Pichon, A., M. Garcés, E. Blanc, M. Barthélémy, and D. P. Drob (2002a), Acoustic propagation and atmosphere characteristics derived from infrasonic waves generated by the Concorde, *J. Acoust. Soc. Am.*, *111*, 629–641.

Le Pichon, A., J. M. Guérin, E. Blanc, and D. Reymond (2002b), Trail in the atmosphere of the 29 December 2000 meteor as recorded in Tahiti: Characteristics and trajectory reconstruction, *J. Geoph. Res.*, *107*, 4709.

Liszka, L. (1974), Long-distance propagation of infrasound from artificial sources, *J. Acoust. Soc. Am.*, *56*, 1383–1388.

Liszka, L. (1978), Long-distance focusing of Concorde sonic boom, *J. Acoust. Soc. Am.*, *64*, 631–635.

Liszka, L. (2004), On the possible infrasound generation by sprites, *J. of Low Frequency Noise, Vibration, and Active Control*, *23*, 85–93.

Liszka, L. (2008), Infrasound: A summary of 35 years of infrasound research, *IRF Scientific report 291*, Swedish Institute of Space Physics.

Liszka, L., and M. A. Garcés (2002), Infrasonic observations of the Hekla eruption of February 26, 2000, *J. of Low Frequency Noise, Vibration, and Active Control*, *21*, 1–8.

Longuet-Higgins, M. S. (1950), A theory of the origin of microseism, *Phil. Trans. R. Soc. of London*, *243*, 1–35.

Mack, H., and E. A. Flinn (1971), Analysis of the spatial coherence of short-period acoustic-gravity waves in the atmosphere, *Geoph. J. R. Astr. Soc.*, *26*, 255–269.

Manders, B. (2004), Major gas pipe explodes at 80 bar, killing eighteen, *Offshore newsletter*, Fugro Robertson BV, Netherlands Offshore Information Services.

McIntosh, B. A., M. D. Watson, and D. O. ReVelle (1976), Infrasound from a radar-observed meteor, *Canadian J. of Phys.*, *54*, 655–662.

Melton, B. S., and L. F. Bailey (1957), Multiple signal correlators, *Geophysics*, *XXII*, 565–588.

Mentink, J. H., and L. G. Evers (2008), The response of the KNMI microbarometer, *Technical report*, Royal Netherlands Meteorological Institute, in preparation.

NOAA, NASA, and USAF (1976), *US Standard Atmosphere, 1976*, U.S. Governement Printing Office, Washington D.C.

Olson, J. V. (2004), Infrasound signal detection using the Fisher F-statistics, *Inframatics: the newsletter of subaudible sound*, *6*, 1–8, available through: www.inframatics.org.

Ørbæk, J. B., and M. Naustvik (1995), Infrasonic signatures of a polar low in the Norwegian and Barents Sea on 23-27 March 1992, *Tellus*, *47A*, 921–940.

Ottemöller, L., and L. G. Evers (2008), Seismo-acoustic analysis of the Buncefield oil depot explosion in the UK, 2005 December 11, *Geoph. J. Int.*, *172*, 1123–1134.

Pain, H. J. (1983), *The physics of vibrations and waves*, John Wiley & Sons Limited, Great Britain.

Petit, M. E. (2000), Infrasonic wave propagation through the atmosphere, Master thesis, Utrecht University.

Pierce, A. D. (1989), *Acoustics: An introduction to its physical principles and applications*, Acoustical Society of America, Melville, USA.

Posey, J. W., and A. D. Pierce (1971), Estimation of nuclear explosion energies from microbarograph records, *Nature*, *232*, 253.

Posmentier, E. S. (1967), A theory of microbaroms, *Geoph. J. R. Astr. Soc.*, *13*, 487–501.

PrepCom (1997), *Comprehensive Nuclear-Test-Ban Treaty (CTBT)*, 139 pp., Preparatory Commission for the Comprehensive Nuclear-Test-Ban Treaty Organization, Austria.

ReVelle, D. O. (1975), Studies of sounds from meteors, *Sky and Telescope*, *49*, 87–91.

ReVelle, D. O. (1976), On meteor-generated infrasound, *J. Geoph. Res.*, *81*, 1217–1230.

ReVelle, D. O. (1997), Historical detection of atmospheric impacts of large superbolides using acoustic-gravity waves, *Ann. N.Y. Acad. Sc.*, *822*, 284–302.

Rind, D. H., and W. L. Donn (1978), Infrasound observations of variability during stratospheric warmings, *J. Atm. Sc.*, *35*, 546–553.

Ripepe, M., P. Poggi, T. Braun, and E. Gordeev (1996), Infrasonic waves and volcanic tremor at Stromboli, *Geoph. Res. Lett.*, *23*, 181–184.

Salby, M. L. (1996), *Fundamentals of atmospheric physics*, Academic Press, San Diego.

Shaw, T. A., and T. G. Shepherd (2008), Raising the roof, *Nature Geoscience*, *1*, 12–13.

Shaw, W. N., and W. H. Dines (1904), The study of the minor fluctutations of atmospheric pressure, *Q. J. R. Meteorological Soc.*, *31*, 39–52.

Shields, F. D. (2005), Low-frequency wind noise correlation in microphone arrays, *J. Acoust. Soc. Am.*, *117*, 3489–3496.

Shumway, R. H. (1971), On detecting a signal in N stationarily correlated noise series, *Technometrics*, *13*, 499–519.

Smart, E., and E. A. Flinn (1971), Fast frequency-wavenumber analysis and Fisher signal detection in real-time infrasonic array data processing, *Geoph. J. R. Astr. Soc.*, *26*, 279–284.

Smirnov, A. A. (2006), Identification of the oil-well gas flare group as a unique infrasound source using I31KZ data, in *Infrasound Technology Workshop 2006*, Wilson Infrasound Observatories, Geophysical Institute, University of Alaska Fairbanks, Fairbanks, USA.

Spiegel, M. R., and L. J. Stephens (2008), *Statistics*, McGraw-Hill.

Spurný, P., J. Oberst, and D. Heinlein (2003), Photographic observations of Neuschwanstein, a second meteorite from the orbit of the Pribram chondrite, *Nature*, *423*, 151–153.

Sutherland, L. C., and H. E. Bass (2004), Atmospheric absorption in the atmosphere up to 160 km, *J. Acoust. Soc. Am.*, *115*, 1012–1032.

Symons, G. J. (Ed.) (1888), *The eruption of Krakatoa and subsequent phenomena*, Trübner & Co., London.

Szuberla, C. A. L., and J. V. Olson (2004), Uncertainties associated with parameter estimation in atmospheric infrasound arrays, *J. Acoust. Soc. Am.*, *115*, 253–258.

Van Lancker, E. (2001), Acoustic goniometry: a spatio-temporal approach, Ph.D. thesis, École Polytechnique Fédérale de Lausanne.

Wessel, P., and W. H. F. Smith (1991), Free software helps map and display data, *EOS Trans. AGU*, *72*, 441.

Whipple, F. J. W. (1930), The great siberian meteor and the waves, seismic and arial, which it produced, *Q. J. R. Meteorological Soc.*, *56*, 287–304.

Wilson, C. R. (1967), Infrasonic pressure waves from aurora: a shock wave model, *Nature*, *216*, 131–133.

Wilson, C. R. (1981), Atmospheric infrasound, *Antarctic J. of the U.S.*, *16*, 198–199.

Wilson, D. K., R. J. Greenfield, and M. J. White (2007), Spatial structure of low-frequency wind noise, *J. Acoust. Soc. Am.*, *122*, EL233.

Winer, B. J. (1962), *Statistical principles in experimental design*, McGraw-Hill Kogakusha, Ltd.

Summary

The inaudible symphony: on the detection and source identification of atmospheric infrasound

Infrasound consists of sound waves that travel through the atmosphere and are inaudible to humans because the frequency contents is lower than 20 Hz, i.e. the human hearing threshold. The lowest frequency is determined by the thickness of the atmospheric layer through which infrasound travels. In this thesis, infrasound is considered in the frequency range of 0.002 to 20 Hz, which propagates with acoustic velocities and has amplitudes in the range of 10^{-2} to 10 Pa at the receiver after having traveled over ranges of hundreds to thousands of kilometers.

Large and powerful sources are necessary to generate infrasound because only large displacements of air lead to a notable signal. Natural sources of infrasound are: meteors, volcanoes, avalanches, aurora, oceanic and sea waves, earthquakes, lightning and severe weather. Man-made events include: (accidental) chemical explosions, nuclear tests, gas flares, air traffic, sonic booms and the usage of munitions.

There is a wide variety of reasons why measuring infrasound is of interest. The ability to detect atmospheric nuclear tests has resulted in a broad attention for the study of infrasound in the past. After World War II, this monitoring aspect gained much interest, but came to an end with the signature of the Limited Test Ban Treaty in 1963. This Treaty confined nuclear tests to the underground. Only a small amount of scientists stayed interested in infrasound. With the signature of the Comprehensive Nuclear-Test-Ban Treaty (CTBT) in 1996, infrasound gained renewed interest as it was chosen as one of the verification techniques. Measuring infrasound also serves other purposes such as acoustic remote sensing of especially the upper atmosphere (higher than 20 km). Furthermore, insight can be obtained

in, for example, weather dependent sound propagation and detailed information on explosions can be derived for forensic investigations.

Three research objectives form the basis for this thesis:

- Develop a method to measure infrasound. This includes the construction of an instrument to detect infrasound and the configuration of arrays.

- Use signal detectors and array processing techniques to get insight in the information contained in the continuous recordings and to extract relevant signals.

- Apply the measurement and processing techniques to identify sources, which include knowledge on the propagation of infrasound through the atmosphere.

A differential microbarometer has been developed which is capable of measuring infrasound with a frequency contents between 0.002 and 20 Hz having amplitudes in the range of 10^{-2} to 10^2 Pa. Described are the considerations for properly constructing such an instrument and its phase and amplitude response. Arrays of microbarometers are deployed to characterize the signals and to reduce noise. Array design is based on the desired array response. Theoretically, an array should be capable of fully reconstructing the imposed wavefield. In practice, aliasing occurs due to the limited sampling in time and space. Several array configurations, i.e. aperture and number of instruments, are discussed which should optimally avoid aliasing in the required broad-band operations.

As arrays became operational, detection algorithms were developed as well as tools for array processing and parameter estimation, i.e. slowness. Detection on the basis of the Fisher ratio is described and applied in both the time and frequency domain. The evaluation of this F-ratio or statistical test is based on beamforming. Events are characterized by their slowness which also follows from beamforming. Slowness is related to characteristics like back azimuth and apparent sound speed.

An array of microbarometers detects of large amount of coherent signals, i.e. the inaudible symphony. Among those are the signals from meteors which are one of the few natural impulsive sources mimicking an atmospheric nuclear test in terms of yield. Two meteors have been studied in this thesis. One of them appeared to have a yield of 1.5 kT TNT equivalent. The infrasound verification network for the CTBT can detect a yield of 1 kT TNT eq. Therefore, this meteor was studied in detail and needed careful processing and interpretation since its energy was buried in the background noise of microbaroms. Microbaroms are generated by the non-linear interaction of oceanic waves and are almost continuously present with a dominant frequency of 0.2 Hz.

Infrasound from the second meteor was analyzed to resolve its moving character which enables a clear distinction from a static source like a nuclear test. Atmospheric specifications for wind and temperature are needed as input for the propagation model because the parameters determine the sound speed. Both climatological and actual atmospheric models were evaluated. The two distinct arrivals in the data

could be coupled to two explosion altitudes only with the actual models from the European Centre for Medium-Range Weather Forecasts (ECMWF).

Infrasound from the eruptions of Mt. Etna (Italy) was observed in the Netherlands in July 2001. Signals were only detected during the local night-time when the atmosphere stabilizes due to lack of solar radiation. Hundreds of coherent arrivals were identified as coming from Mt. Etna based on their wind-corrected back azimuths. This is achieved by taking into account the deviating effects of cross-winds on the observed back azimuth that affect the orientation of the wavefront along its propagation path. The detectability of the signals was studied by systematically lowering the number of elements and changing the apertures of the 16 element DIA infrasound array. The capabilities of arrays used for the verification of the CTBT were simulated in this way. Reducing the aperture of the array with a factor of two, means that two instruments less can be used to keep the same detection capabilities. This is also partly caused by the loss of spatial coherency in the boundary layer.

Accidental chemical explosions generate both seismic and infrasound signals and often have reliable ground truth information, i.e. information on location and time. With this information, the accuracy of phase identifiers, location procedures and propagation models can be assessed. Seismic and infrasound signals from a gas-pipeline explosion in Belgium observed over northwestern Europe have been studied to resolve the source location and yield. It appeared that the derived location and corresponding uncertainties could be reduced with a factor of two. This is achieved by correcting the back azimuths for cross-winds and discarding results from arrays with an unsuitable response. A yield estimate was realized by comparing the amplitudes of atmospheric arrivals to those from a high-explosives dataset.

Exceptionally fast arrivals were observed in the Netherlands after a vapor cloud explosion in the UK. The so-called forerunners experienced very strong winds around 40 km altitude of up to 150 m/s. This indicates that the highly variable nature of atmosphere, in both place and time, requires careful interpretation of data. Especially, phase identification on the basis of arrival time might lead to ambiguous results and needs attention in routine operations.

In summary, this thesis describes the complete sequence from measuring, processing and interpreting infrasound data which enables source identification as ultimate goal. The recorded signals are a convolution of the source and medium of propagation, i.e. the atmosphere and instrument response. Knowledge on all contributions is essential to accurately identify sources of atmospheric infrasound.

Läslo Gerardus Evers

Samenvatting

De onhoorbare symfonie: over de detectie en bron identificatie van atmosferisch infrageluid

Infrageluid wordt gevormd door geluidsgolven die door de atmosfeer reizen en on-hoorbaar zijn voor de mens omdat de frequentie-inhoud onder de 20 Hz, de gehoor-drempel, ligt. De laagste frequenties van infrageluid worden bepaald door de dikte van de atmosferische laag waardoor het infrageluid zich voortplant. In dit proef-schrift wordt infrageluid beschouwd in het frequentie-interval tussen de 0.002 en 20 Hz. Infrageluid reist met akoestische snelheden en heeft amplitudes tussen de 10^{-2} en 10 Pa.

Om infrageluid te genereren zijn grote en krachtige bronnen nodig, omdat veel lucht verplaatst moet worden om een meetbaar signaal op te wekken. Natuurlijke bron-nen zijn: meteoren, vulkanen, lawines, noorderlicht, oceaan- en zeegolven, aard-bevingen, onweer en zwaar weer. De mens kan ook infrageluid opwekken met onder andere de volgende bronnen: chemische explosies, kernbomproeven, affakkelen van gas, vliegverkeer, doorbreken van de geluidsbarrière en gebruiken van munitie.

Het meten van infrageluid dient vele doelen. Atmosferische kernbomproeven gener-eren infrageluid, iets wat tot veel aandacht voor het bestuderen van infrageluid heeft geleid, zeker na de Tweede Wereldoorlog. Toen in 1963 kernbomproeven alleen nog maar ondergronds gedaan werden, ten gevolge van de Limited Test Ban Treaty, nam de aandacht voor infrageluid af. Slechts een kleine groep wetenschappers bleef geïnteresseerd in het bestuderen van infrageluid. De interesse in infrageluid neemt sinds 1996 weer toe, omdat het als verificatietechniek voor het kernstopver-drag (Comprehensive Nuclear-Test-Ban Treaty; CTBT) gekozen is. Infrageluid kan ook gebruikt worden voor beeldvorming van de atmosfeer. Met name de hoge at-

mosfeer (hoger dan 20 km) kan met infrageluid in kaart worden gebracht. Andere voorbeelden van toepassingen zijn: het meten van weersafhankelijke geluidsvoortplanting en ondersteunen van forensisch onderzoek na explosies.

In deze dissertatie staan drie onderzoeksdoelen centraal, te weten:

- Het ontwikkelen van een techniek om infrageluid te meten. Dit omvat het maken van een instrument en het ontwerpen en installeren van zogeheten arrays. Dit zijn specifieke configuraties van instrumenten in het veld.

- Het ontwikkelen van detectie algoritmes en array analyse technieken om inzicht te krijgen in de informatie die in de continue meetgegevens zit. Tevens kunnen zo ook interessante signalen uit de meetgegevens gehaald worden.

- Het toepassen van de meet- en analysetechnieken om bronnen van infrageluid te identificeren, waarbij kennis over de voortplanting van infrageluid vereist is.

Een differentiële microbarometer is ontwikkeld om infrageluid te meten in het frequentie gebied van 0.002 tot 20 Hz, met amplitudes tussen de 10^{-2} en 10^2 Pa. Beschreven wordt hoe een microbarometer geconstrueerd kan worden en wat de fase- en amplituderesponse zijn. Arrays van microbarometers worden toegepast om de signalen te kunnen karakteriseren en om omgevingsruis te onderdrukken. Het ontwerp van een array is gebaseerd op de gewenste array response. In theorie zou een array in staat moeten zijn het gehele akoestische golfveld te reconstrueren. In de praktijk lukt dit maar gedeeltelijk omdat er in zowel de tijd als in de ruimte beperkte bemonstering mogelijk is. Verschillende array configuraties worden besproken die zo goed als mogelijk werken in een gewenst frequentiegebied.

Detectie-algoritmes en -programmatuur voor de analyse van array data zijn ontwikkeld om de meetgegevens van de arrays de kunnen verwerken. Detectie wordt gedaan op basis van de Fisher ratio in zowel het tijd- als frequentiedomein. De F-ratio, wat een statistische test is, wordt geëvalueerd door middel van bundelvorming. Hierbij is het doel om de traagheid (één gedeeld door de snelheid) van het signaal te bepalen. Deze traagheid is gerelateerd aan de richting waaruit het infrageluid komt en de propagatie snelheid.

Een array van microbarometers detecteert een groot aantal coherente infrageluid signalen, oftewel de onhoorbare symfonie. Eén van de bronnen is een meteoor, een natuurlijke impulsieve bron, waarvan het signaal qua sterkte op dat van een kernbomproef kan lijken. Eén van de bestudeerde meteoren had een explosieve kracht van 1.5 kT TNT equivalent. Het verificatienetwerk voor de CTBT kan een nucleaire test van 1 kT TNT eq. detecteren. Vandaar dat het infrageluid van deze meteoor in detail bekeken is, waarbij bleek dat de energie verborgen zat in de achtergrondruis. Deze ruis is vrijwel continue aanwezig en wordt veroorzaakt door de niet-lineaire interactie van oceaan golven. De opgewekte microbaromen hebben een dominante frequentie van 0.2 Hz.

Een atmosferische nucleaire test vindt plaats aan het aardoppervlak, terwijl een meteoor door de atmosfeer beweegt en dus niet als puntbron beschouwd kan worden.

Dit gegeven is gebruikt in de analyse van een tweede meteoor. De twee distincte aankomsten van energie van deze meteoor bleken opgewekt te zijn op twee hoogtes. Het lokaliseren van deze explosiehoogtes kon met behulp van gedetailleerde atmosfeergegevens uit modellen van het European Centre for Medium-Range Weather Forecasts (ECMWF). Met infrageluid kan onderscheid gemaakt worden tussen een statische nucleaire test en een bewegende meteoor.

Infrageluid van de erupties van de Etna in Italië is gemeten in Nederland in juli 2001. Met name 's nachts werd dit infrageluid gedetecteerd als de atmosfeer stabiliseert in afwezigheid van zonnestraling. Honderden aankomsten van de Etna zijn als zodanig geïdentificeerd waarbij de richting waaruit het infrageluid komt, gecorrigeerd is voor de invloeden van de wind. Het golffront ondergaat een translatie op de weg van bron naar ontvanger. De detecteerbaarheid van de signalen is onderzocht door het aantal elementen van het DIA infrageluid array systematisch te verminderen. Op deze manier werden arrays gesimuleerd die voor de verificatie van de CTBT in gebruik zijn. Verkleining van de diameter van het array leidde ertoe dat twee instrumenten minder gebruikt konden worden. Tevens is er een sterke afname in detecteerbaarheid als het aantal instrumenten afneemt. Dit wordt mede bepaald door het coherentieverlies in de atmosferische grenslaag.

Chemische explosies kunnen zowel seismische als infrageluid signalen genereren. Ook is er vaak gedetailleerde informatie over de lokatie en het tijdstip. Deze informatie is aangewend bij het interpreteren van de data en het testen van lokatieprocedures en voortplantingsmodellen. Meetgegevens van een explosie, ten gevolge van een ongeluk met een gaspijplijn, zijn gebruikt om te kijken hoe nauwkeurig de lokatie kon worden achterhaald. Er bleek dat een factor twee winst gehaald kon worden uit het gebruik van voor de wind gecorrigeerde richtingen voor het bepalen van de lokatie. Hierbij zijn gegevens van arrays in Noordwest-Europa gebruikt en moest onbetrouwbare informatie van te kleine arrays buiten beschouwing gelaten worden. De explosieve kracht is berekend door de gemeten amplitudes van de infrageluid aankomsten te vergelijken met die van een dataset van zware explosieven.

Buitengewoon snel gereisde infrageluid aankomsten zijn geobserveerd in Nederland na de explosie van een wolk van gasdamp in Engeland. Deze zogenaamde "forerunners" konden ontstaan ten gevolge van een zeer krachtige wind van 150 m/s op 40 km hoogte. De atmosfeer is een sterk variërend medium als functie van de tijd en plaats en er is dus voorzichtigheid geboden bij de interpretatie van de meetgegevens. Het identificeren van infrageluid aankomsten op basis van de reistijd kan tot dubbelzinnige uitkomsten leiden.

Deze dissertatie beschrijft het gehele traject van het meten, analyseren en de interpretatie van infrageluid waarbij het identificeren van de bron het ultieme doel is. De gemeten signalen zijn een convolutie van de bijdragen van bron, de atmosfeer en het instrument. Kennis van al deze bijdragen is essentieel in het succesvol identificeren van bronnen van atmosferisch infrageluid.

Läslo Gerardus Evers

Curriculum vitae

Läslo Gerardus Evers was born in Purmerend on 1971, August 27. He attended secondary school at the Niftarlake College in Maarssen, where he received the HAVO diploma in 1988 and the VWO Diploma in 1990. The same year, he started the study of Geophysics at the Utrecht University (UU). He specialized in Exploration Geophysics and Seismology and received his M.Sc. degree in 1996. His M.Sc. thesis in Seismology was on precursors to core phases from the D" layer extracted from seismic array data.

During his study, Läslo joint the Orfeus Data Centre (ODC) as student-assistant for the analysis and archival of earthquake data. The ODC moved from the UU to the Seismology Division of the Royal Netherlands Meteorological Institute (KNMI) in 1993. He continued working for the ODC also after his graduation. He also participated in paleoseismological studies in the framework of an international project funded by the European Commission.

In 1999, he became project leader of the project "Sonic Boom Detection Technique" funded by the Royal Netherlands Air Force. This project aimed at developing and demonstrating a technique for the detection of infrasound from sonic booms. A 16 element microbarometer array was constructed at an Air Force Base near the village of Deelen.

Läslo became part of the permanent staff of KNMI's Seismology Division in 2000 and continued studying infrasound. His work was presented at several international conferences and published as peer reviewed journal articles. This thesis was prepared in collaboration with the Faculty of Applied Sciences and Aerospace Engineering of the Delft University of Technology.

Acknowledgements

Adoring the study of atmospheric infrasound was not necessarily essential for writing this thesis but having a sparring partner sharing the same passion proved very inspirational both professionally and personally. Dr. H.W. Haak (KNMI) introduced me into the world of infrasound and guided me through much of my scientific maturation. Dear Hein, thanks a lot for the productive years we conducted research in infrasound together. I sincerely hope we will continue our fruitful collaboration in the future in the same joyful manner.

Prof. Dr. D.G. Simons (TU Delft) held his inaugural speech for the chair of Acoustic Remote Sensing in 2007. Soon afterward we started talking on infrasound and the large amount of scientific and societal benefits. All these unexplored areas in science. Dick, thanks for your interest and enthusiasm for the study of infrasound which has been very motivating for writing this thesis. May this thesis form the basis for our near future cooperation. I would like to thank all the people from the Acoustic Remote Sensing group for the warm welcome I received.

Prof. Dr. Ir. A. Gisolf (TU Delft) supported my work in infrasound in an early stage. Although, our initial cooperation did not start of as expected, I much appreciate your comments and thorough examination of my thesis. Dries, I learned from your remarks from a physical and textual point of view and appreciate your lasting interest in this work, for which I gratefully thank you.

Nicole has read every word of this thesis and corrected the text where necessary. We have also discussed about most of the research presented here. Thanks Nic, I much appreciate your critical view on my research. Big hug and kiss.

The KNMI has supported research in infrasound since 1985. The Seismology Division has gained a recognized (inter)national track record. Dr. B. Dost introduced me in 1993 to this group where we worked on several topics and allowed me to finalize this thesis which I much appreciate, thanks Bernard.